universität wien

DIPLOMARBEIT / DIPLOMA THESIS

Titel der Diplomarbeit / Title of the Diploma Thesis

Metal-organic framework-based materials for photoelectrochemical water-splitting

a study of the in-situ growth and effects of Cu-BDCNH$_2$ on cuprous oxide-based photo-cathodes

verfasst von / submitted by

Susanne Gross, BSc

angestrebter akademischer Grad / in partial fulfilment of the requirements for the degree of

Diplom-Ingenieurin (Dipl.-Ing.)

Wien, 2023 / Vienna 2023

Studienkennzahl lt. Studienblatt / degree programme code as it appears on the student record sheet:	UE 066 658
Studienrichtung lt. Studienblatt / degree programme as it appears on the student record sheet:	Masterstudium Chemie und Technologie der Materialien UG2002
Betreut von / Supervisor:	Assoz.Prof. Jia Min Chin, Ph.D.
Mitbetreut von / Co-Supervisor:	

Acknowledgements

In this part, I want to thank everyone that made this journey possible, that guided and accompanied me through my study, and who supported me as advisors, colleagues, and friends. I wholeheartedly want to thank my supervisors, Assoz.-Prof. Jia Min Chin, Ph.D., and Rachmat Adhi Wibowo, Ph.D., for providing me the opportunity to work and gain experience as a researcher in their respective groups at the University of Vienna and the Austrian Institute of Technology (AIT). Their advice and inputs were always valuable and guided me through the many months of my work – ultimately resulting in this thesis that I can proudly call my own. However, it was not only the productive working environment that they created that left an impression on me, but also they themselves – to Rachmat Adhi Wibowo, Ph.D., whose kind and cheerful ways always contributed to an enjoyable atmosphere, and also to Assoz.-Prof. Jia Min Chin, Ph.D., who always had an open ear when problems arose. Also, I want to express my gratitude to Theodoros Dimopoulos, Ph.D., and Domenico Grammatico, Ph.D, from AIT for their valuable advice, explanations, and help during my thesis work.

Furthermore, I want to thank the Österreichische Forschungsförderungsgesellschaft (FFG) for funding this project. Moreover, I would like to thank the Core Facility Interface Characterisation at the Institute of Materials Chemistry Research, with particular thanks to Dr.techn. Andreas Mautner and his contribution to this work by conducting the XPS experiments.

Next, I also want to thank all my working colleagues, not only for listening and helping me through my thesis work but also for their company – for the hiking trips and countless meals together that were always sparked with the most joyful conversations and silly banter. Of course, I also want to thank my friends that accompanied me through my studies, not only for studying and helping each other out in times of need but also for the diversion that is so very necessary at times to remain level-headed.

Last but not least, I want to thank my family for supporting me not only through my studies but through my whole life. Without you, I would not be where I am today, and for that, I truly thank you.

Abstract

The increasing demand for energy coupled with environmental issues, encourages researchers to look out for renewable and particularly green alternatives to traditional fossil fuels. Photo-electrochemical (PEC) water-splitting demonstrates a promising route to produce hydrogen as a zero-emission energy carrier in a green manner [1]. In this regard, the exploration of proper photo-active materials to construct PEC cells, as well as finding suitable co-catalysts, is of great interest. Among potential materials for PEC water-splitting applications, p-type cuprous oxide (Cu_2O) has been intensively studied due to its suitable band energy position, earth abundance, and low toxicity [2]. However, established techniques such as atomic layer deposition (ALD) to produce highly efficient Cu_2O-based PEC cells are costly and not commercially applicable [3]. Therefore, more commercially viable Cu_2O preparation methods need to be studied, for instance, the electrochemical deposition technique. Furthermore, metal-organic frameworks (MOFs) - a unique class of crystalline, porous materials recognized for their enhanced specific surface area and catalytic abilities - are investigated for their application in PEC water-splitting [2, 4].
The aim of this thesis is to explore the photo-cathodic behavior of cuprous oxide (Cu_2O), its enhancement in PEC performance using additional overlayers (metal oxides and polymer-based), and particularly to create a unique combination with a copper-based metal-organic framework, namely Cu-BDCNH$_2$. Cuprous oxide was deposited on glass/Au and ITO via ECD (electrochemical deposition) in a common three-electrode set-up to yield cuprous oxide-based photo-cathodes. As the synthesis of this MOF has not been implemented yet to the best of our knowledge, various settings and conditions have been tested to allow the growth of a continuous MOF layer onto the Cu_2O substrate film. To do so, other works of literature were used as starting points and adapted accordingly. Afterward, the obtained Cu_2O/MOF system was tested and analyzed through various methods (XRD, FTIR, XPS, SEM, EDS) and compared to existing literature. By combining MOF and Cu_2O, it was ultimately possible to achieve a photo-current density of 1.5 mA/cm^2 without the need for an additional co-catalyst.

Kurzfassung

Der steigende Energiebedarf gepaart mit Umweltproblemen ermutigt Forscher, nach erneuerbaren und besonders umweltfreundlichen Alternativen zu herkömmlichen fossilen Brennstoffen zu suchen. Die photoelektrochemische (PEC) Wasserspaltung stellt dabei einen vielversprechenden Weg zur umweltfreundlichen Herstellung von Wasserstoff als emissionsfreiem Energieträger dar [1]. In diesem Zusammenhang ist die Erforschung geeigneter photoaktiver Materialien für den Aufbau von PEC-Zellen sowie die Suche nach geeigneten Cokatalysatoren von großem Interesse. Unter den potenziellen Materialien für PEC-Wasserspaltungsanwendungen wurde p-Typ Kupferoxid (Cu_2O) aufgrund seiner günstigen Bandenergieposition, Erdhäufigkeit, und geringen Toxizität [2] intensiv untersucht. Allerdings sind etablierte Techniken wie Atomlagenabscheidung (ALD) zur Herstellung hocheffizienter Cu_2O-basierter PEC-Zellen kostspielig und nicht kommerziell anwendbar [3]. Daher müssen kommerziell einsetzbarere Cu_2O-Herstellungsmethoden untersucht werden, wie beispielsweise die elektrochemische Abscheidungstechnik. Darüber hinaus werden metallorganische Gerüste (MOFs) – eine einzigartige Klasse kristalliner, poröser Materialien, die für ihre erhöhte spezifische Oberfläche und katalytische Fähigkeit bekannt sind – auf ihre Anwendung bei der PEC-Wasserspaltung untersucht [2, 4].
Ziel dieser Arbeit ist es, das photokathodische Verhalten von Kupferoxid (Cu_2O) zu erforschen, seine Verbesserung der PEC-Leistung durch zusätzliche Überschichten (Metalloxide und Polymerbasis) zu untersuchen und insbesondere eine einzigartige Kombination mit einem kupferbasierten metallorganischen Gerüst, nämlich Cu-$BDCNH_2$, herzustellen. Kupferoxid wurde mittels ECD (elektrochemische Abscheidung) in einem üblichen Drei-Elektroden-Aufbau auf Glas/Au und ITO abgeschieden, um Photokathoden auf Kupferoxidbasis zu erhalten. Da die Synthese dieses MOF auf Kuperoxid auf diese Weise nach unserem Wissens noch nicht umgesetzt wurde, wurden verschiedene Einstellungen und Bedingungen getestet, um das Wachstum einer kontinuierlichen MOF-Schicht auf dem Cu_2O-Substratfilm zu ermöglichen. Dabei wurden andere Literaturen als Ausgangspunkt genutzt und entsprechend angepasst. Anschließend wurde das erhaltene Cu_2O/MOF-System mit verschiedenen Methoden (XRD, FTIR, XPS, SEM, EDS) getestet und analysiert und mit vorhandener Literatur verglichen. Durch die Kombination von MOF und Cu_2O war es letztendlich möglich, eine Photostromdichte von $1.5\,mA/cm^2$ zu erreichen, ohne dass ein zusätzlicher Cokatalysator erforderlich war.

Contents

1 | Introduction

1.1 Motivation

The ever-increasing demand for energy linked to the swift population growth as well as related environmental issues are amongst the greatest challenges confronting scientists of the 21st century. Even though fossil fuels are widely regarded as problematic due to being non-sustainable and being the cause of severe environmental and health-related problems [5, 6], the world's energy demand is still mainly covered by fossil fuels, including coal, natural gas, and related products [7, 8]. As a result, large quantities of greenhouse gases (GHG), among them, carbon dioxide (CO_2), methane (CH_4), and nitrous oxides (N_2O), are released through fossil fuel combustion into the atmosphere, leading to multiple issues related to the topic such as weather changes, health problems, changes in the ecosystem, sea-level rise, etc. [7, 9]. Figure 1.1 illustrates the global direct primary energy consumption beginning from 1800 till 2021. While roughly 80% of the world's primary energy consumption stems from fossil fuels, around 14% is covered by renewable resources, although the trend towards renewable energy sources is steadily increasing. While the primary energy consumption doubled from 1800 to 1900, a nine-fold rise in the energy consumption was measured from 1900 to 2000. The already high consumption of 112 TWh has been increased 1.5 times until 2021 to around 159 TWh, the main contributors remaining coal, oil, and gas.

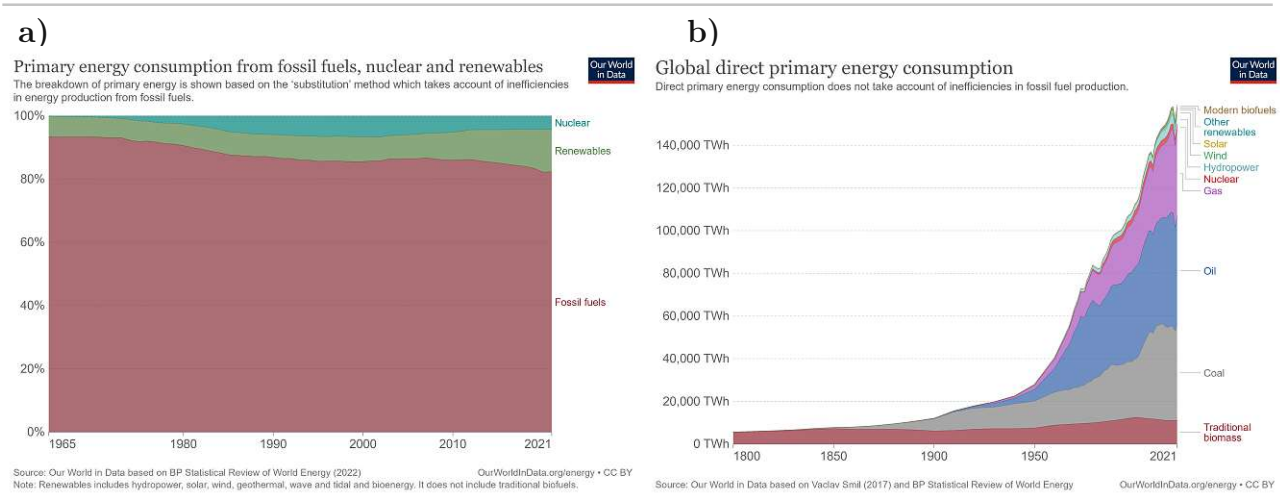

Figure 1.1: Development of global direct primary energy consumption through the years. a) displays the relative development of the global direct primary energy consumption from 1965 till 2021, whereas b) shows the development of the primary energy consumption from 1800 till 2021 measured in terawatt-hours (TWh) divided among the resources [10, 11].

Because of the fast growth in the civil and industrial sectors as well as recent political tensions throughout the world, governments started to adjust their strategies concerning the minimization of GHG emissions as well as to ensure a certain level of energy-related autarky [7].

Thus, improving the efficiency of current technologies as well as developing new devices to act as renewable alternatives to fossil fuels while simultaneously addressing the topics such as global warming and climate change is of utmost importance. Hence, seeking renewable, carbon-neutral energy sources is urgently needed, ultimately shaping the field of future energy production[12] due to the following challenges [13]:

- human-induced/accelerated climate changes due to GHG emissions via the combustion of fossil fuels
- limited reserves of fossil fuels
- increasing price of fossil fuels
- need for fuel that can be obtained from raw materials that are abundantly available
- need for environmentally benign fuel

In this regard, hydrogen (H_2) is a potential solution to the abovementioned challenges. Driven by these circumstances, scientists have been working vigorously to discover and fabricate catalyst materials that are efficient, earth-abundant, and ideally low-cost to generate green hydrogen through clean and sustainable processes from water as its feedstock by photoelectrochemical water-splitting [14].

1.2 Hydrogen as a renewable energy source

For long, hydrogen as an alternative energy source has gained tremendous attention in the pursuit of opening the path for a low-carbon future. Alone 2019, 33.3 metric gigatons of CO_2, related to energy production processes were recorded around the globe, a number that is still growing at a considerable rate. The consequence of the release of GHG such as CO_2 is a rise in the earth's temperature by several degrees, causing severe environmental problems. However, as the energy-related sectors are widely dependent on fossil fuels (schematically displayed in Figure 1.2 a), the decarbonization of these sectors, and therefore, the reduction of emissions faces various difficulties [15]. In the face of these difficulties, many countries pushed towards renewable energy technologies [15]. One of these technologies is the production of 'green hydrogen', which is the production of hydrogen via water electrolysis by making use of electric current to break down H_2O into hydrogen (H_2) and oxygen (O_2). This route is generally regarded as an interesting approach to decreasing the dependency on fossil fuels while not producing any GHG emissions - of course, under the assumption that hydrogen was generated employing only sustainable energy sources as well (e.g., solar or wind) [13]. Hydrogen in itself shows favorable properties such as high mass-energy density, facile electrochemical conversion, and lightweight. In addition, it can be carried across geographical regions utilizing pipelines or by converting it to its liquid form [16]. Furthermore, hydrogen can be stored across seasons in tanks or in caverns underground [15]. Also, hydrogen serves multiple purposes as it can be utilized as a reagent for the synthetic production of fuels, make use of it as a chemical feedstock, or burn it for heating[15]. This inherent flexibility of hydrogen renders it a promising candidate in the crusade for a renewable future [16]. As can be seen in Figure 1.2 b) hydrogen and electricity could be implemented in tandem to cater to all energy-related sectors.
However, in a study by Oliveria et al. [15], it is stated that hydrogen may not end up being the most important energy economy due to unavoidable energy losses that occur at the conversion of electricity to hydrogen, but it will still play a vital role when it comes to establishing a sustainable energy society.

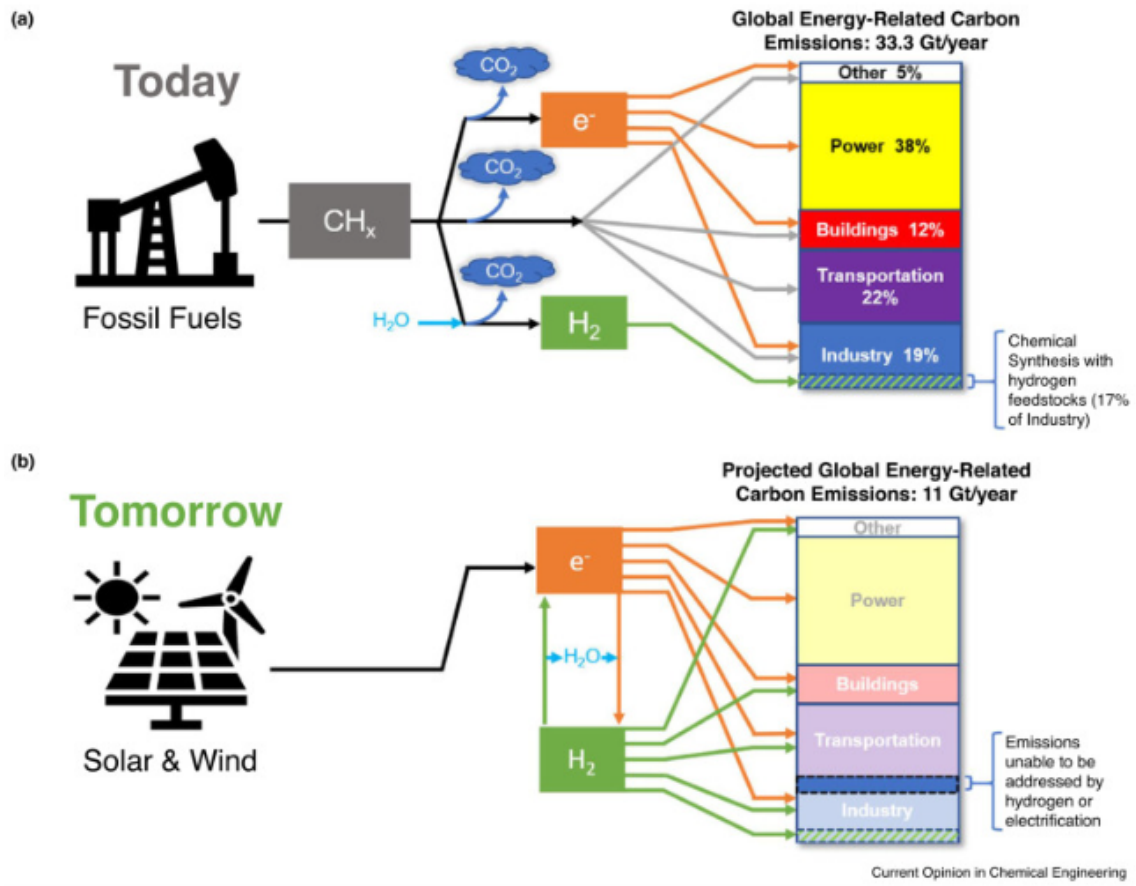

Figure 1.2: Schematic illustration of the energy sectors of today and tomorrow [14].

As aforementioned, the ongoing research to find a way to obtain hydrogen from water is mainly driven by the desire to seek out valid alternatives for a low-carbon future that are both sustainable and environmentally friendly in its usage. As the electrolysis of water results in oxygen as the only by-product[13], provided that the electricity used in the process stems from renewables as a whole, photo-electrochemical (PEC) reactors coupled with a fuel cells present the ideal case, as hydrogen is again combined with oxygen to produce water [17] without air pollution nor the emission of GHG.

$$\text{Generation:} \qquad H_20 + energy(\text{solar}) \rightarrow H_2 + \frac{1}{2}O_2 \qquad \text{(PEC reactor)}$$

$$\text{Consumption:} \qquad H_2 + \frac{1}{2}O_2 \rightarrow H_2O + energy \qquad \text{(Fuel cell)}$$

In general, PEC water-splitting is viewed as a promising route to produce hydrogen. Since the introduction of the method by Honda et al. [18] almost 50 years ago, countless papers have been published exploring different materials and composites and their performance as PEC cells [13]. Currently, it is stated in the literature that the main work lies in enhancing the efficiency as well as the stability of the photo-active materials, mostly metal oxides, with a target efficiency of 10% in order to create a system ready for commercialization [17]. Although there are already systems that achieve an efficiency of 10% they are mostly based on multi-junction conventional semiconductors, which degrade within a short time [17, 19].
Thus, the ideal photo-electrode should satisfy the following requirements in order to be commercially attractive [2, 13]:

- high activity for water-splitting
- long-term stability
- good light absorption and charge transfer
- low cost of manufacturing and maintenance
- environmentally friendly

In this regard, p-type cuprous oxide (Cu_2O) has been intensively studied because of its various advantages, such as favorable positions of the valance and conduction band featuring a direct bandgap of ∼2 eV appropriate for visible light absorption, earth abundance, and low toxicity. Furthermore, a high theoretical photo-current density up to 14.7 mA/cm^2 was calculated for Cu_2O based on the AM 1.5 spectrum [2]. This renders p-type cuprous oxide an interesting material for PEC water-splitting applications. The highest yet achieved photo-current density for a Cu_2O-based system of 10 mA/cm^2 was reported by the Grätzel group, which employed atomic layer deposition (ALD) to craft Al-doped ZnO/TiO_2 protective overlayers onto Cu_2O[19]. However, the ALD technique is generally regarded as too complicated and expensive for large-scale usage [3]. Thus, alternatives are being investigated.
Particularly, metal-organic frameworks (MOFs) mark an interesting class of materials already implemented in various technologies such as catalysis [20], sensing [21], CO_2 reduction [22], hydrogenation [23], organic transformations[24], as well as PEC water-splitting [2]. MOFs are made out of metal ions connected via organic ligand units, and due to the wide range of ligand and metal ions available for the MOF construction, they show great flexibility when it comes to the design of a suitable catalytic material [2]. Furthermore, they are recognized for their structure displaying high porosity and large specific surface area [4] as well as other advantages, which will be further discussed in the following section.

1.3 Aim and Methodology of the thesis

As PEC water-splitting route is an interesting procedure to obtain hydrogen as a zero-emission energy carrier alternative to polluting fossil fuels in a green and environmentally friendly manner [1], the investigation of proper photo-active materials as well as suitable co-catalysts is of great importance. Especially, Cu_2O has been regarded as an interesting candidate for this matter, however, established techniques to produce highly efficient PEC cells are costly and thus not commercially applicable. Thus, the aim of this thesis is to study the photo-cathodic behavior of cuprous oxide (Cu_2O), prepared by electrochemical deposition, its enhancement in PEC performance using overlayers of different nature (metal oxides and polymer-based), and particularly creating a unique combination with copper-based MOF, namely Cu-$BDCNH_2$. As the synthesis of this MOF in this matter has not been implemented yet to the best of our knowledge, various settings and conditions have been tested in order to allow the growth of a continuous MOF layer onto the Cu_2O substrate film. In order to do so, other literatures were used as starting points and adapted accordingly. Afterward, the obtained Cu_2O/MOF system was tested and analyzed through various methods and compared to existing literature.

2 | Theoretical background and state-of-the-art

2.1 Fundamental principles of PEC water-splitting

The principle of PEC water-splitting relies on the direct conversion of light into electricity. For this to occur, two electrodes, which are immersed in an electrolyte containing water, are connected by an external circuit to decompose water into its basic components - hydrogen and oxygen. At least one electrode has to be made of a semiconducting material that will absorb light upon exposure and the generated electricity that will be used for water electrolysis. Hence, the PEC apparatus should allow for good light exposure so that a maximum amount of photons can reach the semiconducting material [17]. In theory, there are three common options for assembling photo-electrodes in the PEC system [13]:

- a photo-anode consisting of n-type semiconducting material together with a metallic cathode
- a photo-cathode consisting of p-type semiconducting material together with a metallic anode
- a photo-anode consisting of n-type semiconducting material together with a photo-cathode consisting of p-type semiconducting material

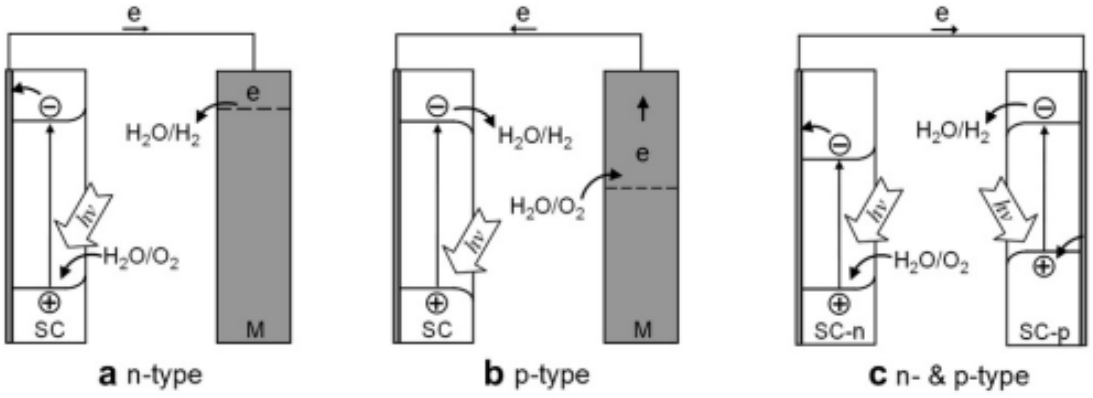

Figure 2.1: Schematic illustration of common photo-electrode arrangements for PEC water-splitting applications (SC stands for semiconductor; M stands for metal) [17].

Charge separation and transfer occur due to band banding at the interface of the light-absorbing material and the aqueous electrolyte, which is seen as the general driving force. Here, a built-in electric field can be introduced to adjust the degree of band bending by an applied bias. As can be seen in Figure 2.1 c), the upward band bending on the photo-anode drives the photo-generated holes (h^+) towards photo-electrode/electrolyte interface, whereas

the photo-generated electrons (e^-) at the photo-cathode are pushed to the active sites by downward band bending. When a good combination of these photo-electrodes with proper band alignment is secured, efficient charge separation and transport will take place, leading to a good PEC water-splitting performance [25].

As the focus of this thesis lies on p-Cu_2O and its performance as a photo-cathode, the following sections will be limited to the second photo-cell arrangement as visualized in Figure 2.1 b). Table 2.1 provides an overview of the main requirements necessary for PEC water-splitting.

Table 2.1: Required conditions for PEC water-splitting. Table adapted from ref. [17].

Conditions	**Main requirements**
PEC water-splitting	$H_2O(l) + 2h\nu \rightarrow \frac{1}{2}\ O_2(g) + H_2(g)$
Minimum potential requried	$E^{\circ}_{H_2O}(25°C) = 1.23$ eV
Practical overpotential (+ overpotential & losses)	$E^{\circ}_{H_2O}(25°C) = 1.6$ - 2.0 eV $E_{BG} > E^{\circ}_{H_2O}$
for efficient utilization of sunlight	$UV > h\nu(Vis) > IR$ $h\nu \geq E_{BG}$
Band edges requirements	$CB_{bandedge} < E^{\circ}{}_{H_2/H^+}$ $VB_{bandedge} > E^{\circ}{}_{O_2/H_2O}$

2.1.1 Thermodynamic aspects of PEC water-splitting

During PEC water-splitting, water gets broken down into its basic components using a semiconducting material that produces electron-hole pairs when it is exposed to a light source of sufficient energy. They then travel to the surface of the light-absorbing material and drive the reaction at the interface between the semiconducting material and the electrolyte [26]. According to thermodynamics, this process involves energy of around 285.8 kJmol^{-1}. This is equal to the energy released when hydrogen is combusted into water [26]. Because of the positive value of Gibb's free energy, the water-splitting reaction is considered an uphill reaction and corresponds to the maximum energy achievable and the released heat (48.6 kJmol^{-1}) [27]. Considering the nature of the redox reaction, if energy equal to Gibb's free energy (237.2 kJmol^{-1}) is put into the system, water can be thermodynamically converted into its compounds Eq.2.1) [26, 27].

$$H_2(g) + \frac{1}{2}O_2(g) \rightleftharpoons H_2O(l) + 237.2\ kJ/mol + 48.6\ kJ/mol\ (heat) \tag{2.1}$$

Under normal conditions, the change in Gibb's free energy ($\Delta G = 237.2$ kJmol^{-1}) necessary to convert one molecule H_2O into its components corresponds to 1.23 eV per electron in the transfer process [28]. Thus, for the water-splitting reaction to happen, a potential barrier of 1.23 V needs to be overcome [28]. However, to further push the reaction, the excess heat and losses in the system need the be considered as well, further pushing the minimum potential barrier to higher values (285.8 kJmol^{-1}). When the total energy of 285.8 kJmol^{-1} is converted, this value ends up being 1.48 V [26]. The excess potential required to drive the reaction is called the overpotential. Hence, the photo-voltage produced by the photo-electrode must be greater than 1.23 V for the water electrolysis to occur [28].

2.1.2 Working principle of PEC cells

The PEC setup consists of two electrodes, where at least one is photo-active, that are placed in a suitable electrolyte within a container as illustrated in Figure 2.1. The container can be either transparent so that the light can reach the PEC cell or fitted with an optical window. If the energetic requirements (summarized in Table 2.1) are fulfilled, the water-splitting reaction will happen on the surface of the photo-active material[17].
In general, PEC water-splitting involves the following four steps [26]:

(i) absorption of light by the semiconducting material,
(ii) creation of charge carriers (photo-electrons and holes),
(iii) separation of photo-electrons and holes, and
(iv) transportation of charge carriers to the surface of the semiconducting material [26].

First, light with energy greater or equal to the BG of an appropriate semiconducting material is absorbed. The light absorption excites the electron-hole pairs, followed by their separation. The electrons migrate towards the photo-cathode, and positively charged holes are left behind. It is of great importance that the valence band (VB) and conduction band (CB) in the semiconducting material are suitably positioned: For hydrogen evolution reaction (HER) to occur, the CB edge needs to be more negative than the reduction potential of the proton ($E_{CB} < E^0_{red}$), whereas for the oxygen evolution reaction (OER) the VB edge is required to be more positive than the water oxidation potential ($E_{VB} > E^0_{ox}$) [26].

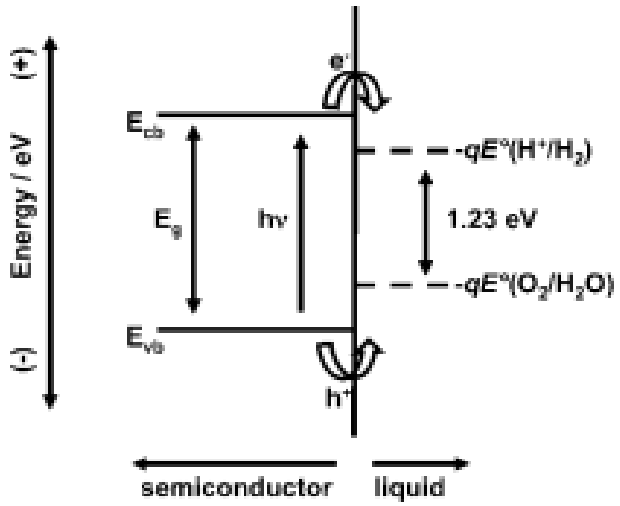

Figure 2.2: Schematic illustration of the HER and the OER occurring for an ideal semiconducting material on an absolute energy scale [28].

In general, the water-splitting reaction is composed of two half-reactions: the HER that happens at the cathode and OER that happens at the anode. While the reduction of protons during the HER is a two-electron process, the oxidation of water requires four electrons. Hence, the OER is kinetically more sluggish compared to the HER and is considered the bottleneck reaction[29]. Table 2.2 displays the reactions occurring in the half-cell [26].

Table 2.2: PEC Half-reactions as reported in [26].

Anode:	$2H_2O(l)$	$\rightarrow$	$O_2(g) + 4H^+ + 4e^-$	(OER)
Cathode:	$4H^+ + 4e^-$	$\rightarrow$	$2H_2(g)$	(HER)
Overall:	$2H_2O(l)$	$\rightarrow$	$O_2(g) + 2H_2(g)$	

Furthermore, the redox potentials for the water-splitting reactions are pH dependent [28]. Thus, the water-splitting reactions at low pH conditions [26] are displayed in Eq. (2.2) and (2.3),

$$\text{Anode:} \quad H_2O + 4h^+ \rightleftharpoons O_2 + 4H^+ \qquad \Delta E^0_{ox} = 1.23\ V_{RHE} \tag{2.2}$$

$$\text{Cathode:} \quad 4H^+ + 4e^- \rightleftharpoons 2H_2 \qquad \Delta E^0_{red} = 0\ V_{RHE} \tag{2.3}$$

while the reactions under high pH conditions [26] are shown in Eq. (2.4) and (2.5):

$$\text{Anode:} \quad 2OH^- + 4h^+ \rightleftharpoons O_2 + 2H_20 \qquad \Delta E^0_{ox} = -0.404\ V_{RHE} \tag{2.4}$$

$$\text{Cathode:} \quad 4H^+ + 4e^- \rightleftharpoons 2H_2 \qquad \Delta E^0_{red} = -0.826\ V_{RHE} \tag{2.5}$$

2.2 Material aspects of photo-electrodes

According to molecular bonding theory, when atoms get together to form a molecule, their energy levels split accordingly, and bonding and anti-bonding levels are formed. The energy difference between these two levels decreases rapidly with the increasing number of participating atoms, forming closed sets of energy levels (energy bands). This phenomenon creates two energy bands: the valance band (VB) and the conduction band (CB). While the former contains the highest occupied molecular orbital (HOMO), the latter encloses the lowest unoccupied molecular orbital (LUMO). These two bands (VB and CB) can be attributed to the bonding and anti-bonding energy levels, respectively, and the gap in-between is called the band-gap (BG). For semiconducting materials, this BG is commonly positioned in the range of 0.5–2.5 eV. Upon excitation, e.g., via light, it is possible to excite the negatively charged electron in the VB to the CB, and a positively charged hole is left behind. These photo-generated charge carriers play a key role in this process[26, 30]. As pure semiconducting materials usually display poor electron conductivity, they get contaminated (doped) with other atoms, which serve as donors or acceptors for electrons. A common example is silicon that is either doped with phosphorus, which contributes electrons to the system (n-type Si), or boron with fewer valence electrons compared to Si, generating a hole-rich semiconductor (p-type Si) (see Figure 2.3). Hence, for n-type semiconducting materials, electrons are the main charge carriers, while p-type semiconductors have holes as the main charge carriers [30].

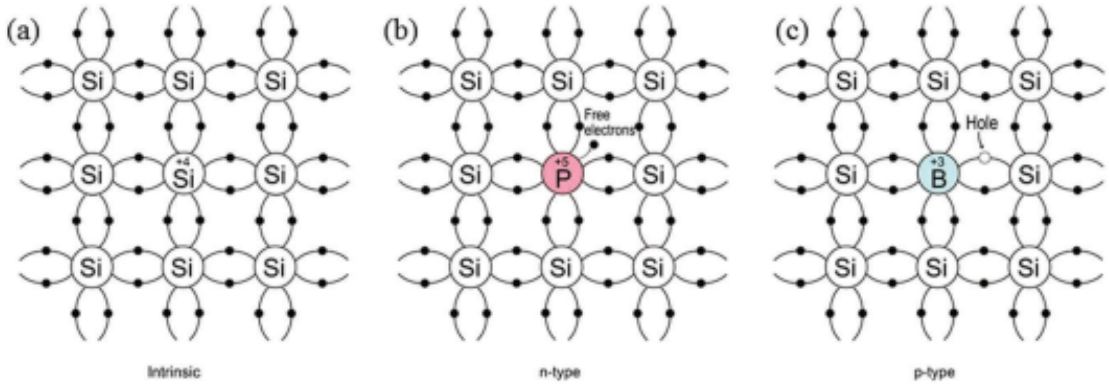

Figure 2.3: Schematic bond representation silicon with (a) nothing; (b) with phosphorus leading to the n-type doping of silicon (c) with boron leading to the p-type doping of silicon [30].

The choice of an appropriate photo-electrode material is of utmost importance when designing a cell for PEC water-splitting. Independently of the purpose (photo-cathode or photo-anode) the optimal semiconductor material displays the following characteristics:

(i) *Appropriate band alignment and band-gap.* Light, as it occurs in nature, is made of 5% ultraviolet (300–400 nm), 43% visible (400–700 nm), and 52% infrared radiation (700–2500 nm) [30]. Thus, in order to generate sufficient photo-voltage, the semiconducting material needs to be capable of absorbing light in the visible range of the solar spectrum [30]. Furthermore, in addition to the minimum energy (1.23 V) required for light photons to overcome the minimum barrier of the HER, additional losses in energy need to be considered. These losses occur due to charge carrier transportation processes as well as the application of an additional overpotential to ensure fast-enough surface reaction kinetics. Everything considered, the minimum BG increases to around 1.8 eV, which corresponds to a wavelength of light of around 700 nm. Generally, the upper limit of the BG range is 3.2 eV as the light intensity decreases swiftly once it is below 390 nm [30].
Thus, the ideal semiconductor for PEC water-splitting possesses a BG between 1.6–2.6 eV[26]. Figure 2.4 shows the band alignment of various semiconductor materials.

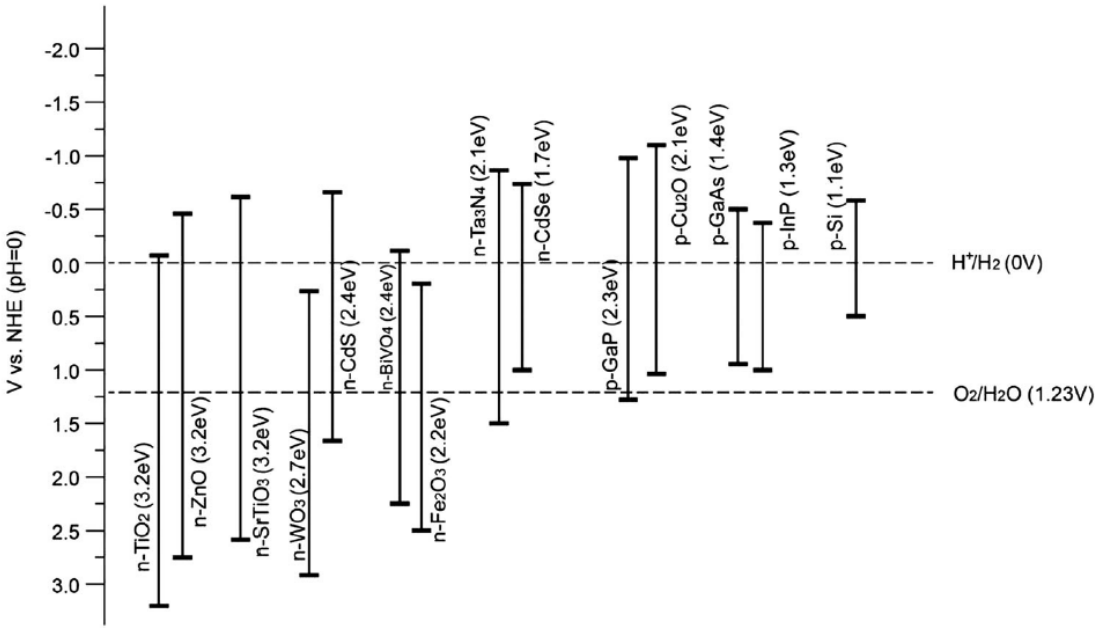

Figure 2.4: BGs and band alignments of common semiconducting materials studied for of water-splitting at pH = 0 [30].

In theory, a BG of around 2.0 eV is preferred for ideal sunlight absorption under the prerequisite of suitable band positions [30]. Narrow bandgap p-type semiconducting materials such as Cu_2O, Cu_2S, and p-Si possess favorable positioned CB edges for photo-cathodes, with optimal BGs for light absorption. N-type semiconductors such as $BiVO_4$, and Fe_2O_3 are suitable for OER with their appropriate absorption of visible light and viable VB edges. Compared to that, n-type semiconductors, e.g., TiO_2 and CdS may have favorable band-edge positions for OER, but due to the wide BG, the PEC efficiency is low in contrast to narrow BG semiconductors [26].

(ii) *Efficient electron-hole separation and transportation within the light absorbing material.* The recombination of charge carriers is a significant problem in PEC water-splitting. To promote swift charge separation and transfer of electron-hole pairs, both intrinsic properties (charge carrier mobility) and the extrinsic properties (structure, crystallinity) of the semiconducting material need to be addressed [30].

(iii) *Stability and high catalytic performance.* Fast reaction kinetics are capable of averting the accumulation of charges on the surface, suppressing recombination events. Furthermore, photo-corrosion, a process where holes or electrons generated via light absorption are not used for the oxidation or reduction of water but for the decomposition of the catalyst itself, is a major issue for many potentially suitable semiconductors and depends on the relative positions of the band edges as well as the respective potentials of the decomposition of the material. For anodic photo-corrosion to take place, the decomposition potential is positioned above the VB potential, whereas cathodic photo-corrosion occurs when the decomposition potential is positioned below the CB of the light-absorbing material [30].

2.2.1 Cuprous-oxide based photo-cathodes

Among possible p-type semiconducting materials employed as photo-cathodes for PEC water-splitting reaction, cuprous oxide (Cu_2O) can be a good candidate that shines with several advantages such as abundance, low toxicity, as well as a high theoretical photo-current of -14.7 mA/cm^2 [31]. Furthermore, Cu_2O is considered a natural p-type semiconductor due to vacant copper ion lattice sites, which act as electron acceptors [32]. This hypothesis regarding the origin of the p-type nature of Cu_2O is generally accepted and supported by theoretical [33, 34] and experimental [35, 36] studies. Concerning its structural properties, Cu_2O displays a simple cubic crystal structure, belongs to the space group $Pn\bar{3}m(224)$ and a lattice constant of 4.2696 ± 0.0010 [37]. Its unit cell is visualized in Figure 2.5.

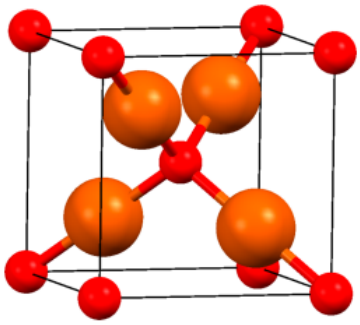

Figure 2.5: Crystal structure of Cu_2O: oxygen (red), copper atoms (orange)[37].

As discussed earlier, Cu_2O can be utilized for PEC HER as it features a small direct BG of approximately 2 eV, allowing for the absorption of light in the range of 300 to 620 nm. This enables the absorption of around half of the light photons the visible solar spectrum has to offer [38]. Moreover, Cu_2O displays good alignment of the energy band edges, where the CB is positioned at 0.7,negative to the HER, whereas the VB is slightly more positive than the OER potential. Thus, there is no overpotential available for the OER. This means that HER can be conducted by the photo-cathode, while the OER needs an external bias [31]. Moreover, the Fermi level positioning of Cu_2O also allows the possibility of combining it with an n-type semiconducting material to fabricate efficient devices for water-splitting by creating a p-n junction [38].

Limitations and Strategies

Despite its promising nature, Cu_2O faces several disadvantages, such as poor stability in aqueous solutions and low mobility of the majority charge carriers, which causes recombination events and lowers the efficiency [38].
Since the redox potentials for Cu_2O fall in-between its BG (see Figure 2.6), it is prone to photo-corrosion, which is considered a major drawback of Cu_2O [30]. Furthermore, the Cu_2O film needs to be at least 1 μm thick to ensure sufficient absorption of the light. Also, the right orientation of the Cu_2O crystals obtained via electrodeposition is an important factor for the stability as Cu^+ (111) terminated surfaces in polycrystalline Cu_2O are reported to be more stable compared to other orientations such as O^{2-} terminated (211) and (311) surfaces [37, 38]. Thus, the deposition process needs to be optimized to ensure a high degree of Cu^+ (111) terminated surfaces. In addition, the relatively small BG limits the light-absorbing ability to 600 nm, rendering Cu_2O incapable of harvesting the entire light from the visible spectrum [38].

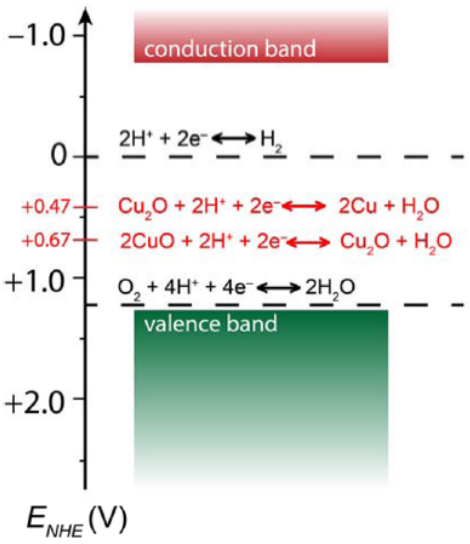

Figure 2.6: Illustration of the band alignment of Cu_2O. The potentials at which the photo-corrosion reactions occur are highlighted in red [37].

Various strategies have been tested to solve the limitations of Cu_2O, e.g.: (1) combining Cu_2O with an n-type semiconducting material. By combing Cu_2O with a suitable n-type material (e.g., TiO_2), it is possible to create a p-n junction that enhances the charge transport of photo-generated electrons to travel from Cu_2O to the n-type semiconducting material, which in turn increases the efficiency and the stability of Cu_2O [38]. (2) The addition of a thin-film protection layer on top of Cu_2O. This protection layer could be composed of different materials e.g., metal oxide or carbon. It is to note that, the protection layer needs to be pin-hole-free and form a proper p–n junction that is both contiguous and uniform to obtain a stable Cu_2O-based PEC electrode [30, 38]. The additional use of a (3) co-catalyst can also greatly accelerate reaction kinetics by facilitating the electron-hole separation and preventing recombination events. Moreover, the active surface sites of MOFs allow for the adsorption of ions [26]. Figure 2.7 schematically illustrates a typical photo-cathode architecture.

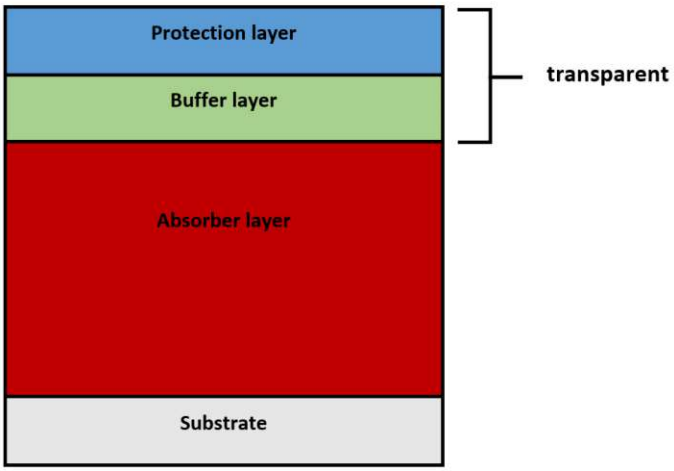

Figure 2.7: General architecture for photo-cathode displaying a buffer layer to form a p-n junction as well as a window layer for protection purposes.

2.3 Structures and Properties of MOF materials for PEC water-splitting

Metal-organic framework (MOF) materials have gained increasing attention due to properties such as controllable porous size, tunable framework structure, and compositions [39]. They present a class of porous materials that are synthesized by joining metal ions with organic linking units to form porous, crystalline frameworks featuring multiple coordination sites [40] (see Figure 2.8).

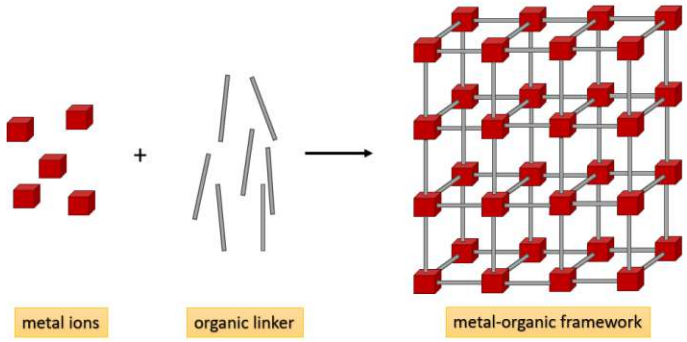

Figure 2.8: Schematic illustration of the construction of the crystalline MOF structure.

Because of their diverse structures and exceptional tunability of nearly every aspect, including particle and pore size, surface area, as well as post-synthetic modifications to name a few, these hybrid inorganic–organic crystalline materials possess a broad potential for a wide range of applications [41], e.g., sensing [21], hydrogenation [23], CO_2 reduction [5], N_2 reduction [42], and PEC water-splitting [2]. By selecting a suitable metal ion, it is possible to design photo-responsive MOF materials that, in combination with an appropriate semiconductor, could lead to a promising approach to develop devices for effective solar-conversion processes [25].

The first reported MOF recognized for its intrinsic semiconducting properties to participate in photo-catalysis had been reported by Alvaro et al. [43] in 2007. Here, the charge transfer from ligand to metal was explored upon light irradiation in MOF-5. Further studies in the field soon highlighted the advantages of MOFs for efficient photo-catalysis, including [4]:

(i) *Highly porous structure*, allowing MOFs to separate charge carriers as well as allowing the option to introduce co-catalysts and photo-sensitizers.
(ii) *Offering more active sites*, for enhanced HER.
(iii) *Integration of functional groups in MOFs*, for the improved adsorption of reactions and the diffusion of products.
(iv) *Efficient use of light*, by adjusting the MOF structure accordingly.
(v) *Tunablity of the MOF structure*, enabling structure studies on the activity of MOFs as well as flexibility regarding the chemical properties.

Despite the promising nature of MOFs in the field of water-splitting applications, they still need further development as most MOFs suffer under a narrow light absorption region. Furthermore, the BG of many MOFs is not suitable to promote the HER. Moreover, it has been stated in the literature that electron–hole pair separation ability is still in need of further development. Additional stability problems regarding exposure to moisture also hamper its

usage [39, 40]. However, it is possible to address these issues in multiple ways:

A wide range of techniques exists to enhance the performance of MOF materials in the field of photo-catalytic HER. For example, the structure can be specifically tailored via ligand functionalization, defect engineering, metal doping, and morphology regulation. Additionally, it is possible to load guest molecules like co-catalysts (metal, non-metal) and photo-sensitizers onto the MOF surface to construct heterostructures [39]. Furthermore, hydrophobic coatings can be employed to increase the stability of MOFs [40]. Figure 2.9 summarizes different strategies to produce stable MOFs for PEC water-splitting.

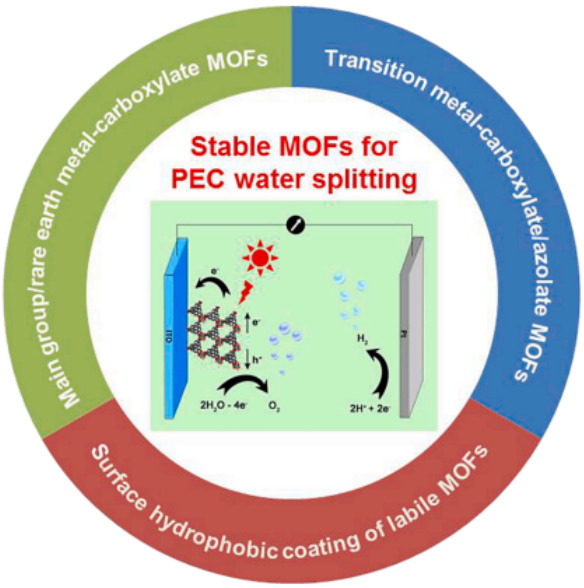

Figure 2.9: Schematic illustration of different strategies to obtain stable MOFs [40].

The semiconducting properties for photo-catalysis and photo-electronics of certain types of MOFs have already been demonstrated [44]. MOFs that have been employed for photo-catalytic and PEC hydrogen production include NH_2-MIL-101 (Cr) [45], NH_2-UiO-66 [46], and NH_2-MIL(Ti) [47]. A typical laboratory test setting for photo-catalytic hydrogen production usually includes MOFs in powdered form that get dispersed to yield a suspension of MOFs in water. However, this procedure harbors extra costs, as powdered MOFs normally cannot be recycled. Hence, depositing MOFs on a substrate of choice to give MOF films that are catalytically active, is typically highly desired [48].

2.3.1 Copper-based MOFs

Among the earliest metals used in history, copper (cu) represents a relatively earth-abundant metal with low mining costs [39]. In addition, it has the same electronic structure as the noble metals Au and Ag, as it is in the periodic table group. Its various oxidation states ranging from Cu(0) to Cu(III), lead to a wide variety of redox reactions, and up until today, various complexes utilizing Cu have been tested for HER [4]. The central divalent copper ion of Cu-based MOFs is four- or six-coordinated and displays unsaturated coordination sites, which can act as reactive sites to drive the photo-catalytic reaction [39]. For example, Dong et al. [49] produced a Cu-based MOF called Cu-RSH, which presented a combination of rhodamine-derived organic ligands that displayed photo-activity, with copper ions as the central ions, which was capable of remaining stable in solutions ranging from pH 2 to 14. Furthermore, this MOF was capable of efficiently catalyzing co-catalyst free H_2 generation under visible

light irradiation. Herein, it was stated that the results were due to open coordination sites, effective light absorption, as well as because of the enhanced redox ability of the cooper central ions.
Another study presented the semiconductive MOF $\{[Cu^{I}Cu^{II}_{2}(DCTP)_{2}]NO_{3}\cdot 1.5DMF\}_{n}$ that displayed a narrow BG of 2.1 eV and two different photo-catalytic activities attributed to the photo-generated charge carriers (electrons and holes). Due to this, the photo-catalytic hydrogen production and the degradation of methyl blue, an organic dye, were observed without the aid of a photo-sensitizer [50]. Furthermore, a Cu(II)-based MOF, namely MOF-199, was electrodeposited on nickel foam and exhibited exceptionally high photo-catalytic activity for HER with good recyclability and reusability using Pt as the co-catalyst and with the aid of Eosin as a photo-sensitizer [48].

The present work studies the formation of Cu-BDCNH$_2$ MOF (see Figure 2.10) on the Cu_2O-based photo-cathode. The use of CuBDC with 1, 4-benzenedicarboxylate (BDC) as an organic linker to form a two-dimensional network has already been implemented for PEC CO_2 reduction [51]. Here, CuBDC was obtained in-situ via solvothermal synthesis on copper foam, which acted as the source for the metal ions. Furthermore, by properly changing the volume ratio of the solvent mixture for the synthesis, the group of Xue et al. [51] was able to obtain well-regulated MOF crystals of controllable thickness.
Cu-BDCNH$_2$, similar to Cu-BDC, has paddlewheel secondary building units (SBUs) [51]. In this case, the 1,4-BDC-NH$_2$ (2-amine-1,4-benzenedicarboxylic acid) was employed as an organic linking unit, which yields a three-dimensional structure[52].

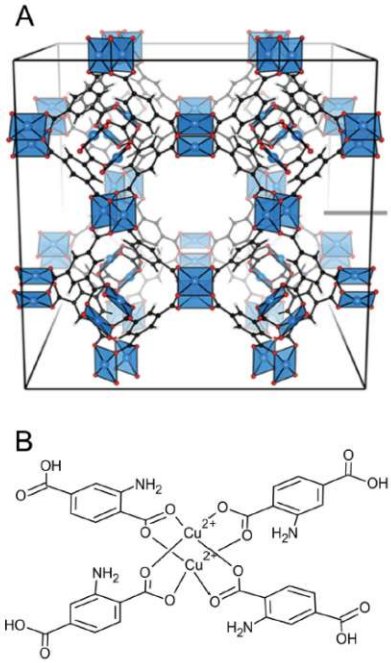

Figure 2.10: A) Cu-BDCNH$_2$ MOF cubic structure, and B) Cu_2Iw paddle-weel secondary building unit [52].

2.4 State-of-the-art PEC Architectures

A collection of different PEC architectures with their corresponding performances is shown in Table 2.3. The cells vary deposition techniques, testing environments, as well as additional protection layers and co-catalysts to provide a broad overview covering the most known strategies for Cu_2O-based photo-cathodes. Their sole common ground is the usage of Cu_2O as absorber material as a solid film substrate. As can be seen from Table 2.3 generated current is rather broad and can vary from <1 to >10 mA/cm^2. Further, while comparing the different studies, it is noticeable electrochemical bath deposition (ECD) is a common fabrication method for Cu_2O. While ALD techniques dominate the field by generating the highest photo-current, carbon-based protection layers also produce good results.
Since the first introduction in 1972 of TiO_2 as a photo-electrocatalyst for PEC water-splitting by Fujishima and Honda [18], many research groups have attempted to develop other semiconductor materials as photo-electrocatalysts to facilitate this reaction. Among those, MOFs appear as potential candidates due to their versatile nature. Even though the implementation of MOFs in PEC water-splitting devices is still at the beginning, a few pure MOFs, as well as MOF-based composites, have shown promising results [40]. It is to note that while other reports on MOFs for PEC water-splitting exist, only one source [2] reports their use as photo-cathode in a similar setting as in this thesis and is therefore listed in Table 2.3.

Table 2.3: Selected reports of the performance Cu_2O photo-cathodes for PEC water-splitting, highlighting the variety of possible architectures alongside their experimental details. Note: All samples are illuminated under the following conditions: 100mW/cm2; AM 1.5 illumination.

No.	Type of photo-cathode	Co-catalysts	Method of deposition	Electrolyte	pH	Photocurrent density	Comment	Ref.
			ALD processed photo-cathodes					
1	FTO/Cu/Cu_2O/Ga2O3/TiO_2	RuOx	1. Sputtering of Cu 2. electrochemical anodization of copper-coated FTO + annealing 3. ALD of Ga2O3 4. ALD of TiO_2 5. Galvanostatic PEC deposition of RuOx	1.0 M Na2SO4 solution buffered with phosphate (0.1 M)	5	-10mA/cm^2 at 0 VRHE	highest yet achieved photo current Cu_2O nanowires for lager surface area	[19]
2	FTO/Au/Cu_2O/ZnO:Al/TiO_2	Pt	1. Thermal evaporation of Au 2. ECD of Cu_2O 3. ALD of ZnO:Al 4. ALD of TiO_2 5. Potentiostatically electrodeposited Pt	1.0 M Na2SO4 solution buffered with potassium phosphate (0.1 M)	4.9	-7.6 mA/cm^2 at 0 VRHE		[31]
			carbon-based protection layers					
3	FTO/Cu_2O/Cu/C		1. ECD of Cu_2O 2. Annealing of Cu_2O in O2 2. C deposition by aqueous solution coating of glucose + annealing in N2		5.5	-6.6 mA/cm^2 at 0 VRHE	Carbon protection layer	[53]
4	FTO/Cu_2O/PUA/TiO_2		1. ECD of Cu_2O 2. Spin-coating of PUA + annealing 3. Magnetronsputtered TiO_2	1 M Na2SO4	7	-2.8 mA/cm^2 at 0 VRHE	Polyurethan protection layer	[54]
5	FTO/Cu_2O/PI-200		1.ECD of Cu_2O 2. Spin-coating of PI + annealing	1 M Na2SO4	7	-1.8 mA/cm^2 at 0VRHE	Polyimid protection layer	[3]
6	Cu mesh/Cu_2O/Graphene		1. Cu-anodization 2. Dip-coating in GO + annealing in N2	1.0 M Na2SO4 solution buffered with potassium phosphate (0.1 M)	5	-4.8 mA/cm^2 at 0 VRHE		[55]
			nobelmetal free co-catalysts involved					
7	FTO/Cu_2O	Ni-CuBTC	1. ECD of Cu_2O 2. Solvothermal synthesis of Ni-CuBTC	0.5 M Na2SO4 buffered with 0.2 M PBS	5	-1.5 mA/cm^2 at 0 VRHE	Ni-CuBTC as co-catalyst, photosensitizer, protector	[2]
8	FTO/Au/Cu_2O	NiFe-LDH	1. ECD of Cu_2O 2. ECD of NiFe-LDH	0.5 M Na2SO4	6.5	-0.5mA/cm^2 at 0.33 VHRE		[56]
9	FTO/Cu_2O	g-C3N4	1. ECD of Cu_2O 2. Sol-gel synthesis of g-C3N4 + deposition on Cu_2O via electrophoretic deposition process	0.1 M NaNO3	7	-1.4 mA/cm^2 at 0.21 VRHE		[57]
10	FTO/Cu_2O/CuO	NixPy	1. ECD of Cu_2O 2.Thermal annealing of Cu_2O to CuO 3. Pulse-plating electrodeposition of amorphous Ni–P	0.5M Na_2SO_4	7	-3.2 mA/cm^2 at 0 VRHE		[58]

3 | Experimental approach and methods

The following chapter describes the experimental approach of the underlying thesis and the applied methods. The experimental setup to obtain the Cu_2O film as well as the synthesis of BDC-NH_2 MOF are explained in detail, followed by the construction of different architectures for Cu_2O-based photo-cathodes. Moreover, the addition of further protection layers and data evaluation for the performance measurement for PEC water-splitting are discussed.

3.1 Materials and Reagents

For the Cu_2O deposition, glass slides (Menzel-Gläser, 25x25mm, thickness: 1,0 mm) were purchased from Thermo Scientific. In addition, Indium tin oxide coated glasses (ITO, surface resistance 8-12 ohm/sq, 25 mm × 25 mm × 1.1 mm) were purchased from Sigma Aldrich. Further, Lactic acid in aqueous solution (90%) was from VWR. Sodium sulfate (Na_2SO_4, ≥ 99%) and Copper(II) sulfate pentahydrate ($CuSO_2$*$5H_2O$) were purchased from Sigma Aldrich. As a reference electrode for all experiments, RE-6 Ag/AgCl Reference Electrode (3 M NaCl gel) from Basi Research products was used. To prepare the electrolyte, Sodium sulfate (Na_2SO_4, ≥ 99%) and Kaliumphosphat (KH_2PO_4), and Natrium hydroxide pellets (NaOH) from Sigma-Aldrich were used.
For the BDCNH_2 synthesis, Copper(II) nitrate trihydrate ($Cu(NO_3)_2$*3 H_2O, 99%) from Thermo Scientific and 2-Aminoterephthalic acid ($C_8H_7NO_4$, 99%) from Alfa Aesar were purchased.
For MOF functionalization, Triethylamine (TEA, $C_6H_{15}N$) from Thermo Fischer Scientific and Perfluorooctanoyl chloride (C8ClF15O, 97%) from Thermo Fischer Scientific were used.
For the hydrophobic organic protection layer, Sylgard 184 Silicone Elastomer Kit was used from Dow Corning. Additionally, EtOH (abs., ≥99%, Thermo Fischer Scientific) and deionized water (DI) were used.

3.2 Preparation of the Cu_2O-based PEC cell

A PEC cell is usually composed of a photo-active material equipped with various overlayers to generate charge carriers that are swiftly transferred to the surface of the photo-cathode for the water-splitting reaction. The addition of layers of other materials can serve multiple purposes, such as for protection, fulfilling a catalytic role, and/or reduction of series resistance when employed as back contact. In order to construct the Cu_2O cell, which served as the stepping stone for the MOF synthesis, the following procedures were utilized:

(1) Sputtering. Through this process, which is of physical nature, a material is deposited by using ions (here Ar^+) to extract atoms from a pure material target and deposit them on the sample substrate. This allows for the creation of thin layers in the range of nm.

(2) Electro-chemical bath deposition (ECD). This process entails submerging the sample in a chemical solution and depositing the desired layer onto the samples by applying a deposition potential at a given process temperature.

(3) In-situ MOF synthesis. This process allows the direct growth of MOF crystals onto the surface of the substrate to ensure good adhesion between the material layers.

(4) Spin-coating. Via spin-coating it is generally possible to add layers of different natures onto various substrates with relatively thin thicknesses and ease for hydrophobic protection layers.

The production steps for the PEC cell are illustrated in Figure 3.1.

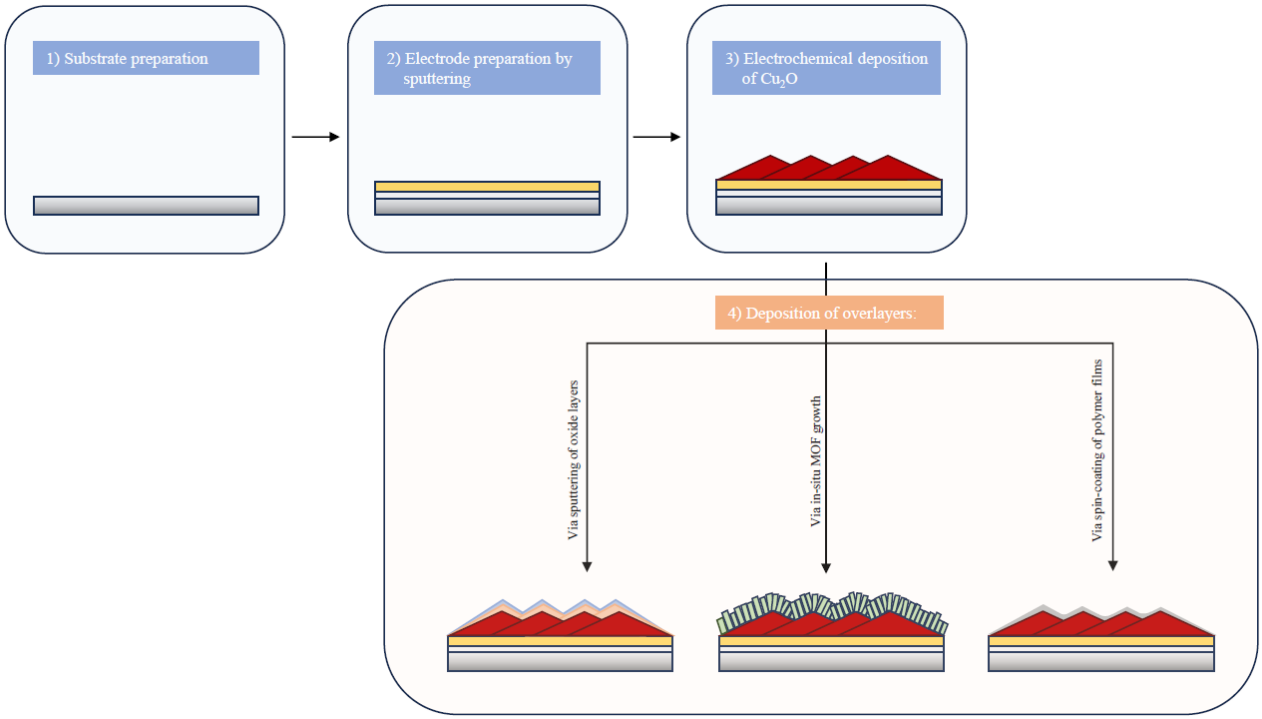

Figure 3.1: Schematic workflow for the preparation of the different cuprous oxide-based photocathodes. The first step includes the cleaning process, and the second step is the addition of the metallic back contact (Au). The third step is the deposition of Cu_2O on the gold-coated glass substrate, which is then used in the fourth step to deposit other layers. For the ITO substrate, the second step was bypassed, and the substrate was directly used for the ECD of Cu_2O after cleaning.

Each step will be discussed in detail in the following sections, with a particular focus on the in-situ MOF growth onto the Cu_2O film. Afterward, the finished devices were tested for performance and stability and underwent a series of material characterization methods such as XRD, XPS, FTIR, and SEM.

3.2.1 Substrate preparation and base layer sputtering

For the electrochemical bath deposition of Cu_2O, glass slides (25x25x25 mm microscopic glass squares) were first cleaned in the following manner: the glasses were carefully placed into a sample holder and immersed DI water containing ∼1 ml of Hellmanex III detergent. The sample holder was then placed into a sonication bath for 15 min at 40-50°C. Afterward, the procedure was repeated in pure DI water for 15 min at 30-40°C. Then, the glass slides were immersed in Isopropanol and sonicated for 15 min at 25-30°C. At last, the slides were washed with Isopropanol and dried with N_2 to ensure a clean surface. As for the ITO slides, the same treatment was applied.

After the cleaning process, it is crucial to add a metallic layer to establish the conductivity and enable electrons to flow into an external circuit, as the glass substrates do not inherently possess conductive properties. This was implemented by sputtering 10 nm thick layer of aluminium-doped zinc oxide (AZO) onto the cleaned glass substrates, followed by a 50 nm thick Au layer. While the former is necessary to ensure the adherence of the Au layer onto the glass surface, the latter serves as the conductive back contact for the PEC device. The parameters for all layers created via sputtering are summarized in Table 3.1 in Section 3.2.4.

3.2.2 Electrochemical deposition of Cu_2O

Preparation of the ECD solution

The electrolyte solution for the ECD of Cu_2O was prepared as follows: 0.2 M (24.969 g) Copper sulfate pentahydrate ($CuSO_4 \times 5H_2O$) was dissolved in 300 ml ultrapure milli-Q water, followed by adding 3 M (135.12 g) lactic acid. The solution was stirred constantly until the Cu crystals were fully dissolved. Then, ∼ 63 g NaOH pellets were carefully added, decreasing the pH from an initial acid value to a pH of 12.5. At ∼7, the solution undergoes a color change from blue to dark blue-violet increasing in depth as the pH declines. The lactic acid in the solutions serves as a chelating agent to stabilize the Cu^{2+} ions and prevents the formation $Cu(OH)_2$, which would precipitate and hinder the deposition of Cu_2O in the deposition solution. For the fine-tuning of the pH, a diluted NaOH solution of 0.1 M was used. During this procedure, the water bath was replaced at least twice to ensure sufficient cooling. A total volume of 500 ml was prepared, of which ∼150 ml was used from the stock solution to a beaker for the preparation of around 3-5 samples, while the rest was kept under constant stirring until it was thoroughly consumed.

Experimental set-up

The three-electrode setup represents the standard arrangements for all ECD experiments and includes a working electrode (WE), a counter electrode (CE), and a reference electrode (RE). Figure 3.2 a) displays a schematic illustration of the ECD set-up next to the real set-up b) in the laboratory.

a)

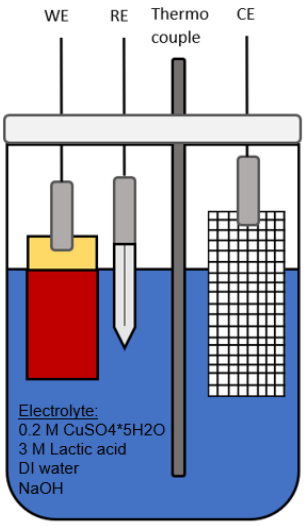

b)

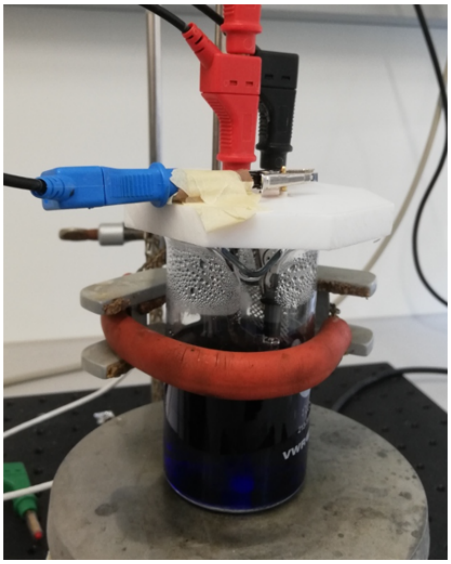

Figure 3.2: Experimental set-up for electrochemical bath deposition of Cu_2O: a) schematic illustration, b) laboratory set-up, with working electrode (WE), Ag/AgCl reference electrode (RE), thermocouple, and Pt mesh as counter electrode (CE), immersed in $CuSO_4$ electrolyte.

The conductive substrate (either AZO/Au or ITO) onto which the Cu_2O film was deposited acted as the WE, whereas a Pt-coated steel mesh served as the CE. An Ag/AgCl electrode (with a filling solution of 3 M NaCl) acted as a RE. All electrodes were connected to an AUTOLAB potentiostat and placed into a 250 ml beaker filled with 150 ml ECD solution. The solution was kept at a constant temperature of 50°C via the usage of a thermocouple connected to a hotplate for the automated regulation of the solution temperature. To avoid inhomogeneous deposition over the substrate area (most probably due to a disturbed mass flow), the ECD solution was not stirred during the actual deposition process but in between the depositions as well as during the heat-up sessions. The depositions themselves were conducted in the potentiostatic mode. Thus, the potential was kept constant with varying currents.

Linear sweep voltammetry

In order to select appropriate conditions for the potentiostatic deposition for the Cu_2O deposition on the specific substrate, a linear sweep voltammetry (LSV) measurement was performed. For this, the potential was ramped from 0 to -1 V vs. Ag/AgCl RE at a rate of 10 mV/s while the current was recorded.
Figure 3.3 illustrates the semi-logarithm of the current density j plotted against applied Ag/AgCl electrode potential for Cu_2O on Cr/ITO electrode obtained by the group of Dimopoulosa et al [59]. $\eta = (E - E_{eq})$ describes the activation overpotential. Furthermore, E_{eq} is the equilibrium potential, where the redox reactions happen at the same rates [59, 60] and is marked in red at $0.19V$.

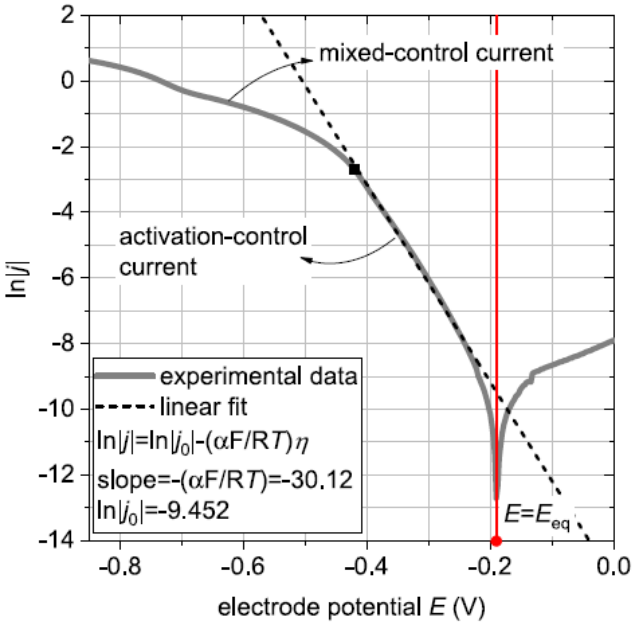

Figure 3.3: Current density on a semi-logarithmic scale vs Ag/AgCl electrode potential curve based on previous results in the lab for Cu_2O on Cr/ITO electrode [59] to visualize the mixed-controlled and activation-controlled region.

According to the Butler-Volmer equation, as the overpotential ($|\eta| \pm 50mV$) takes on large, negative values, the deposition current increases exponentially [59]:

$$|j| = |j_0| e^{[-(\frac{\alpha F}{RT})\eta]} \tag{3.1}$$

or written as:

$$ln(|j|) = ln(|j_0|)[-(\frac{\alpha F}{RT})\eta] \tag{3.2}$$

Here, j_0 represents the exchange current density, whereas the universal gas constant is $R = 8.3144598[J/mol*K]$, and the temperature is $T = 323K$ (at 50°C). The cathodic charge transfer coefficient α is dimensionless [59]. As shown in Figure 3.3, the slope of the linear fit from previous experiments from the group[59] shows -30.12, which yields a cathodic charge transfer coefficient of α=0.84. The potential regime that is activation-controlled can be generally described with the Butler-Volmer equation, as the reaction in this region is managed by the electrical charge transfer occurring at the surface of the electrode. However, this equation does not hold for the mass transfer from the bulk electrolyte to the electrode. This implies that outside the linear region, as marked in the plot, the potential current starts to slow down as the transportation of the mass to the electrode approaches its limits. At this point, the mixed-control region is entered with its own characteristics [59]. Well-defined crystals are obtained in the activation-controlled region, whereas depositions occurring in the mixed-controlled region lead to irregular and disturbed crystal formations due to limited mass transport. However, the mixed-controlled region also shines with higher deposition rates and a larger nucleation density. Particularly, the latter is of importance as it determines the minimum film thickness and the grain size of the film [59]. The generation of compact thin absorber films requires a high nucleation density, whereas larger grain sizes are desirable for their improved electrical properties. As the latter is achieved through low nucleation density, a trade-off situation is created [59, 61]. Everything considered, the optimal deposition potential should lead to compact, void-free thin films, with large grain sizes of the crystals[59]. In order to combine all these attributes, the ideal deposition potential should be as low as possible while still being part of

the linear regime of the LSV curve. The selected deposition potentials for the glass/AZO/Au substrates were set to be -0.3 V, whereas for the glass/ITO substrates, a dual-deposition approach was applied, where first a higher potential for -0.47 V was selected and then switched to the lower potential of -0.35 V as can be seen in Figure 3.4. This approach led to better Cu_2O layers for the glass/ITO samples, however, no difference for the glass/Au substrates and was therefore omitted for the latter.

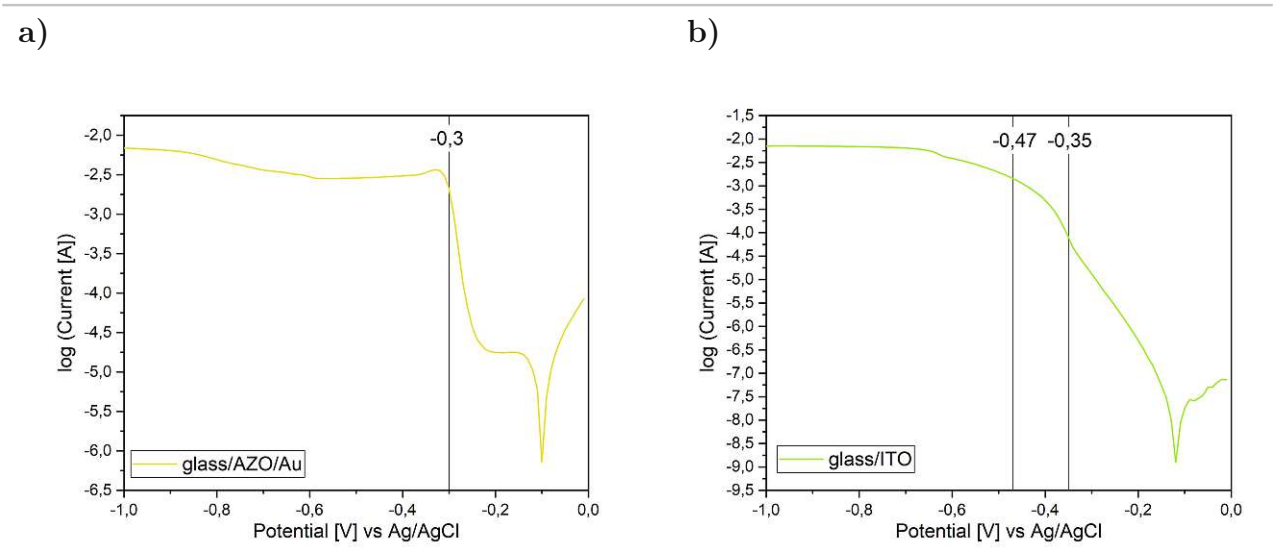

Figure 3.4: Linear sweep voltammetry (LSV) performed on glass/AZO/Au and b) glass/ITO substrate yielding different deposition potentials.

3.2.3 Deposition

The deposition process was performed by applying a certain deposition potential while the charge transfer onto the sample gets monitored simultaneously. When a certain charge was recorded by the in-build Autolab charge recorder, the process gets interrupted, and a film of a certain thickness onto the substrate was obtained.
The relation between these two entities is described through the Faraday law:

$$d = \frac{MQ}{nFA\phi} \tag{3.3}$$

Here, d represents the targeted film thickness, M represents the molecular weight of Cu_2O (M = 143.09 g/mol), n represents the number of electrons involved in the reaction (n = 2), and F is the Faraday constant (F = 96485.33289 C/mol). For the targeted thickness of 2.5 μm, a surface area of A = 2.25 cm^2, and the density ϕ of 6 g/cm^3 for Cu_2O, the charge at which the process concludes equals Q = -4.55 Cb. After the deposition, the samples were taken out from the solution and washed with deionized water to remove residual salts from the Cu_2O surface and dried a N_2 gun.
As aforementioned, Cu^{2+} ions in the electrolytic medium are stabilized by lactic acid and travel toward the surface of the WE. At the surface of the WE, the Cu^{2+} ions go through a charge transfer and get deposited in two steps: $Cu^{2+} \rightarrow Cu^{+} \rightarrow Cu^{0}$. The produced Cu^{+} exhibits low solubility in water solution and reacts with OH^{-} ions to form Cu_2O [62].
The possible mechanism for the electrodeposition process of Cu_2O can be written as fol-

lows [63]:

$$Cu^{2+} + e^- \rightarrow Cu^+ \quad (3.4)$$
$$Cu^+ + e^- \rightarrow Cu \quad (3.5)$$
$$2Cu^{2+} + 2OH^- \rightarrow Cu_2O + H_2O \quad (3.6)$$

3.2.4 Magnetron sputtering parameters

Magnetron sputtering is a physical deposition technique where ions are accelerated toward a target. Here, gaseous plasma is generated and confined in a chamber, that contains a material ('target') which will be deposited in the process. The target's surface gets then struck by the high-energy ions, causing atoms from the target surface to be ejected and to be deposited on a substrate to form a thin film [64] (see Figure 3.5).

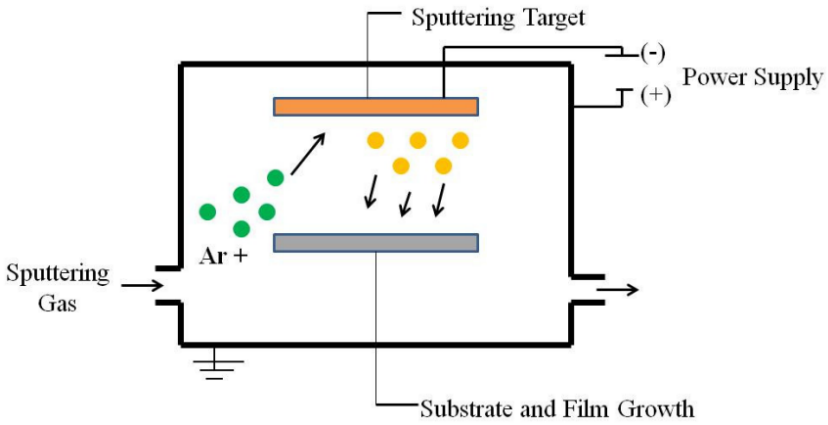

Figure 3.5: Schematic illustration of the DC sputtering procedure [65].

As the sputtering deposition process starts, a deposition chamber first gets evacuated to a high vacuum so that the presence of potential contaminants as well as partial pressures of all background gases are minimized. After the base pressure is reached, the chamber gets filled with inert sputtering gas (in this case Argon). High voltage is applied between the cathode and the anode, and electrons are driven away from the cathode, which is commonly placed behind the target. As the accelerated electrons crash into the atoms of the sputtering gas, they become ionized. Due to their now positive charge, the gas ions are then directed toward a negatively charged cathode, which leads to high-energy collisions at the target surface. Each of these collisions leads to the ejection of atoms from the target surface, which exhibits high enough kinetic energy to travel through the high vacuum and arrive at the surface of the substrate, where it gets deposited [64].
The sputter sources are either supplied by direct current (DC) or radio frequency (RF) power. Traditional DC sputtering acts as a cost-effective way to apply metal target coatings but is limited when it comes to dielectric target materials - as they would take on a polarized charge. In this case, RF mode is applied. By alternating the applied voltage in cycles, Ar+ ions can either collide with the target creating the deposition atoms at a negative bias, or electrons are accelerated to the target neutralizing the built-up charge at a positive bias [66].

The sputtering process parameters are summarized for all layers in Table 3.1. All samples were deposited in Ar atmosphere with a base pressure of 1.2×10^{-7} mbar. The samples were transferred from a load lock to the actual deposition chamber when pressure within the load lock reached at least 2×10^{-6} mbar. For sputtering overlayers (Zinc oxysulphide Zn(O,S) with

S = 20at.% (ZNO)) as buffer layer and Niobium doped TiO_2 (NTO) as protection layer), Kapton tape was used to hold the substrates in place, and a glass slide was used to protect their conductive parts, as can be seen in Figure 3.6.

Figure 3.6: Samples fixated on the sample holder with Kapton tape.

Table 3.1: Overview of the sputtering parameters used for all samples.

Material	*Target*	*Power [W]*	*Pressure [ubar]*	*Rate [nm/s]*	*Sputtering time [s]*	*Thickness [nm]*	*Purpose*
AZO	C4T6	60	4	0.29	35	10	Adhesion layer
Au	C5T1	20	2	0.8	63	50	Back-contact
ZnO	C5T5	100	5	0.174	287	50	Buffer layer
NTO	C4T1	120	7	0.138753086	361	50	Protection layer

3.3 Synthesis of Cu-BDCNH$_2$

The main idea for bringing in MOFs is to implement them as overlayers onto Cu_2O in order to make use of their favorable properties, such as improved light absorption properties and increased surface area for reaction, as has been mentioned in the Introduction section. In literature, the BG of Cu-BDCNH$_2$ is reported to be 2.3 eV (see Figure 3.7 [67]). Up until now, Cu-BDCNH$_2$ has been implemented as a photo-cathode for photo-electrocatalytic CO_2 reduction [52] with no reported BG alignment.
In general, the addition of amine groups should lead to an increase of the light absorption abilities of the MOF, reduce the BG (compared to its amine-free BDC counterpart as ligand), and enhance the charge separation. This leads to a decline in electron-hole recombination events [68]. Moreover, the addition of -NH$_2$ groups gives rise to the option of further functionalization of the MOF in a post-synthetic modification, as has been explored by Cohen et al. [69] and Chin et al. [70].

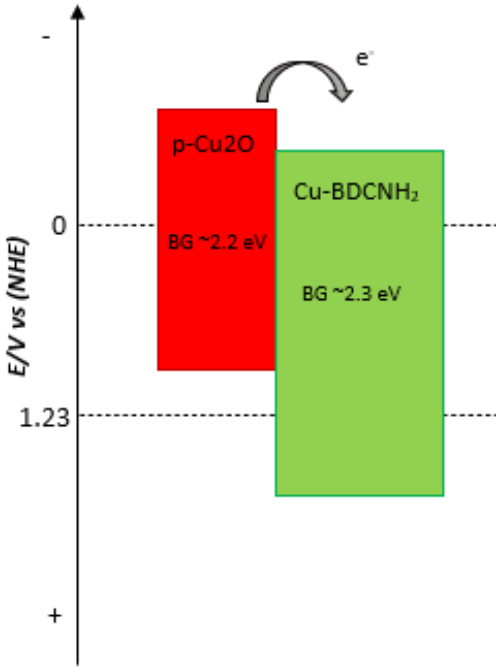

Figure 3.7: Band gap alignment for Cu-BDC reported in literature [67].

As for PEC water-splitting, a uniform MOF coating of relatively small thickness is desirable, a sufficient understanding of the MOF formation mechanism is required. Furthermore, the addition of surfactants can also assist in the controlled growth of MOFs, even yielding 2-D materials, as has been reported by Gao et al. [71], whose team prepared ultrathin 2D metal–organic framework nanosheets using polyvinylpyrrolidone (PVP). However, the use of PVP may block some of the active sites of the MOF nanosheets. Further, thickness control of the MOF sheets is difficult to achieve in this manner [72]. Due to this, the in-situ synthesis of MOF nanosheets starting from metal substrates has been developed without the usage of surfactants, allowing the growth of uniformly distributed MOFs nanosheets on the substrate [73].
Since Cu_2O and not metallic Cu serves as the precursor material for the MOF growth, the synthesis of Cu-BDCNH$_2$ needed proper adjustment. For this, a proper grasp of the growth mechanisms is of utmost importance and is as follows [74]:

During the synthesis approach, Cu^{+} gets gradually released from Cu_2O, which acts as metal ion source and is further oxidized by dissolved oxygen to Cu^{2+}. In the meantime, DMF decomposes to dimethyl amine, a Brønsted base, and deprotonates carboxyl groups of the $BDC(NH_2)$ ligand, which is then coordinated by the Cu^{2+} and serves as the metal node for the MOF.
According to literature [74], the shapes of Cu-MOFs from Cu_2O mainly depend on the oxidative dissolution rate of Cu_2O as well as the coordination rate between Cu^{2+} and $BDCNH^{2-}$. Thus, the mechanism of Cu-$BDCNH_2$ formation can be divided into three main parts[74]: (1) Cu^{+} needs to be released from the Cu_2O source, (2) followed by their oxidation to Cu^{2+} by oxygen, which is dissolved in the electrolyte. (3) Cu-$BDCNH_2$ crystals are formed by coordination reactions of Cu^{2+} and the ligand units [74].

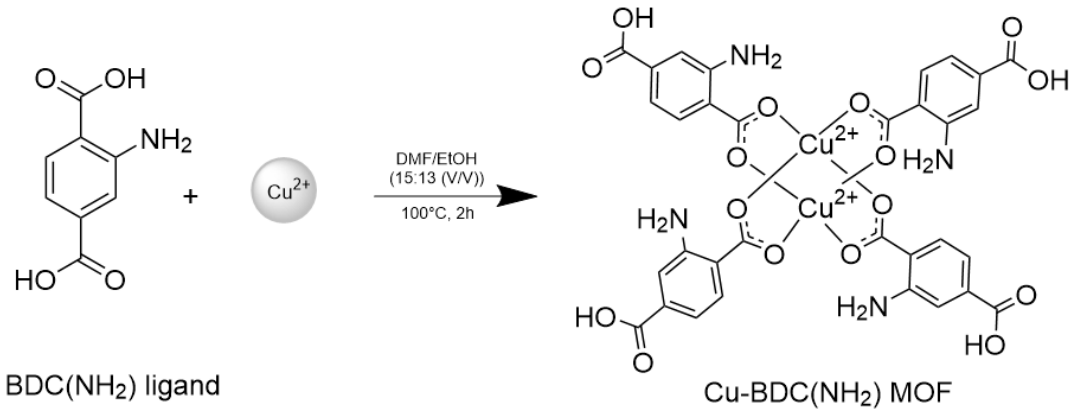

Figure 3.8: Reaction of $BDCNH_2$ ligand with Cu^{2+} ions yielding Cu-$BDCNH_2$.

For the MOFs to grow on the substrate, the dissolved Cu^{2+} ions need to stay in close proximity. This issue can be addressed by adding less-polar organic solvents to adjust the polarity of the reaction solvent downwards, leading to a lower diffusion rate of Cu^{2+} and thus, a higher metal ions concentration near the surface of the substrate, generating a polycrystalline MOF film in an inter-growth fashion [75].

3.3.1 Investigated parameters for the MOF synthesis

In-situ synthesis in glass vial

Various parameters were tested in order to determine the most suitable conditions. For this, a field test was first conducted, where the Cu_2O substrates were cut into smaller pieces and divided among 20 ml glass vials. A 0.1 M $BDCNH_2$ ligand solution was prepared in DMF and sonicated for 5 min to obtain a homogenous solution. 15 ml of ligand solution was placed into the glass vials and onto a heating block at different temperatures. An aluminum foil was placed over the glass vials and then the vials were left standing for different time ranges. The addition of H_2O to DMF was also tested and should increase the polarity of the solvent, as discussed previously. Table 3.2 provides an overview of the tested conditions in glass vials. Afterward, the substrates were rinsed several times with ethanol and DI water and dried under argon, and ultimately placed in the oven for 2 h at 100°C to completely dry.
Figure 3.9 presents the results of the MOF synthesis of selected samples. While the addition of water leads to bulkier MOF crystals which are in accordance with the literature, they vary greatly in form and shape. Furthermore, since only the synthesis after 65 h showed a reasonable

Table 3.2: Tested parameters in the glass vial.

Sample name	*Time [h]*	*Temp.[°C]*	*Ligand Conc [mol/L]*	*Solvent*	*Addition*
SG_001_BDCNH2_1	15h	70	0.01	DMF	-
SG_001_BDCNH2_2	15h	70	0.01	DMF	3 eq H2O
SG_002_BDCNH2_1	65h	70	0.01	DMF	-
SG_002_BDCNH2_2	65h	70	0.01	DMF	1 eq H2O
SG_002_BDCNH2_3	65h	100	0.01	DMF	-
SG_002_BDCNH2_4	65h	100	0.01	DMF	1 eq H2O

amount of MOFs on the Cu_2O surface, the synthesis was in dire need of optimization to lower the reaction time. Thus, the reaction in glass vials was dismissed and further continued in the autoclave.

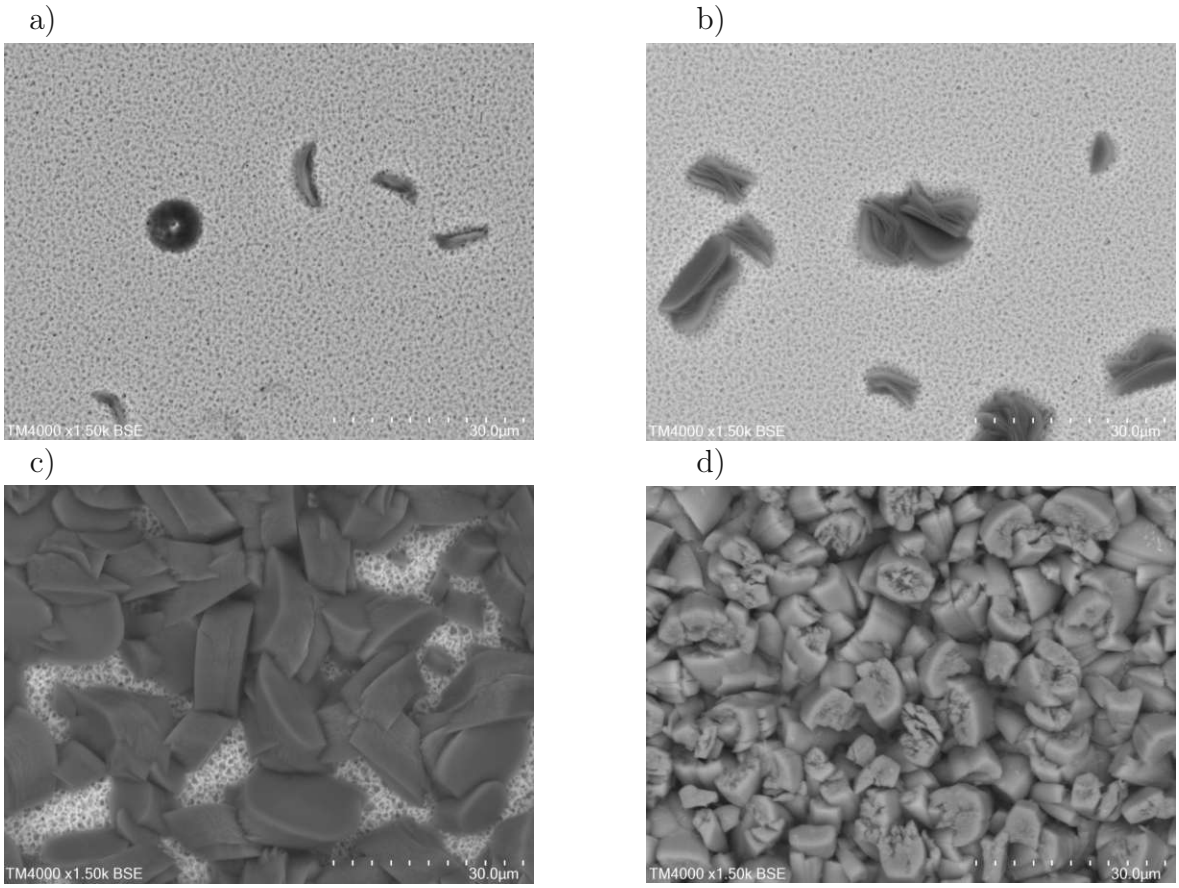

Figure 3.9: SEM pictures of the a) SG_001_BDCNH2_1, b)SG_001_BDCNH2_2, c) SG_002_BDCNH2_2, and d) SG_002_BDCNH2_3 obtained under different reaction conditions.

In-situ synthesis in the autoclave

The following in-situ synthesis was developed: First, a copper-nitrate solution (50 mmol/L of $Cu_2(NO_3)_2$ in deionized water) was prepared, sonicated for 10 min to obtain a homogeneous solution, and then placed onto a heating block for 10 min at 30°C to ensure the controlled temperature of the solution. In the meantime, the Cu_2O substrates were cleaned with ethanol, deionized water, and again ethanol to ensure that dust and other contaminates were removed and dried at 100°C for 5 min in an oven. Then the Cu_2O substrate was immersed in the copper-nitrate solution for 2 h. During this time, the ligand solution was prepared: the $BDCNH_2$ (0.2 M) was dissolved in 18 ml of solvent, sonicated for 5 min, and transferred in a 50 ml Teflon vessel. The solvent was a mixture of N, N-dimethylformamide (DMF), and absolute ethanol (EtOH) in different ratios (9:9, 14:4, and 15:3), where 15:3 yielded the best results. The Cu_2O substrate was placed into the container together with the mixed ligand solution, swiftly sealed, and transferred to a 50 mL stainless steel autoclave. The autoclave was heated at 100°C for 2 h. Afterward, the substrate was taken out, washed with ethanol, and dried at 100°C for 1 h. Figure 3.12 illustrates the synthesis route in detail.

Figure 3.10: Applied synthesis route for the growth of Cu-$BDCNH_2$ onto Cu_2O after several attempts.

Figure 3.11 illustrates the morphologies for the prepared MOF samples with different ratios of DMF/EtOH (V/V).

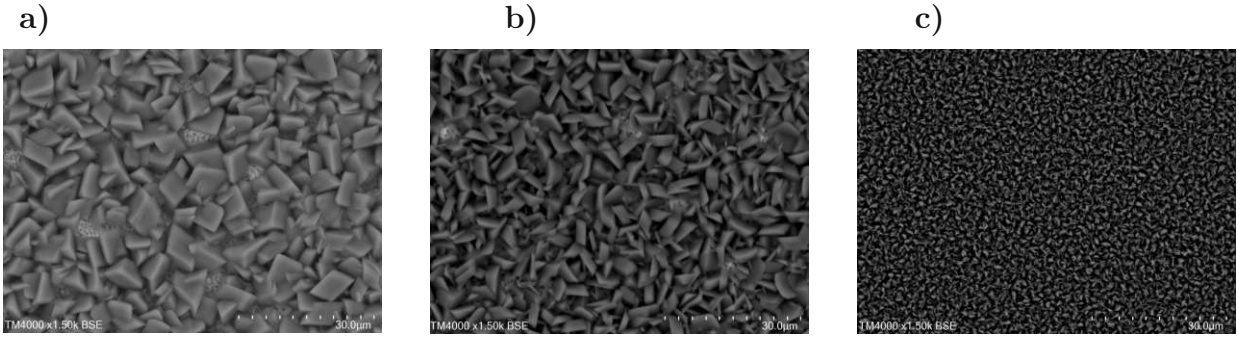

Figure 3.11: SEM pictures of MOF synthesis with a) 9:9, b) 14:4, c) 15:3 DMF/EtOH (V/V).

3.3.2 Post-synthetic modification

The properties of amine-containing MOFs can be readily altered through the post-synthetic modification (PSM) approach, which became a vital tool for developing diverse systems exhibiting different physical and chemical properties. It has already been reported that the physical properties (such as hydrophobicity) of amine-functionalized MOFs can be successfully altered by introducing hydrophobic alkyl chains utilizing PSM for enhanced moisture

resistance. The group of Cohen et al. [69] successfully demonstrated the integration of alkyl groups of different lengths within isoreticular metalorganic frameworks (IRMOFs), shielding the MOFs, that were previously moisture-sensitive by enhancing their hydrophobicity and even achieving superhydrophobic properties for MIL-53(Al)-NH_2. A similiar effect of increased hydrophobicity is desired for Cu-BDCNH_2. Here an adjusted version of the post-synthetic modification reported by Chin et al. [70] has been implemented and is as follows:

For the functionalization, the substrates were placed in a vial and evacuated overnight before being placed into the glovebox. 5 ml THF was added into the vial, followed by 0.5 ml pentadecafluorooctanyol chloride, the vial was capped afterward. Outside the glovebox, an equivalent amount of TEA was added to the vial. A yellowish precipitate formed right away after the addition of TEA. The vial was swirled and left to react for 3 h at RT. Then the substrates were washed with EtOH and dried at 100°C for overnight.

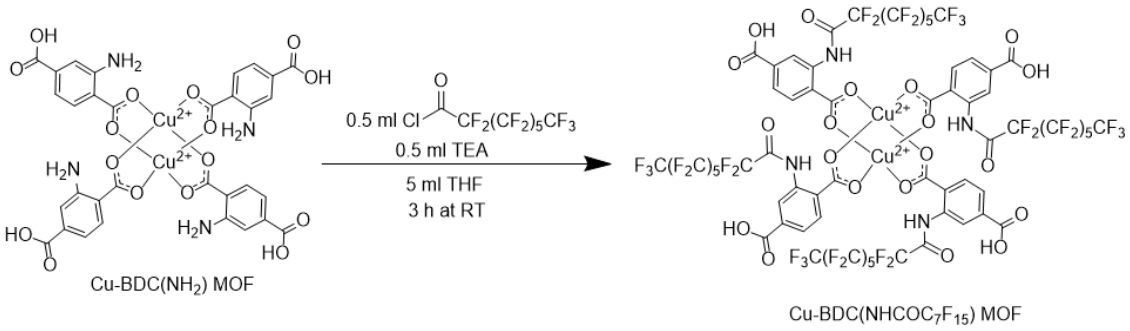

Figure 3.12: Proposed functionalized MOF material after post-synthetic modification.

3.4 Addition of hydrophobic protection layer

The spontaneous self-deactivation due to fast photo-induced corrosion is one of the main disadvantages concerning Cu_2O-based photo-cathodes. The redox potentials of Cu_2O fall in between its VB and CB levels, which means that Cu_2O can fall victim to self-reduction (Cu^{+1} to Cu^0) or self-oxidation (Cu^{+1} to Cu^{+2}) reactions, when illuminated with light, because of the generated charge carriers [54]. As the deactivation of Cu_2O is strongly connected to protons, the first step to achieve enhanced stability for cuprous-based electrodes is to ensure that protons and proton donors are isolated from Cu_2O [54], which is achieved by employing coatings on Cu_2O. While previous studies mainly focus on coating Cu_2O with other semiconducting materials such as TiO_2 and NiO_x to isolate the electrolyte solutions from Cu_2O surface, it is also reported that although the stability is indeed improved to a few hours, the results are still far away from the necessary requirements (days or weeks) to implement these techniques in the industry. Hence, with semiconducting materials, the problem appears to be only delayed but not solved [54].
The issue appears to be the following: the formation of oxide-based protection layers occurs mainly under island growth. These lead to holes in the protection layer, rendering the underlying semiconducting materials partially unprotected. Even in the presence of macroscopically dense oxide films on top of Cu_2O, the liquid molecules are still capable of reaching the Cu_2O surface by passing through the micropores, making use of the "capillary effect". In addition, oxides, like TiO_2, are relatively hydrophilic, further increasing the "capillary effect". To avoid this, applying a protective layer that is both dense and hydrophobic appears to be a promising route to improve the stability of Cu_2O [54]. In this regard, the group of Li et al. [54] prepared

a polymer-based protection layer by spin-coating a 50 nm thick polyurethane (PUA) layer on top of Cu_2O. In combination with Pt as a co-catalyst, the composite material achieved a photo-current of -5.5 mA/cm^2 at 0 V_{RHE}. Another group introduced the polymer polyimide (PI) as a protection layer again via spin-coating and achieved a current density value of 1.8 mA/cm^2 at 0 V_{RHE}, a value 40 times higher than bare Cu_2O [3]. Here, a polydimethylsiloxane (PDMS) layer was spin-coated on top of Cu_2O to create a similar effect:
Silicone base (Sylgard 184) was mixed with 10wt% of crosslinker in a 100 ml plastic beaker and stirred for 1 min at around 900 rpm to obtain a homogeneous solution. The beaker was covered with Alu-foil and put in a desiccator, where it was degassed around five times. Afterward, diluted solutions of PDMS with Toluene were prepared. The substrates were spin-coated with 100 ul of PDMS solution and cured for 1 h at 100°C.
The following PDMS concentrations were prepared: 0.1 wt%, 1 wt%, 10wt%. Tested coating speeds: 5000 rpm (2500 rpm/s), with 100 rpm as the spreading step beforehand. In order to spin-coat the samples, the substrates need to be stuck onto a glass slide of suitable size.

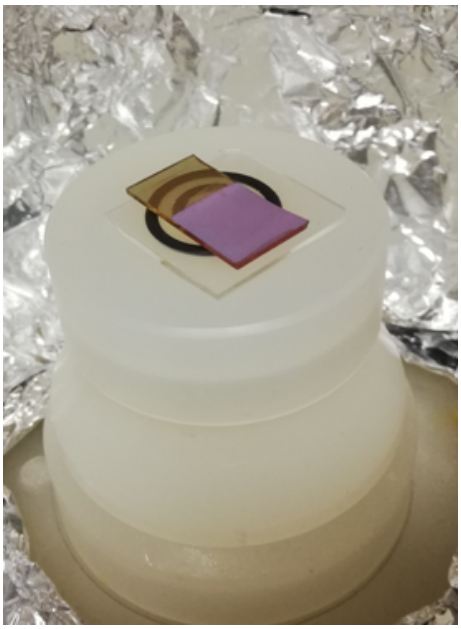

Figure 3.13: Cu_2O photo-cathode in the spin-coater machine.

3.5 Data evaluation

3.5.1 PEC water-splitting performance and stability

All samples were tested for PEC water-splitting. Here, the same three-electrode set-up was used for the deposition procedure: the substrate acted as the WE, a Pt-coated mesh served as the CE, and an Ag/AgCl electrode as the RE. The majority of the experiments were examined under chopped illumination (light intensity 100 mA/cm^2, AM 1.5G spectrum) utilizing either linear-sweep voltammetry (LSV) to test obtained photo-current density as a function of the applied potential or chrono-amperometry (CA), to analyze the stability of the photo-current density at a specific potential over different time periods. All samples were covered with a mask, as visible in Figure 3.14. This was done to ensure that only a specific area (A = 0.19625 cm^2) of the photo-cathode was illuminated to calculate the respective current density for the same area size. Then, the photo-cathodes were immersed into the PEC electrolyte solution, consisting of 0.5 M sodium sulfate, and 0.1 M Potassium dihydrogen phosphate at ph 5 and

7. By applying Eq. 3.7 it is possible to convert the potential vs Ag/AgCl ($E_{Ag/AgCl}$)electrode to potential vs RHE (E_{RHE}).

$$E_{RHE} = E_{Ag/AgCl} + 0.059 \times pH + E_{RE} \tag{3.7}$$

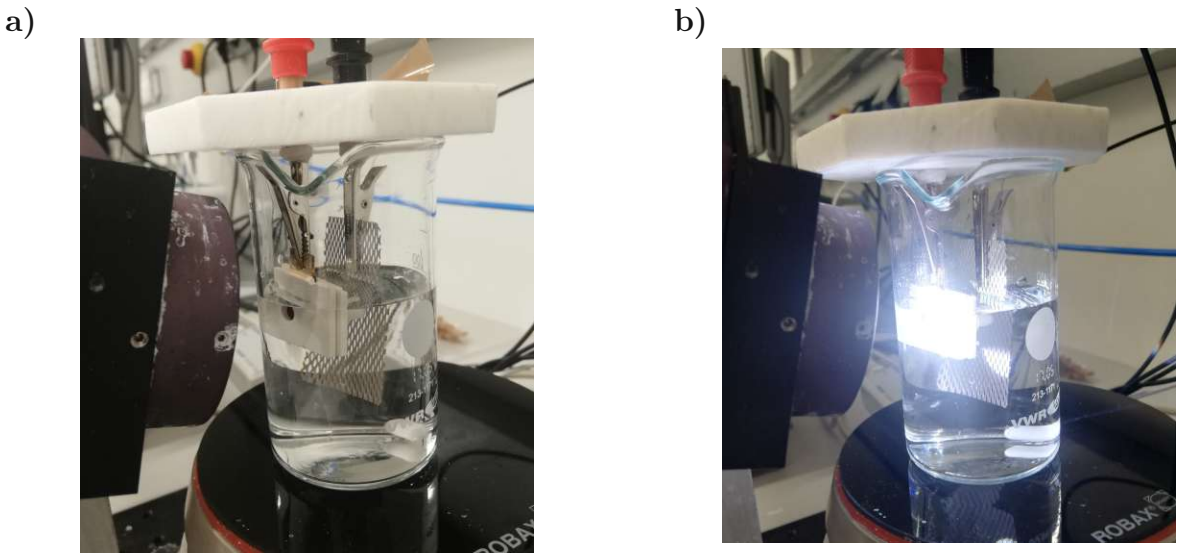

Figure 3.14: Experimental set-up for measuring PEC water-splitting performance: a) without light illumination, b) with light illumination. The photo-cathode faces the light source with a specific surface area exposed, while the remaining parts are covered with a mask. A Pt-coated mesh serves as the WE, and an Ag/AgCl electrode acts as the RE.

3.5.2 Sample characterization

X-ray diffraction (XRD)

X-ray diffractograms (XRD) were recorded at an incidence angle of $\omega = 5°$ employing Cu-Kα radiation on a ThermoFisher Scientific ARLEquinox 100 to observe the film crystallinity.

X-ray photo-electron spectroscopy (XPS)

XPS data was acquired on a Thermo Scientific Nexsa Photo-electron Spectrometer employing Al-Kα radiation. XPS was performed on a spot size of 400 µm with an energy step size of 0.1 eV.

Scanning electron microscopy and energy dispersive X-ray spectroscopy (SEM-EDS)

Scanning electron microscopy and energy dispersive X-ray spectroscopy (SEM-EDS) SEM-EDS measurements were conducted on a Hitachi TM4000 Tabletop Scanning Electron Microscope equipped with an Oxford Instruments Aztec EDS. Furthermore, Scanning electron microscopy was performed at an acceleration voltage of 5 kV and with an in-lens detector using ZEISS Ultra 40.

Fourier-transformed Infrared spectroscopy (FTIR)

To determine the band gap, a Fourier-transform infrared spectroscopy (FTIR, Bruker Vertex 70) was employed. The analysis was conducted in reflectance mode at an incidence angle of

13°. GaP served as the detector, whereas a sputtered Au layer on Si substrate was employed as a reference. All measurements were conducted at room temperature. Additional attenuated total reflection Fourier-transform infrared spectroscopy (ATR-FTIR) measurements were conducted on a Bruker VErtex 70 spectrometer equipped with a diamond ATR unit "Golden Gate" at 128 scans per sample.

Contact angle measurement

Contact angle measurements were performed on a Krüss Drop Shape Analyzer DSA30S paired with ADVANCE software at 20°C and ambient humidity. The substrates were placed on the measuring stage, and a 5 µl droplet of milli-Q water as probing liquid was manually dispensed with a pipette. Then, the substrate was moved, the droplet was removed using a paper towel, and the measurement was repeated with a new droplet at a different spot. The reported values are a mean of at least 3 measurements alongside their standard deviation. The drop shape was fitted by elliptical fit, and the baseline was determined manually.

4 | Results and Discussion

In this chapter, the experimental results of all investigated architectures for Cu_2O-based photo-cathodes are evaluated and discussed in detail. All composites are tested for their PEC water-splitting performance and stability in the form of their respective photo-current density and capability of maintaining a certain photo-current over different time periods. Additional characterization techniques are used to identify the components and make further assumptions about their performance. The synthesis procedure of Cu-$BDCNH_2$ and its post-synthetic modification are discussed, and its usage as overlayers for Cu_2O-based photo-cathodes will be evaluated.

4.1 Morphologies and chemical compositions

4.1.1 Cu_2O deposition on glass/Au and glass/ITO substrates

For the deposition of Cu_2O on glass/Au, a potential of -0.3 V vs Ag/AgCl was chosen. Compared to this, a dual deposition approach was implemented for the deposition of Cu_2O on glass/ITO, as can be seen in Figure 4.1 a). Here, a higher potential of -0.47V vs Ag/AgCl was applied until a transfer charge of -2.275 Cb (equivalent to 1.25 μm layer thickness) was recorded by the Autolab system (Nova 1.2), followed by a lower potential of -0.35 V vs Ag/AgCl. The deposition stopped at -4.5 Cb, which corresponds to 2.5 μm in layer thickness, for both cases. While the deposition of Cu_2O onto glass/Au took around 50 min, the deposition time on glass/ITO lasted around 57 min.
While the dual approach led to more uniform Cu_2O layers on glass/ITO, the same effect was not observed for the deposition on glass/ITO, thus, a single deposition approach was used. The difference in the deposition of Cu_2O on either glass/Au or glass/ITO does particularly reflect in the initial deposition process, as visible in Figure 4.1 b): the nucleation point (the point where the first crystal layer is formed, leading to a drastic increase in the current) is reached within ~7 s, whereas it took ~120 s to reach a similar stage for glass/ITO. The slower deposition, especially in the beginning, appears to be a crucial moment in obtaining high-quality Cu_2O films.

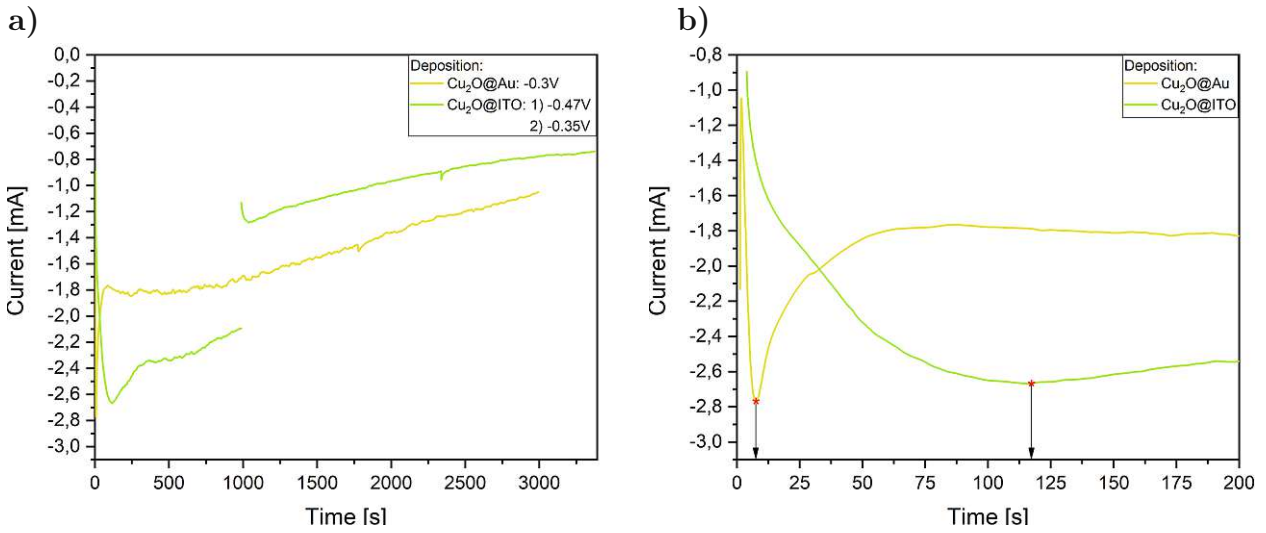

Figure 4.1: Deposition curves obtained via chrono amperometry for a) the whole deposition process and b) the first 200 s to observe the nucleation point of Cu_2O for both substrates.

In general, both approaches lead to Cu_2O films of bright red color, as illustrated in Figure 4.2. For enhanced conductivity in the PEC test, the ITO substrate was additionally painted with silver paste (see Figure 4.2 b)) and left to dry for 3 h.

Figure 4.2: Cu_2O deposited on a) glass/Au, b) glass/ITO.

The appearance of the prepared Cu_2O films were characterized by SEM, as displayed in Figure 4.3. The cross-section image of Cu_2O on glass/Au shows the expected of 2.5 μm from the total charge flow of -4.55 Cb during deposition, which is slightly exceeded by 0.2 μm depending on the point of measurement. The structure of the Cu_2O layer near the Au film reveals many crystal nuclei growing in a thin and columnar manner while steadily growing larger as they approach the surface. A general comparison of the Cu_2O film deposited on glass/Au and glass/ITO reveals that the deposition on glass/ITO usually produces better quality films compared to the deposition on glass/Au, where the former displays the expected cubic crystal structure of Cu_2O, whereas the latter rather shows pyramid-like shape Cu_2O crystals. The reason behind this behavior could be due to the slower nucleation of the Cu_2O crystal and their development into the cubic crystal structure, while the deposition on Au as substrate might be too rapid to properly develop cubic crystals, creating a slightly less ideal Cu_2O surface.

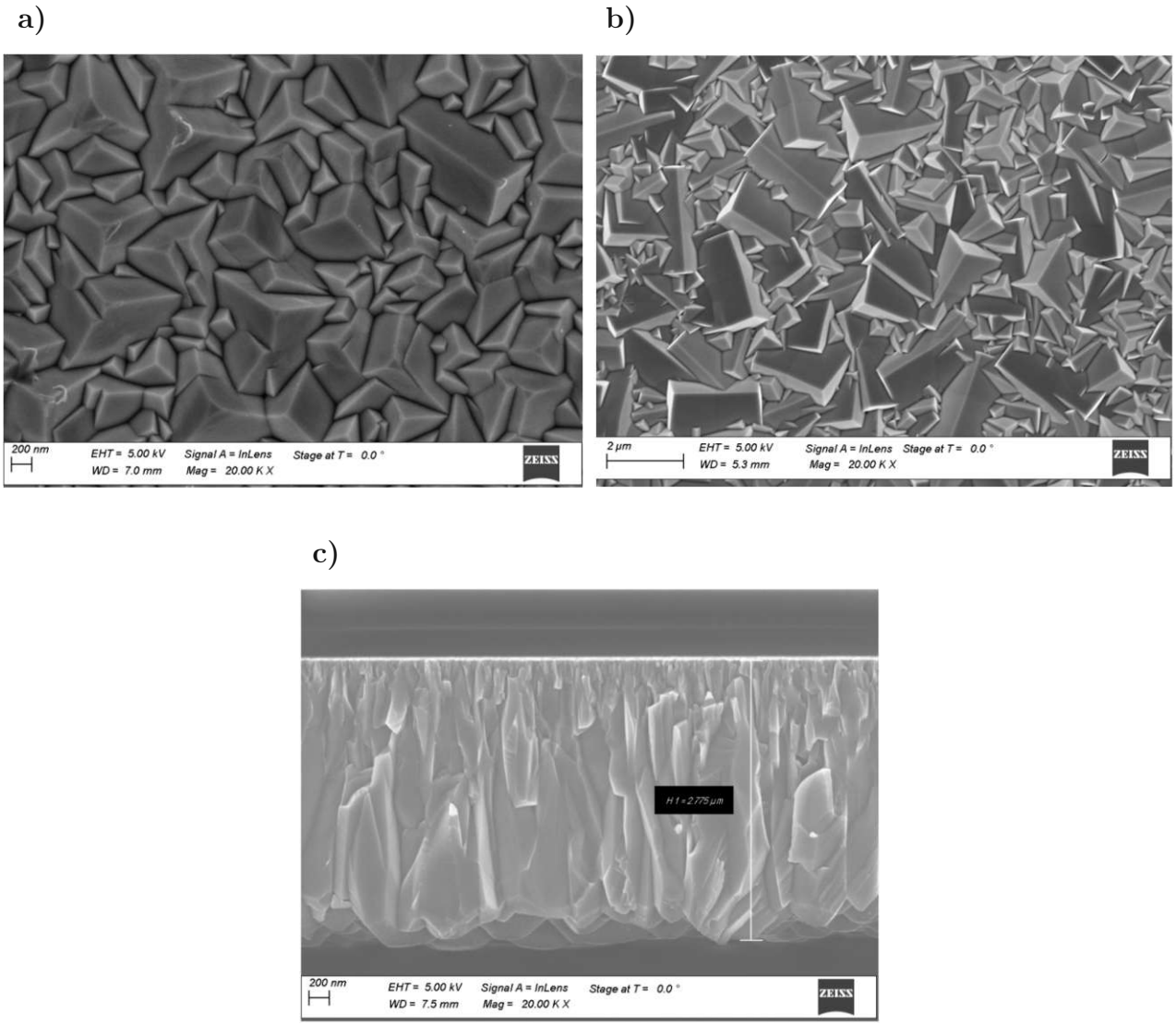

Figure 4.3: SEM picture of a) Cu_2O on glass/Au, b) Cu_2O on glass/ITO. c) displays the cross-sectional SEM of Cu_2O on glass/Au together with the measured thickness of around 2.7 μm.

To analyze the quality of the Cu_2O deposition on the different substrates X-ray diffractometry (XRD) was applied. Figure 4.4 displays the as-prepared Cu_2O films on ITO and Au measured at an angle of $\omega = 5$, along with a reference pattern for cuprous oxide (reference card no. 96-101-0942). The experimentally derived peaks align well with the characteristic peaks of Cu_2O emerging at 36.6, 42.5, 61.7, and 73.9 degrees presented by the reference.

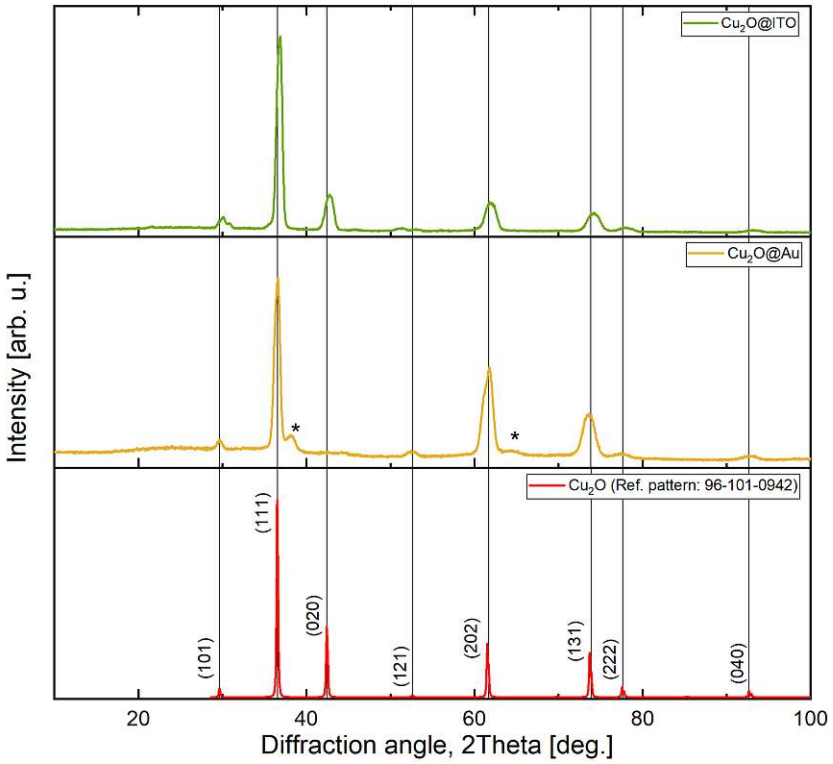

Figure 4.4: XRD of Cu_2O on Au and ITO with a reference pattern of Cu_2O, the marked parts belong to Au.

However, a direct comparison of the XRD spectra obtained for Cu_2O on glass/Au and glass/ITO reveals that the (111) peak, which is the most stable, thus, the most desired phase of Cu_2O, is more prominent for the latter. Hence, it becomes evident that the Cu_2O deposition of glass/ITO produces more desirable films compared to glass/Au. In general, the preferential growth orientation for Cu_2O lies in the (111) direction. The preferential growth direction can usually be explained by taking a closer look at the surface energy of the corresponding faces: surfaces of high energy grow faster, while surfaces of lower energy grow slower. Thus, the area of high surface energy faces decreases, whereas low energy surface areas increase over time. As the (111) orientation of Cu_2O is commonly referred to as the face with the lowest surface energy, thus, the most stable one, the (111) face should become the dominant face [76]. This conversion of high to low surface energy faces appears to be more efficient when Cu_2O is deposited on ITO compared to Au. The reason behind this might be the overall slower deposition rate of Cu_2O on ITO compared to Au, leading to better-defined crystals, which reflects in the deposition curves - particularly in the first seconds of the deposition (see Figure 4.1 b)) - and could be attributed to the overall lower conductivity of ITO.

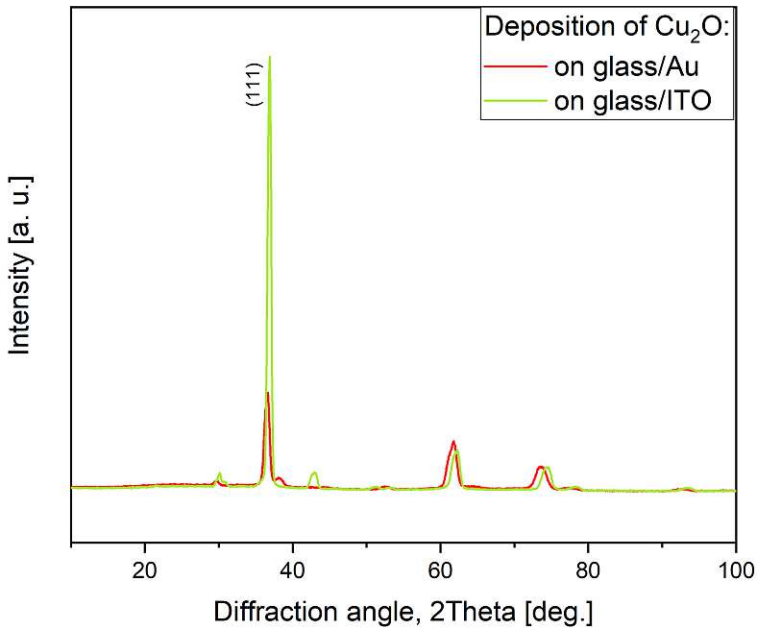

Figure 4.5: Direct comparison of the XRD spectra of Cu_2O on Au and ITO.

4.1.2 MOF on Cu_2O and post-synthetic modification

The development of the prepared Cu-BDCNH$_2$ samples is characterized by SEM. By adjusting parameters such as temperature, reaction time, reaction medium, and container, it was possible to enhance the MOF growth starting from an initially poor coverage to a uniform coating covering the Cu_2O film, as visualized in Figure 4.6. A general observation in the close-up view shows a large number of MOFs displaying uniform thickness standing upright on the substrate. The Cu-BDCNH$_2$ crystals provide a much rougher surface for photo-cathode compared to the blank Cu_2O, implying the presence of a large number of active sites for further reactions and enhanced surface area.

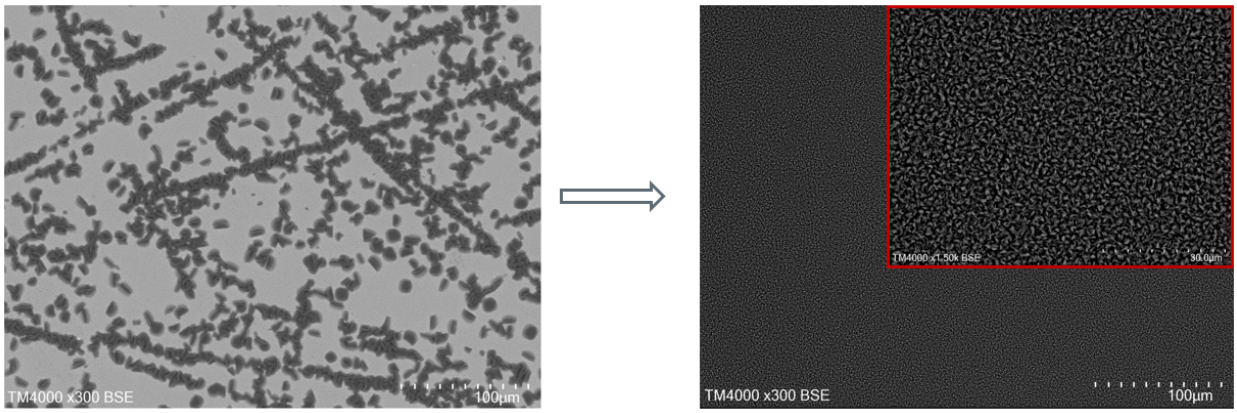

Figure 4.6: Development from poor MOF coverage on Cu_2O to uniformly distributed MOF-coating on Cu_2O on Au.

According to cross-section images (see Figure 4.12), the average thickness of the MOF film is 5 μm, while 2.2 μm Cu_2O remains. Hence, it can be hypnotized that around 0.3 μm Cu_2O is sacrificed in the synthesis process. However, since around 2 μm of Cu_2O are necessary to obtain sufficient absorption of the incident light, this finding does not pose any problems.

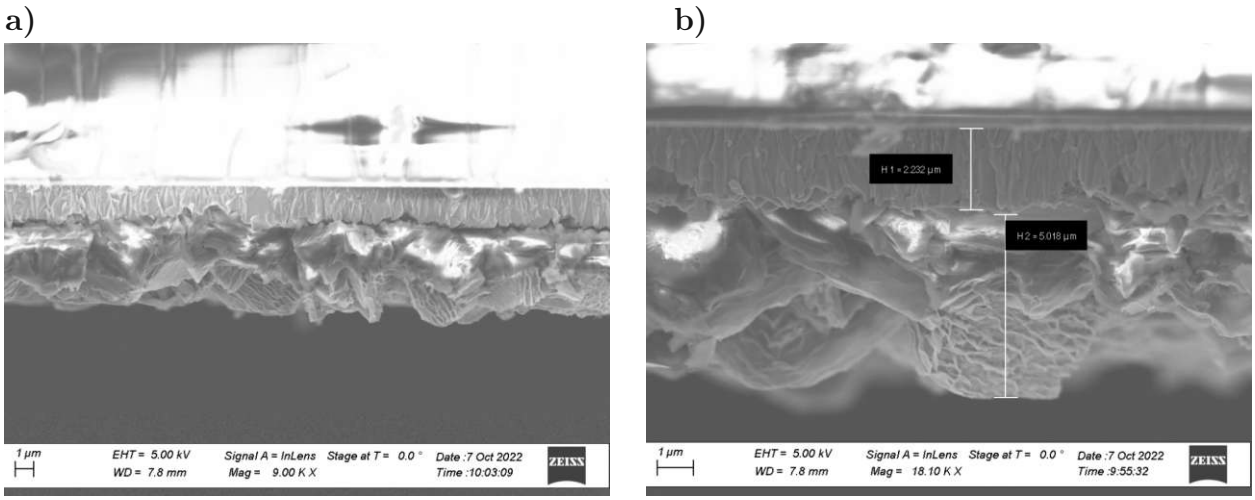

Figure 4.7: Cross-sectional SEM of Cu-BDCNH$_2$ on Cu$_2$O at ITO at different magnifications. For the MOF observation under SEM Zeiss, a thin Au layer of 5 nm was sputtered onto the substrate layer.

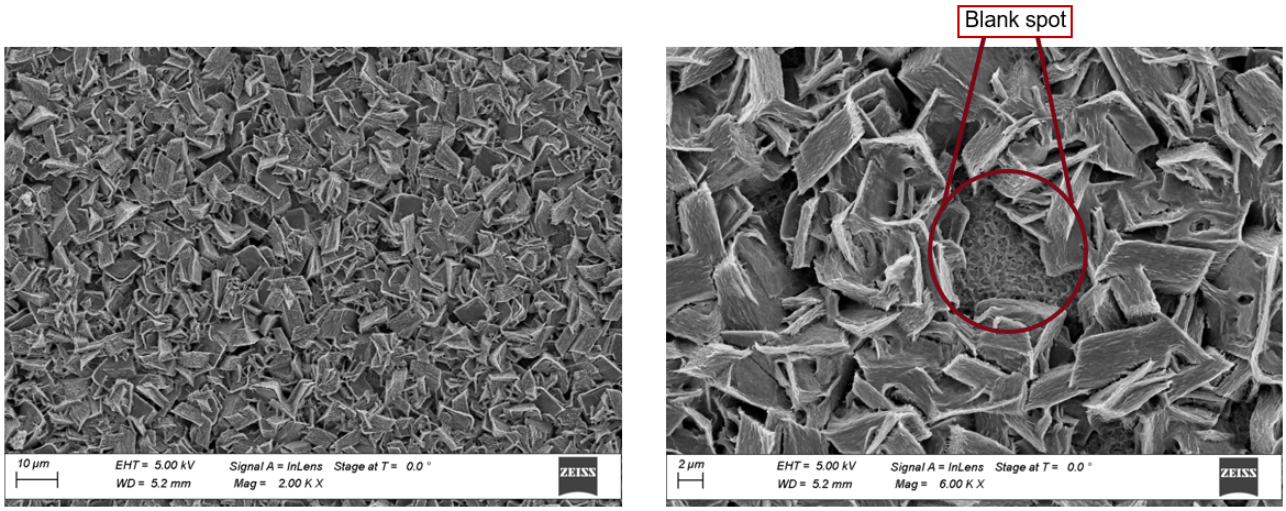

Figure 4.8: SEM Zeiss images of MOF-coated Cu$_2$O photo-cathode under different magnifications revealing blank spots in the coating.

To further confirm the composition of the Cu-BDCNH$_2$ crystals, energy-dispersive X-ray spectra (EDS) was deployed. The analysis shows that the areas covered with MOF display high intensities for C, O, Cu, and N elements, the latter being an indicator for the presence of Cu-BDCNH$_2$ crystals. Since the EDS analysis might not be the most precise technique to measure N, additional FTIR analyses were conducted.

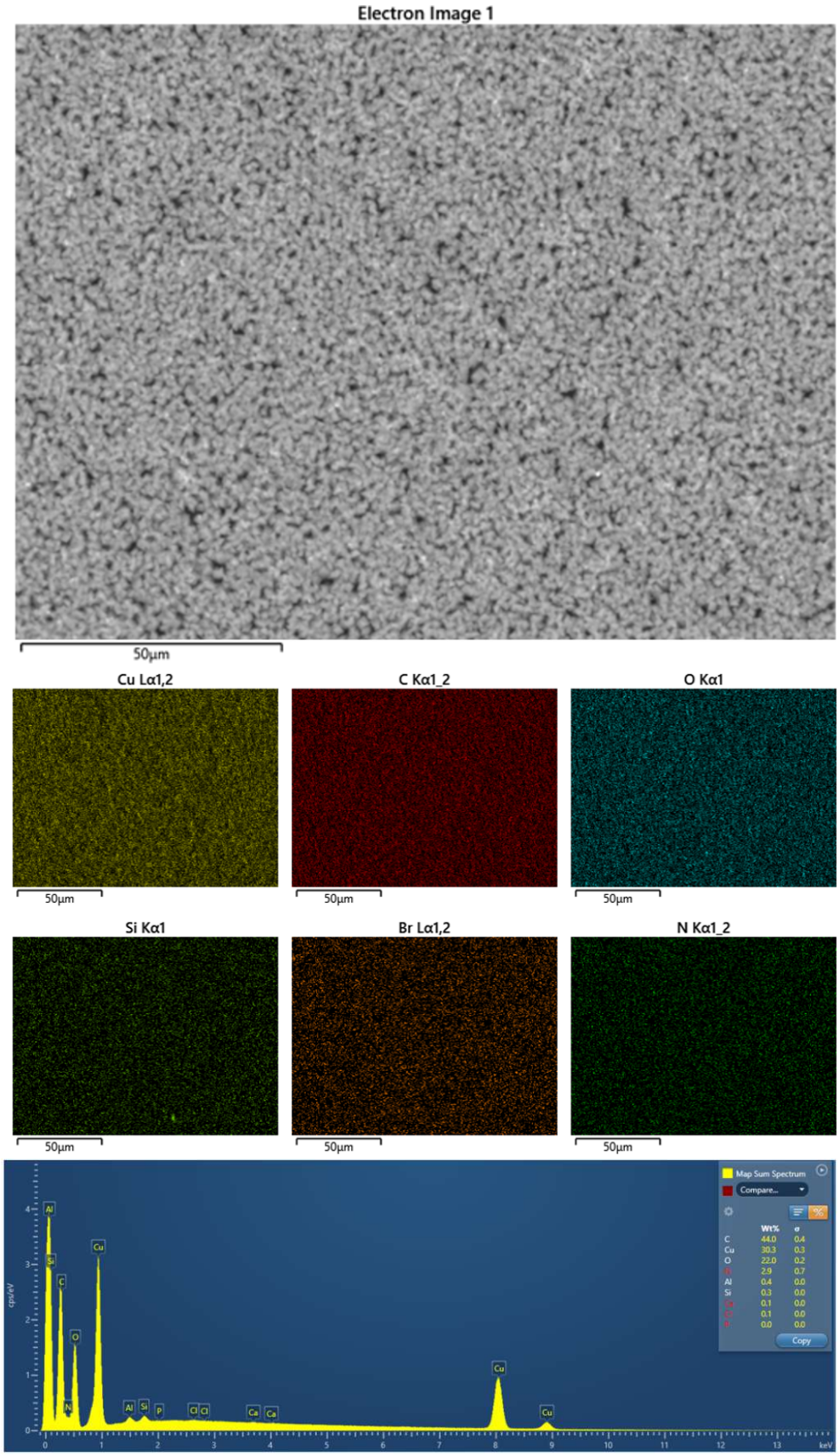

Figure 4.9: EDS spectra of Cu-BDCNH$_2$ on Cu_2O on gold.

The FTIR-ATR infrared analysis was conducted to confirm the successful construction of Cu-BDCNH$_2$ MOF on the surface of the Cu_2O film in the range of 4000 to 600 cm^{-1}. As can be seen in Figure 4.10, the two peaks in the range of 3358 to 3507 cm^{-1} belong to the

stretching vibrations of amine groups. Furthermore, the bands of the organic ligands as follows: vibrational modes COO^- (asymmetric) at 1593 cm^{-1}, COO^- (symmetric) at 1373 cm^{-1}, and C-O-Cu at 1124 cm^{-1}, which is in accordance with the literature [52]. In addition, the C-H stretching vibrations can be observed in the range of 2969–2822 cm^{-1}. These findings are a good indication of the successful coordination of Cu^{2+} and –COOH of 2-NH_2-BDC. Compared to this, a typical FTIR spectrum of Cu_2O reveals a broad band for Cu_2O between 3000 to 2500 cm^{-1}, and a sharp peak at 2355 cm^{-1} to CO stretching. In addition, the characteristic peak of Cu_2O at 608 cm^{-1} can be confirmed [77].

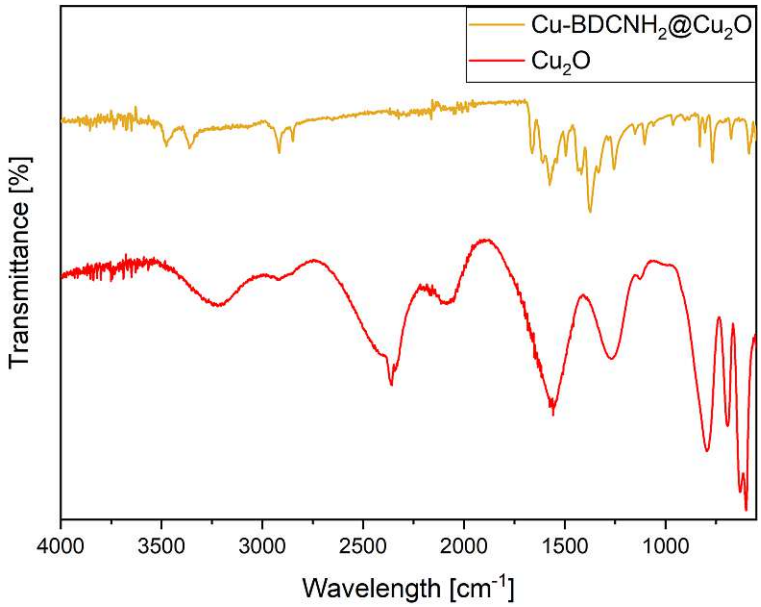

Figure 4.10: FTIR-ATR spectra of Cu_2O and Cu-$BDCNH_2$ on Au.

Furthermore, to explore the structural integrity and crystallinity of the MOF crystals, X-ray diffraction (XRD) analyses were carried out. The characteristic peaks for Cu-$BDCNH_2$ observed at $2\theta = 10.4°$, 11.9°, 13.2°, 16.9°, 18.1°, 20.9°, and 24.5° indicate the crystalline nature of the Cu-$BDCNH_2$ film (see Figure 4.11) and correspond to the reflection planes of (110), (001), $(11\bar{1})$, $(\bar{2}01)$, (111), (220), and (131), respectively [67]. The obtained XRD spectra are in good agreement with literature [52, 67].

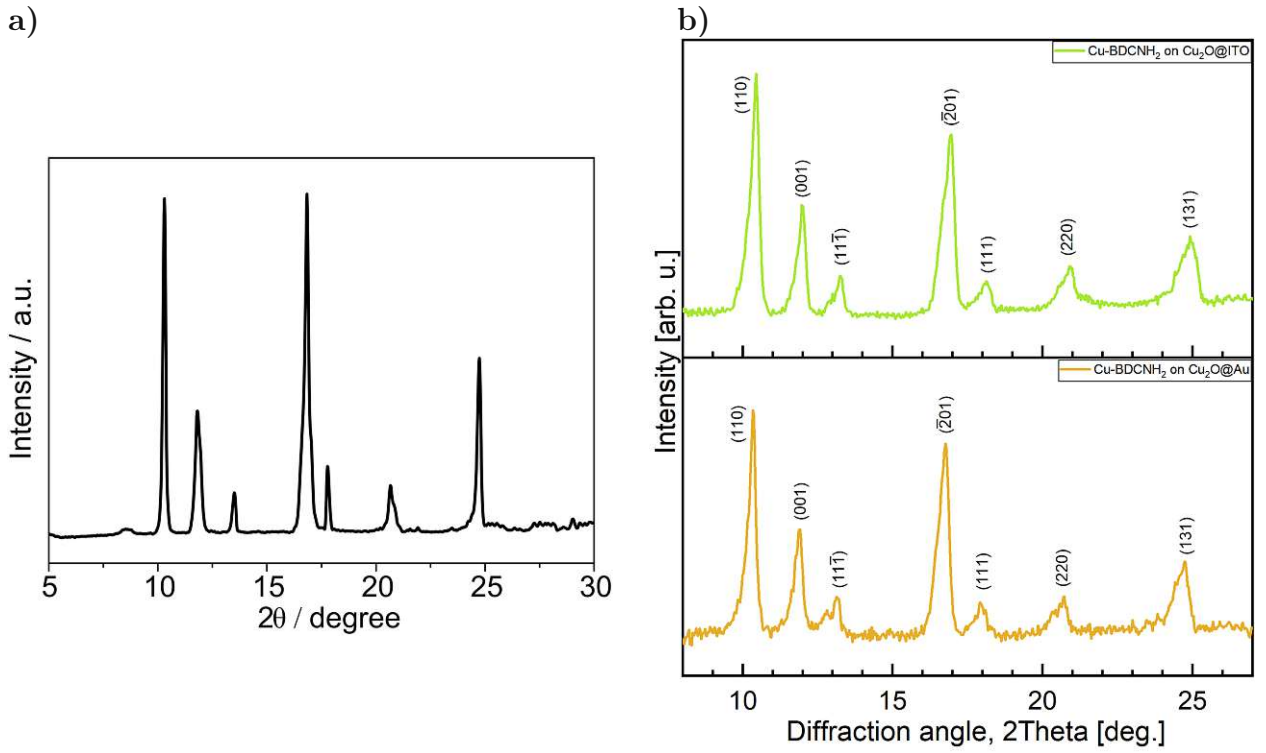

Figure 4.11: XRD pattern of Cu-BDCNH$_2$ as reported in the literature [52] the experimental data.

Comparing the XRD patterns before and after the MOF synthesis, as illustrated in Figure 4.12, the (111) peak becomes more prominent, particularly for Cu_2O deposited on Au. As aforementioned, the in-situ synthesis of Cu-BDCNH$_2$ requires the release of Cu^+ from the substrate, which is oxidized to Cu^{2+} and later coordinated to form the MOF crystal [74]. Furthermore, in literature, the (111) phase of Cu_2O is described as the most stable [38]. This gives rise to the assumption that copper ions from less stable phases dissolve first into the electrolyte and are consequently consumed for the MOF synthesis, which reflects in the XRD pattern, and the (111) peak for Cu_2O on Au intensifies. Figure 4.13 illustrates a proposed mechanism for the formation of the MOF on Cu2O.

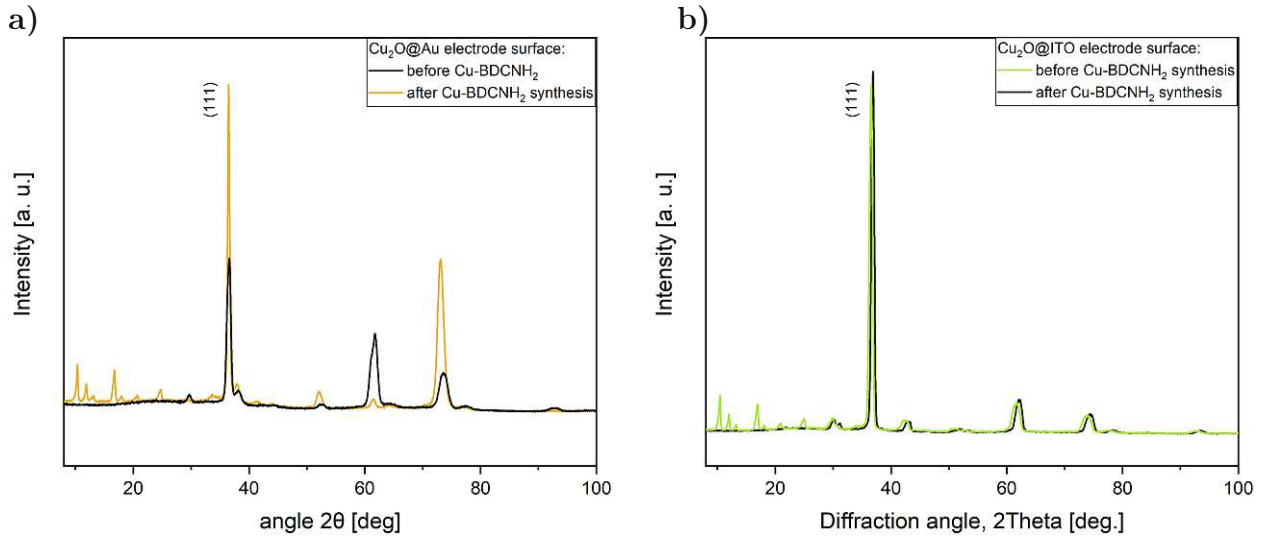

Figure 4.12: XRD pattern of Cu-BDCNH$_2$ before and after the synthesis on a) Au and b) ITO.

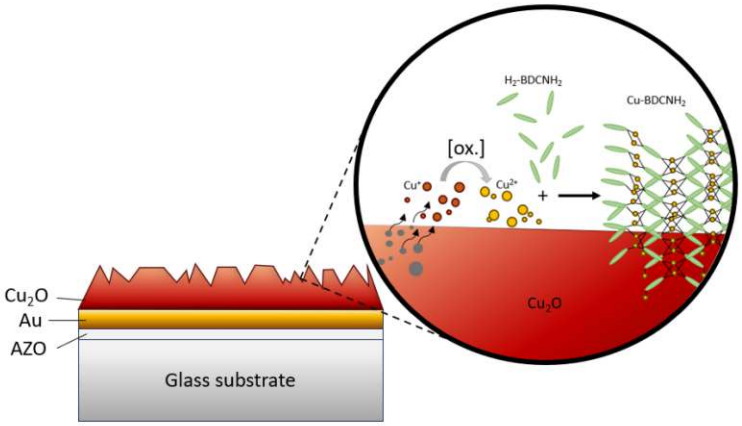

Figure 4.13: Schematic illustration of the MOF formation on Cu_2O, with first Cu^+ being dissolved from the oxide layer, followed by its oxidation to Cu^{+2} and coordination with the ligand to Cu-$BDCNH_2$.

Post-synthetic modification

SEM was performed to investigate the surface of Cu-$BDCNH_2$ before and after the post-synthetic modification with pentadecafluorooctanyol chloride. As can be seen in Figure 4.14, the surface appears rougher compared to the non-functionalized MOF surface.

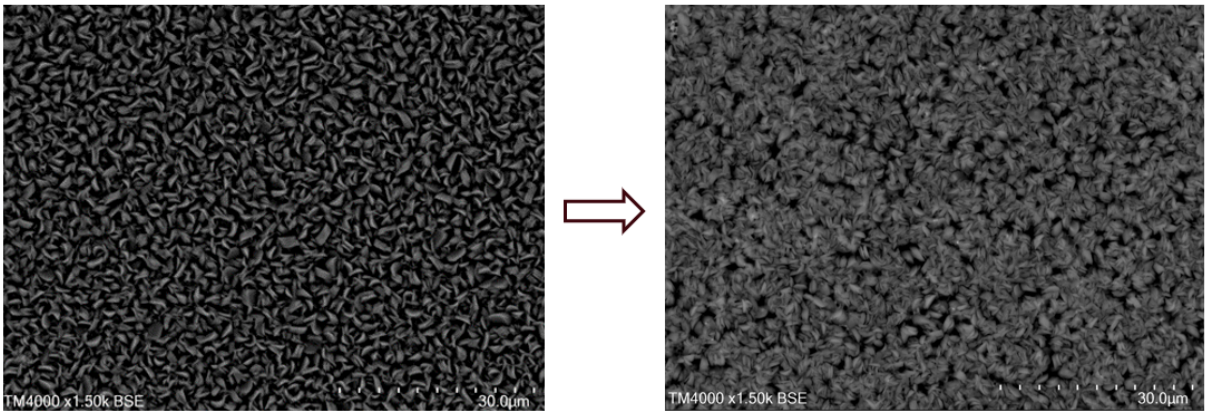

Figure 4.14: SEM images of Cu-$BDCNH_2$ on Cu_2O before and after the functionalization.

The moment TEA was added to the mixture of pentadecafluorooctanyol chloride and THF, a milky yellowish precipitate formed. The sample's appearance in itself did not change tremendously compared to the MOF-coated sample but took on a slightly more greenish color compared to before the modification procedure, as illustrated in Figure 4.16. The XRD analysis does not show any significant differences between the unmodified and modified Cu-MOF.

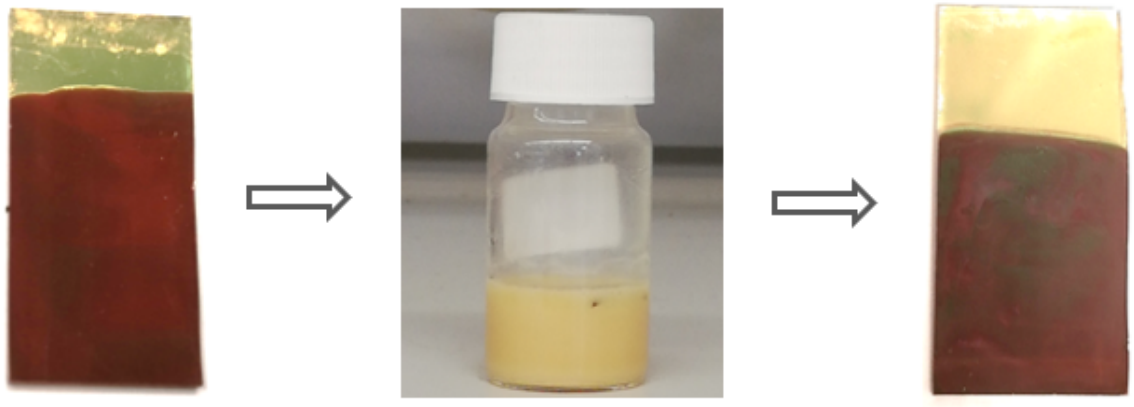

Figure 4.15: Cu-BDCNH$_2$ on Cu$_2$O@Au photo-cathode before and after the functionalization.

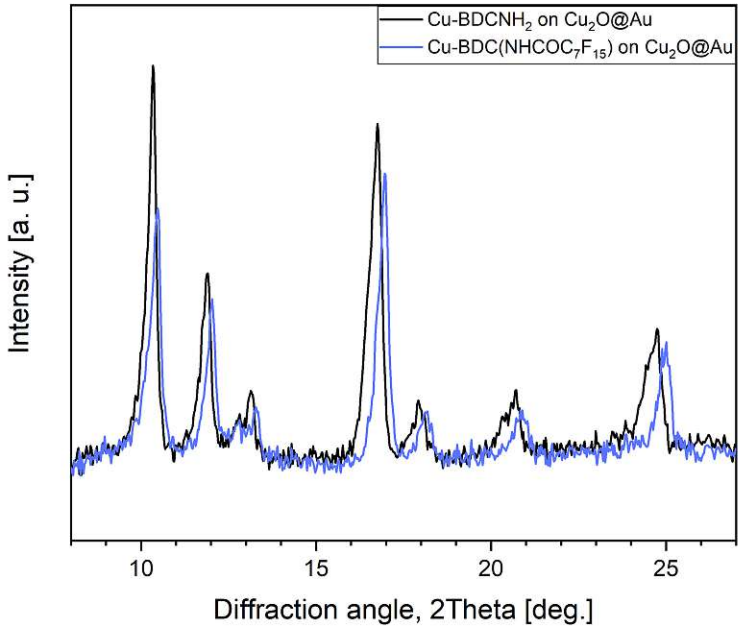

Figure 4.16: XRD pattern Cu-BDCNH$_2$ before and after the functionalization.

To further analyze the composition of the newly obtained Cu-BDC(NHCOC$_7$F$_{15}$) MOF, EDS characterization was applied (see Figure 4.17). The EDS analysis revealed the composition of Cu, O, C, N, and F elements on the Cu$_2$O substrate. The sudden appearance of F confirms the successful functionalization of Cu-BDCNH$_2$ via PSM.

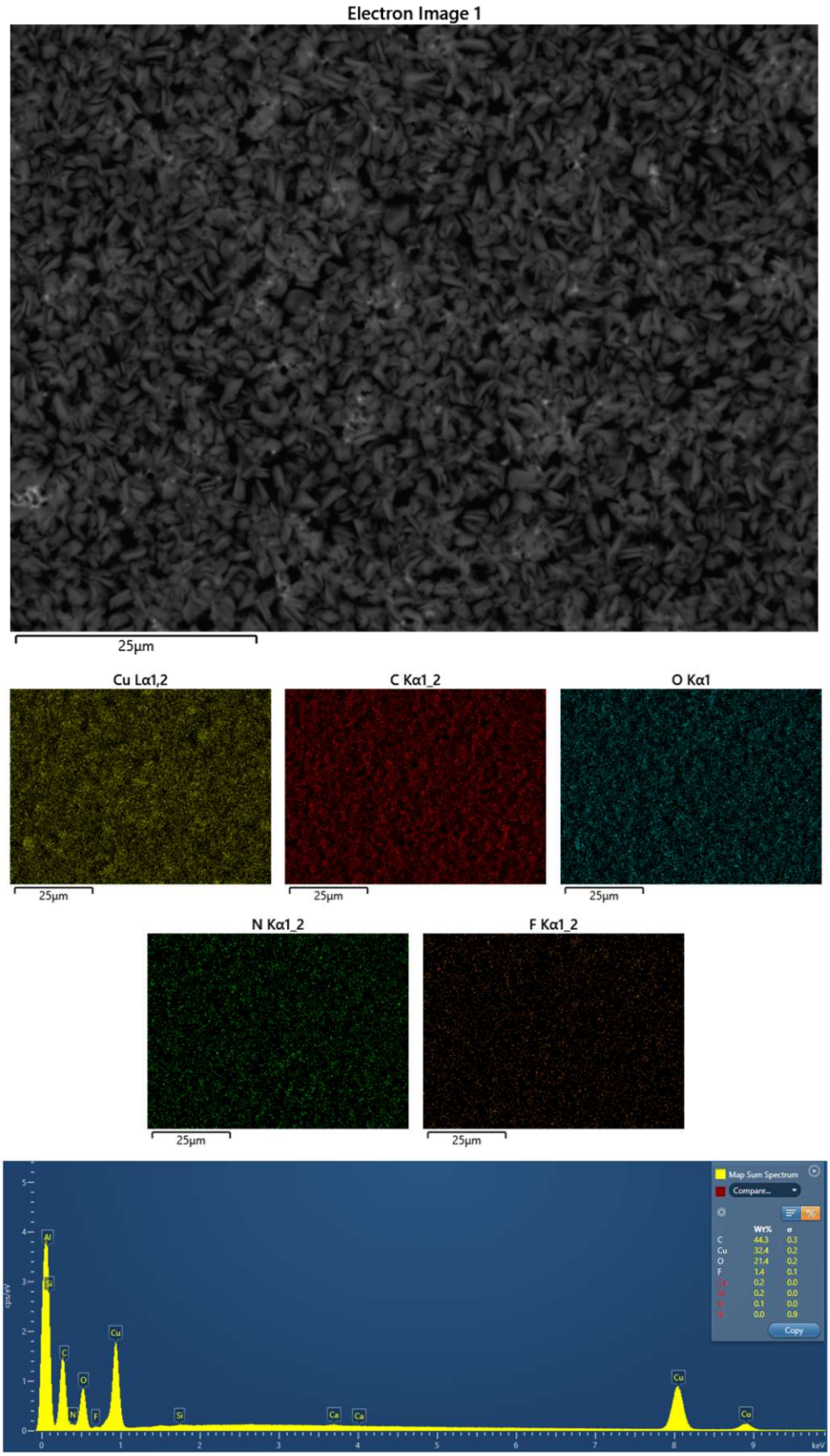

Figure 4.17: EDS spectra of Cu-BDC($NHCOC_7F_{15}$) on Cu_2O on gold.

The XPS analysis clearly shows that the functionalization with pentadecafluorooctanyol chloride was successfully implemented with the presence of the F_{1s} at 686 eV. The visibility of the F KLL Auger peak with binding energy at 832 eV and 858 eV further acts as a confirmatory signal. Furthermore, the fitted spectrum of C_{1s} also displays a peak at 291.8 eV and 294.5 eV characteristic for CF2 and CF3 bonding, respectively.

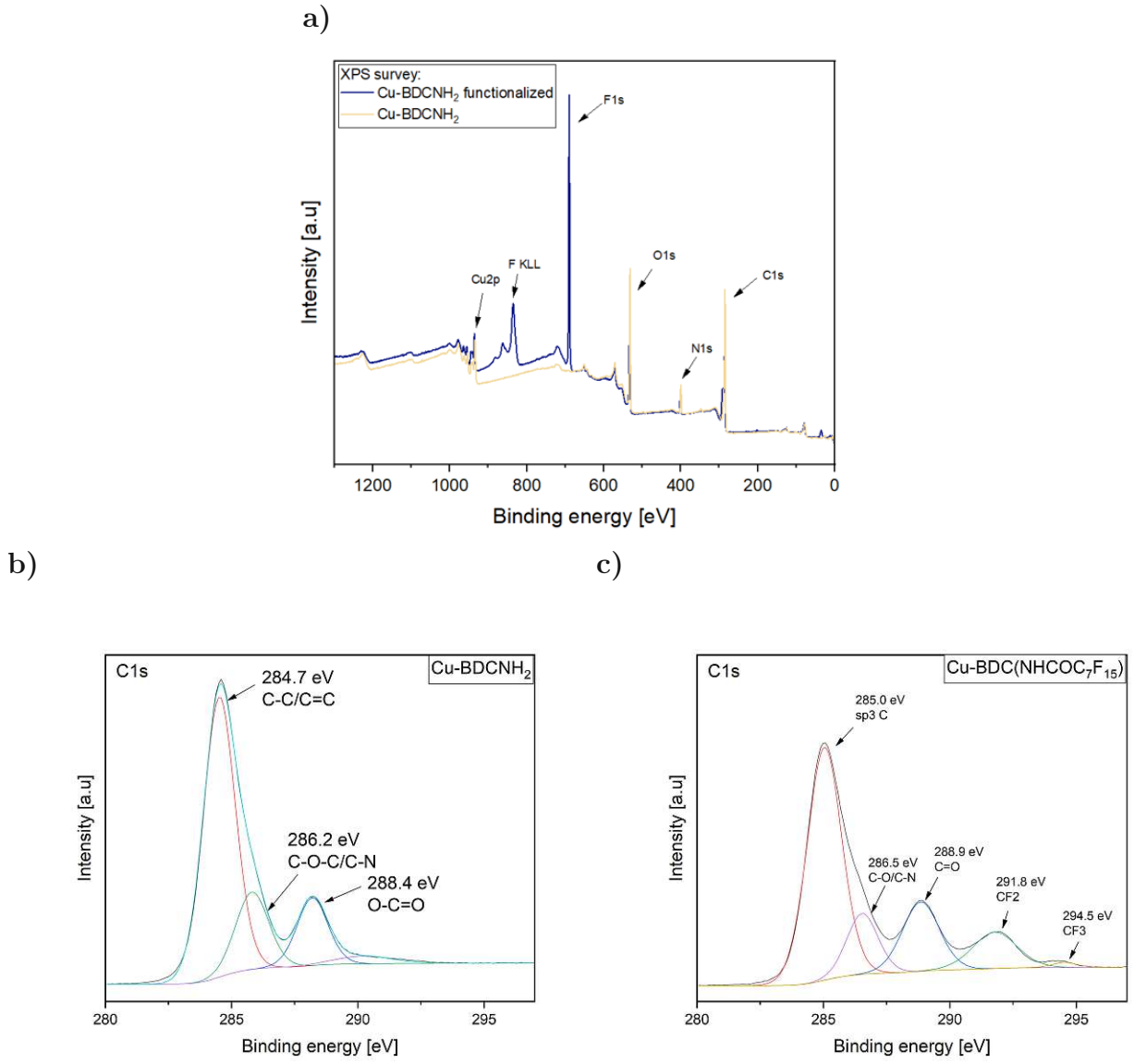

Figure 4.18: XPS spectra of Cu-BDCNH$_2$ and Cu-BDC(NHCOC$_7$F$_{15}$). a) XPS survey, b) XPS C1 spectra of Cu-BDC(NHCOC$_7$F$_{15}$), and c) Cu-BDC(NH$_2$).

The optical properties of Cu_2O, Cu-BDCNH$_2$, and Cu-BDC(NHCOC$_7$F$_{15}$) were analyzed by FTIR spectral reflectance analysis (see Figure 4.19. In general, all samples displayed absorption in the UV–Vis NIR region. The absorption band at 600–860 nm is caused by the d-d transitions around the center Cu clusters as reported in literature [51]. The band gap was estimated by extrapolation of the baseline (dashed line). The interception of extrapolated slope (solid line) and the baseline indicates the band gap. Although this method is not the most precise, it is suitable to make sufficient estimations of the BG.

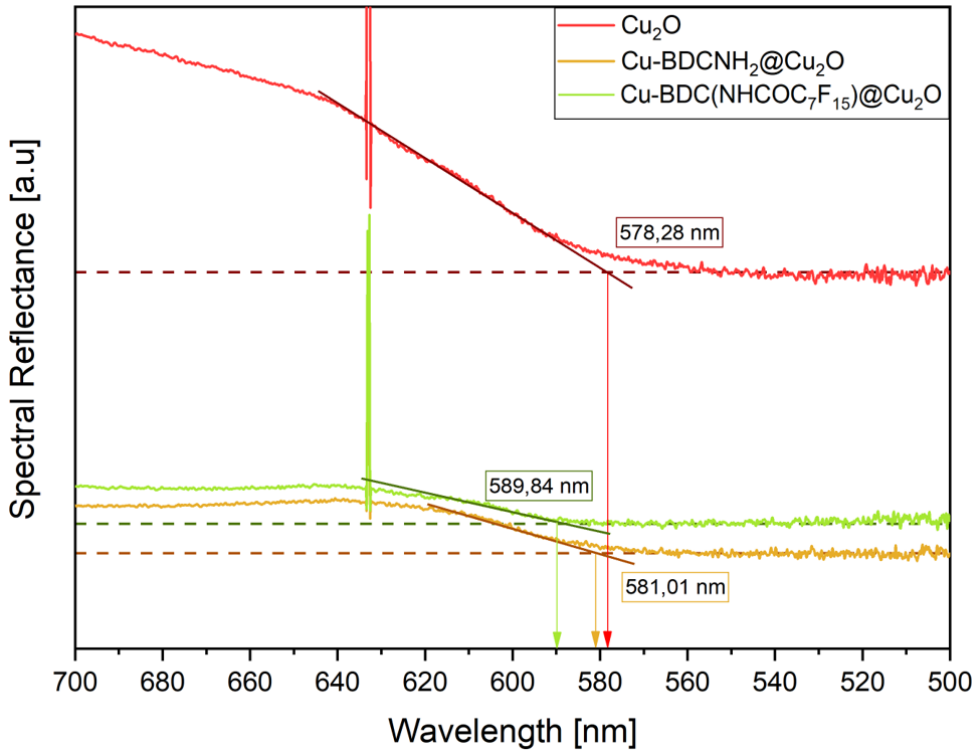

Figure 4.19: Band gap measurement of Cu_2O, Cu-$BDCNH_2$, and Cu-$BDC(NHCOC_7F_{15})$ on Au.

The values of band gap of Cu_2O, Cu-$BDCNH_2$ and Cu-$BDC(NHCOC_7F_{15})$ are 2.14, 2.13, and 2.10 eV, respectively. The corresponding BGs of the different electrode surfaces are summarized in Table 4.1. While Cu_2O exhibits the largest BG of 2.14, which is in the expected range of 2.0 - 2.5 eV reported in literature, the BG slightly decreases depending on the MOF.

Table 4.1: Summary of the different materials together with their corresponding Energy bandgap obtained via FTIR.

Material	***wavelength [nm]***	***Energy [eV]***
Cu_2O	578.28	2.14
$Cu\text{-}BDCNH_2$	581.01	2.13
$Cu\text{-}BDC(NHCOC_7F_{15})$	589.84	2.10

4.1.3 Addition of hydrophobic protection layer

The PDMS layer was added via spin-coating, as described earlier. The SEM images display the change in the surface of Cu_2O on Au and ITO when coated with 0.1, 1, and 10 wt% PDMS. While no difference from the blank Cu_2O surface is noticeable for 0.1 wt% PDSM, a clear coating is observable for 10wt% PDMS.

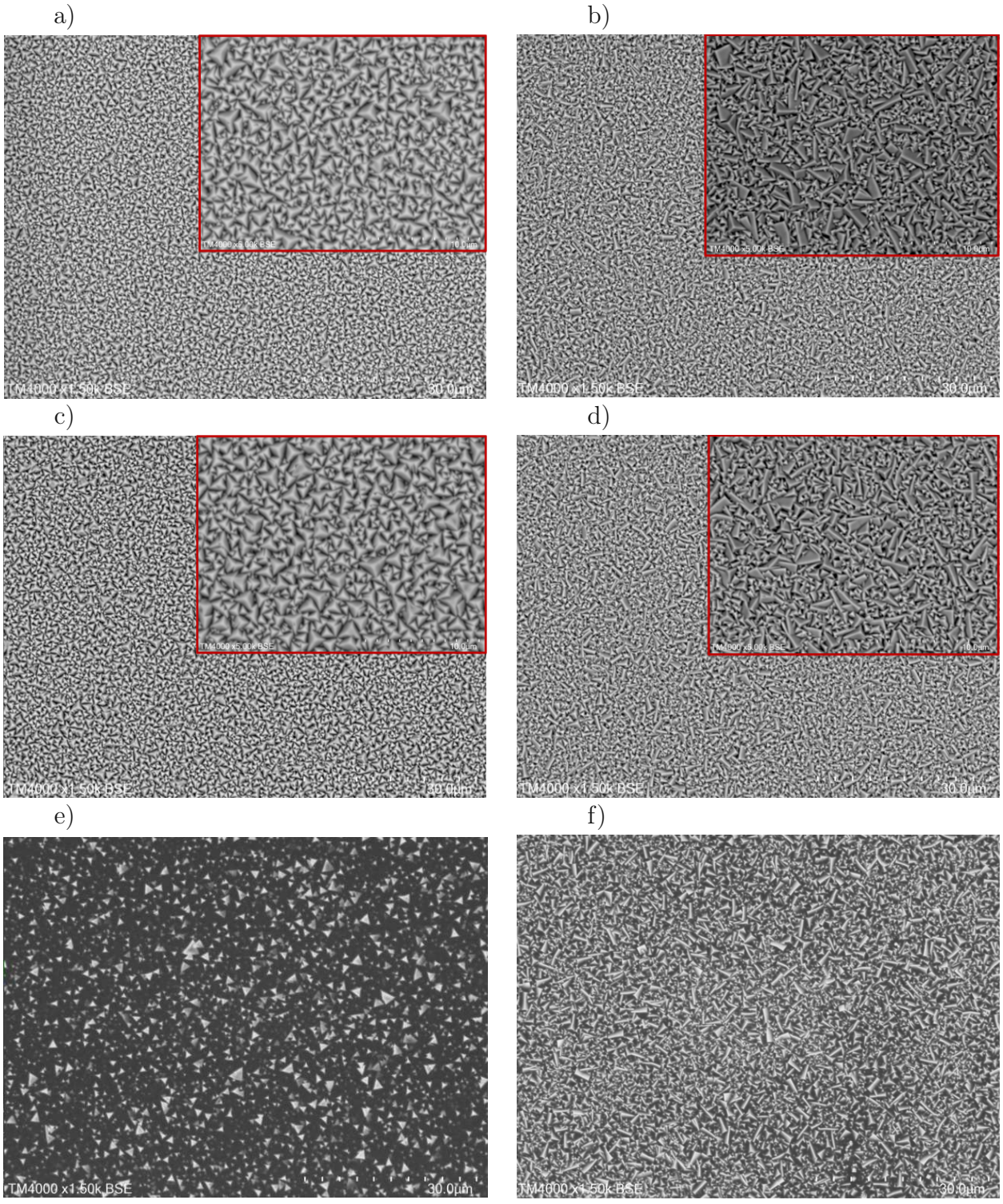

Figure 4.20: SEM images for Cu_2O spin-coated with 0.1wt%, 1wt%, and 10wt% PDMS. The row a-c-e) represent the coating on Au, while the row b-d-f) is the coating on Cu_2O deposited on ITO.

Furthermore, before adding the PDMS solution, the substrates were washed with DI water and ethanol and dried for 5 min at 100°C. 100 μl was dropped onto the substrates and spin-coated at 5000 rpm/s (2500 rpm/s) for 1 min, including 100 rpm/s (50 rpm/s) for 10 s as spreading step beforehand – 5 times in total. After spin-coating, the samples were cured at 100°C for 1 h after each coating step.
By conducting contact angle measurements (CA), the hydrophobic properties of the different layers were investigated. Here, a drop of 5 μl milli-q water was carefully placed on the surface of the electrode, and the contact angle was measured. The results are displayed in Figure 4.21. Cu_2O in the middle of the substrate displays a slightly different morphology compared to the edge, which is known as a common problem for processes involving electrochemical deposition. This probably causes a high standard deviation as the roughness/structure of the surface is not entirely homogeneous. After the functionalization, the contact angle increased from around 71° to 137°, which indicates that the PSM of the Cu-MOF was successful.

Table 4.2: Measured contact angle of different PEC cells.

Substrate Architecture	*Contact angle [°]*
Pure Cu_2O@Au	112.50 ± 1.46
Pure Cu_2O@ ITO	96.28 ± 2.1
Cu_2O@Au coated + 10 wt% PDMS	111.59 ± 3.50
Cu_2O@ITO coated + 10 wt% PDMS	113.3 ± 0.76
Cu_2O@Au + Cu-BDCNH$_2$ MOF	70.71 ± 2.10
Cu_2O@Au + functionalized Cu-BDCNH$_2$ MOF (PSM)	136.78 ± 2.18

a) b)

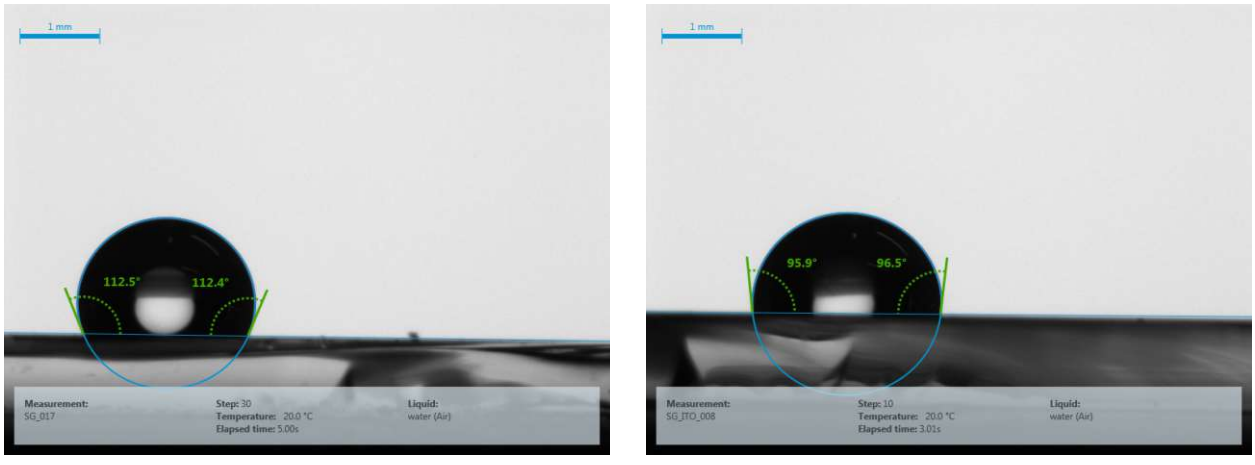

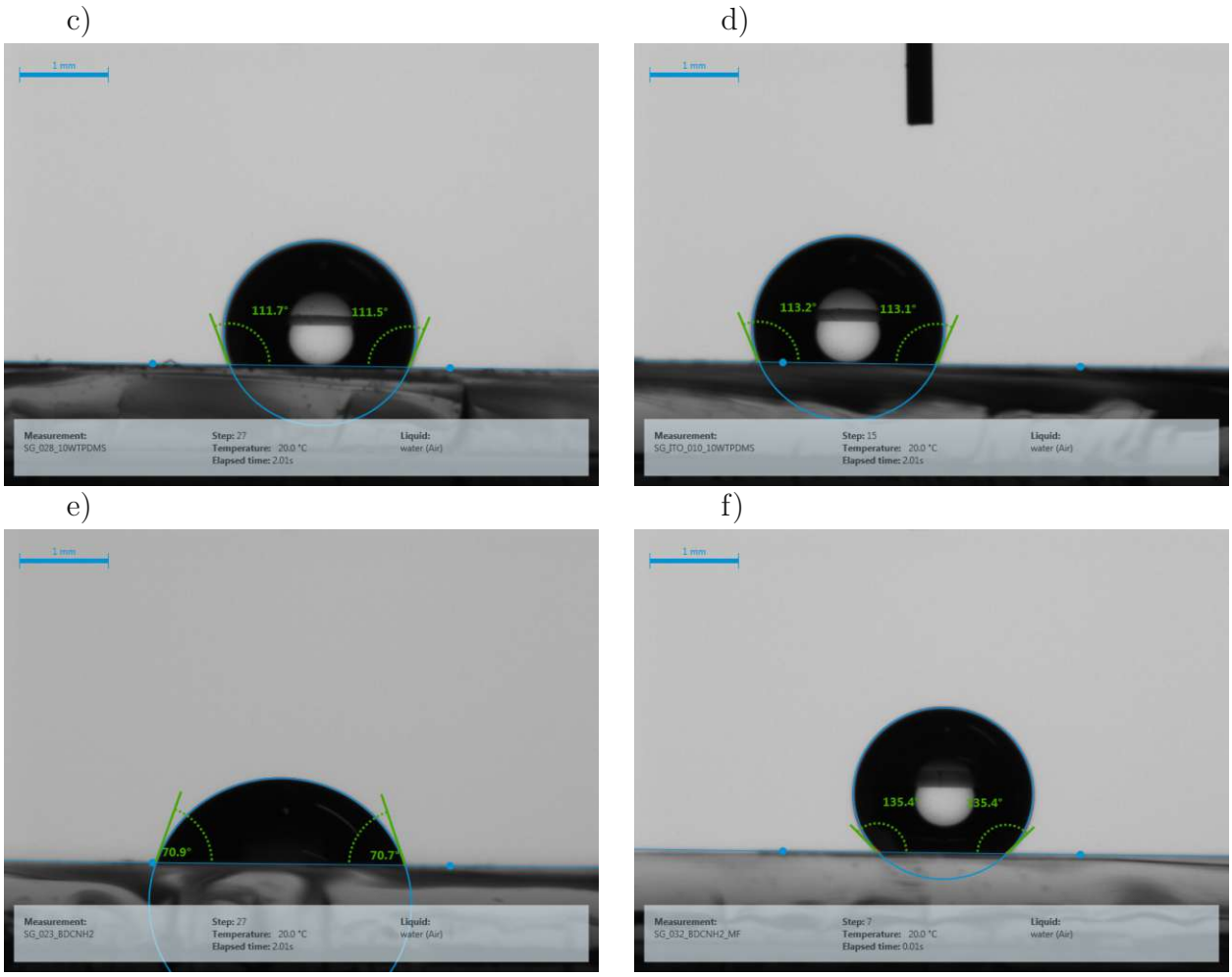

Figure 4.21: Contact angle images of milli-q water on a) pure Cu_2O@Au, b) pure Cu_2O@ITO, c) Cu_2O@Au coated + 10 wt% PDMS, d) Cu_2O@ITO coated + 10 wt% PDMS, e) Cu_2O@Au + Cu-BDCNH$_2$ MOF, and f) Cu_2O@Au + functionalized Cu-BDCNH$_2$ MOF (PSM), as displayed in Table 4.2.

4.2 Electrochemical analysis

4.2.1 Linear-sweep voltammetry

Bare Cu_2O photo-cathode and semiconducting oxide overlayers

Photo-electrochemical tests were conducted by making use of a three-electrode system in 0.1 M Na_2SO_4 electrolyte (pH 7) as described in the previous section. As the PEC HER is a pH-sensitive reaction, the tests were conducted in pH 5 and 7 pH to investigate the difference. The one-set potential is commonly refereeing to as the potential where the current starts to deviate from "zero" and should be as close as possible to 0 V vs RHE.

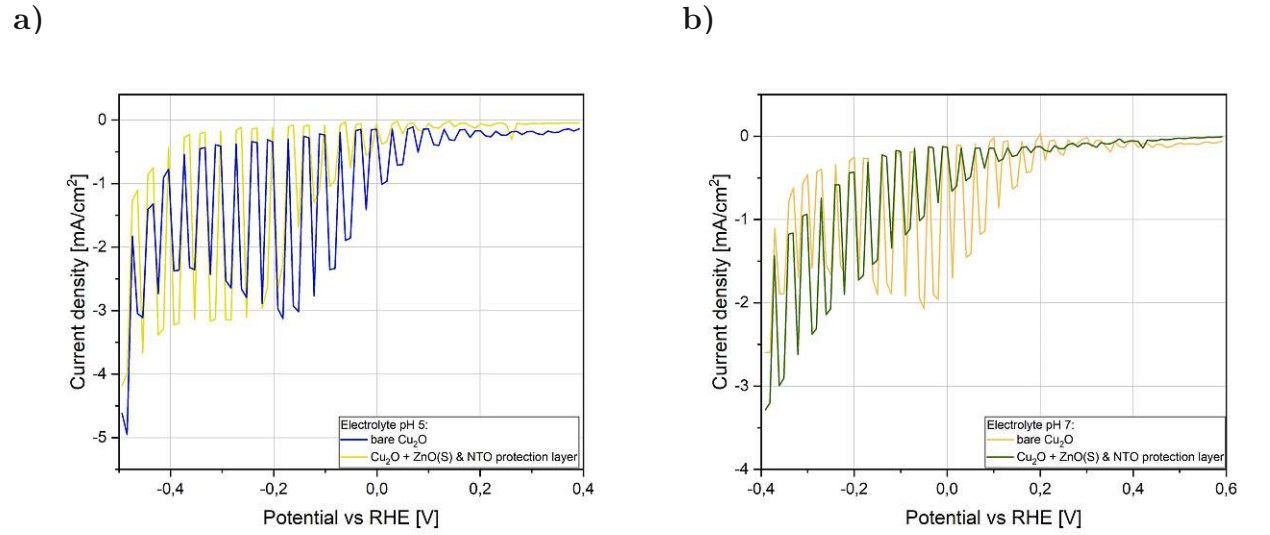

Figure 4.22: Current density obtained via LSV for a) pH 5 and b) pH 7 electrolyte.

Comparing the results for the PEC test conducted in ph 5 and 7, it becomes obvious that the current density for bare Cu_2O is higher when it is coated with the semiconducting overlayers. The obtained current densities are summarized in Table 4.3.

Table 4.3: Comparison of the current-density obtained at different pHs of the electrolyte.

	Electrolyte	
	pH 5	***pH 7***
bare Cu_2O	1.54 mA/cm^2	1.96 mA/cm^2
semiconducting overlayers	0.5 mA/cm^2	0.8 mA/cm^2

It is worth to note, that 0 V vs RHE was selected to determine the photo-current density as at this specific potential, the HER is triggered, which is also visible in the LSV - this is the case for all measurements. The additional current obtained for the bare Cu_2O might be due to photo-corrosion, which might explain the decreasing photo-current after -0.2 V vs RHE. Furthermore, the reaction curve is shifted to the left at pH 7. Due to the higher current obtained for pH 7 as well as the more neutral conditions met at this pH, pH 7 electrolyte was selected for all following experiments. The on-set potential is similar in both cases. As the reaction is processed, the dark current (the current measured as the light source is switched off) slightly increases for both cases. As the HER reaction is only triggered under light illumination, according to literature, the measured dark current should be ideally as close to zero as

possible in order to ensure that the obtained photo-current density is purely due to the HER and not due to side reactions or degradation processes.

After the PEC test, a noticeable color change occurred: as visible in Figure 4.23 the previously reddish color of Cu_2O, which was exposed to the light source, turns blackish, whereas the rest that was covered by the mask remained unchanged. This blackening effect was observed for all samples. As both the bare Cu_2O and the Cu_2O surface that was protected by the semiconductor overlayers underwent a color change, it is safe to assume that the reason for this behavior lies with Cu_2O. A possible explanation is the formation of metallic copper due to the self-reduction of Cu_2O, leading to a reaction similar to an etching process (as illustrated in Figure 4.23), rendering the previously smooth Cu_2O surface extremely porous. The obtained current flow is a combination of degradation processes as well as due to the HER at the cathode/electrolyte interface. In order to distinguish between the two processes, the total amount of H_2 produced needs to be measured e.g., via gas-chromatography, which was not possible to properly conduct in the framework of this work.

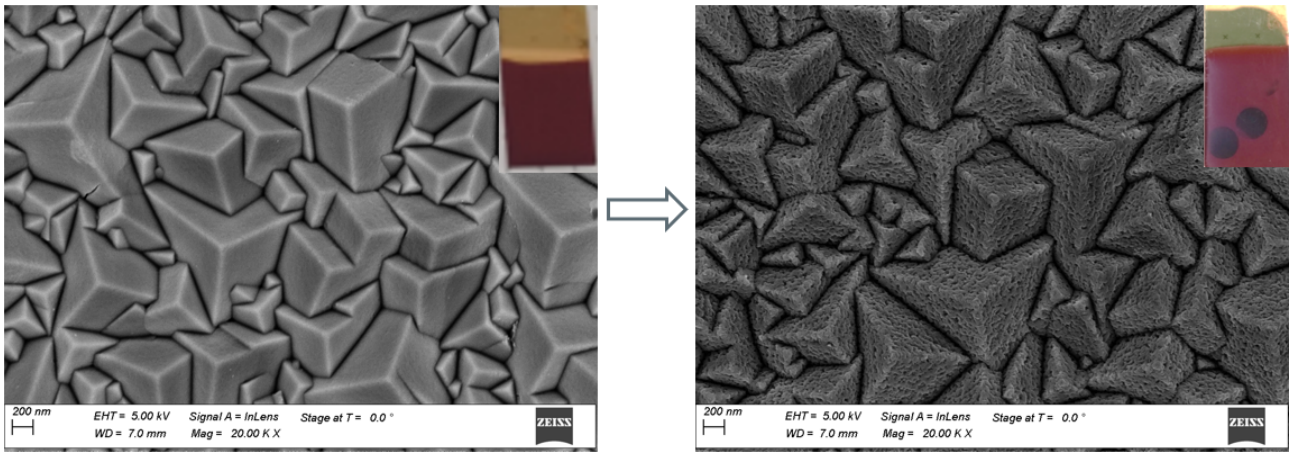

Figure 4.23: SEM images of bare Cu_2O surface without protective coatings before and after the PEC test alongside their corresponding PEC cell in the corner.

Cu-BDCNH$_2$ overlayers and functionalization

The PEC test for the Cu-BDCNH$_2$ coated Cu_2O substrates reveals a shift of the on-set potential towards a more positive value, as visible in Figure 4.24. The on-set potential for the purely oxide-based photo-cathode is generally positioned around +0.4 V, whereas the on-set potential for Cu-BDCNH$_2$ is located around +0.75 V. When the light source is switched on, the recorded current density for the MOF-coated sample gets pushed towards -2.8 mA/cm^2 at 0 V vs RHE, and to -0.8 mA/cm^2 at 0 V vs RHE for the oxide-based photo-cathode. Furthermore, the dark current (the current obtained when the light source is switched off) is relatively small for NTO/ZnO(S)/Cu_2O@Au (around -0.1 mA/cm^2 at 0 V vs RHE), a dark current of around -1.3 mA/cm^2 is recorded for Cu-BDCNH$_2$/Cu_2O@Au. If one only considers the total change in current density when the light source is switched off and on, the Cu-BDCNH$_2$/Cu_2O@Au still achieves a current-density of 1.5 mA/cm^2, whereas the current density of the other sample decreases to 0.7 mA/cm^2. The large dark current for the MOF-coated sample could be due to enhanced light-absorbing abilities generating current solely with room light. The general downward drift for both samples after 0V vs RHE, is most likely due to the destruction of the light-exposed sample area.

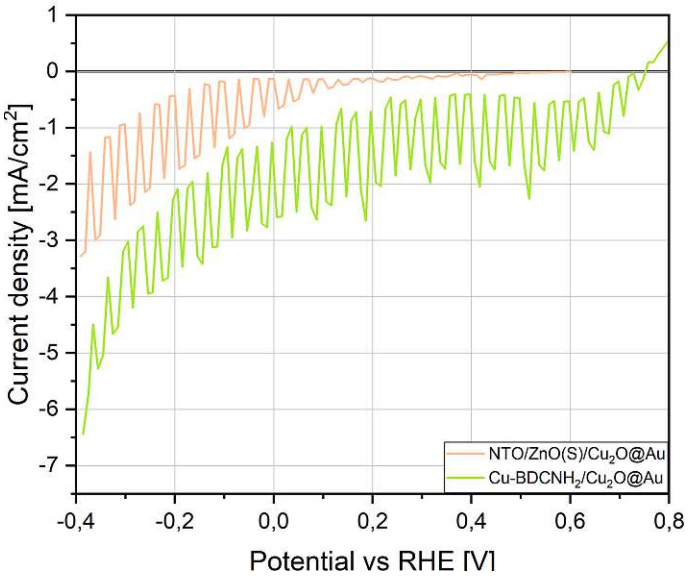

Figure 4.24: Comparison of the obtained current density via LSV for semiconductor overlayers and MOF overlayer on Cu_2O on Au.

Examining the MOF-coated electrode surface under SEM (see Figure 4.25) reveals that the surface part, which was exposed to the light source, has been cleared of the MOFs. Thus, the additional current might be due to interfacial issues, as aforementioned. This again highlights the need for a suitable protection method.

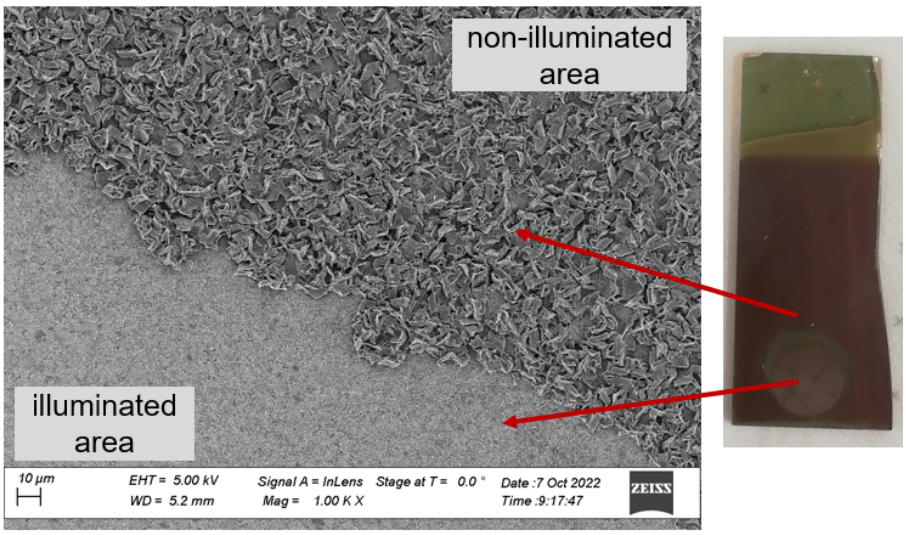

Figure 4.25: MOF-coated Cu_2O surface exhibiting the damaged MOF layer after light illumination.

Figure 4.26 displays the measured current densities for the MOF-coated samples prepared on either gold or ITO alongside a functionalized sample of similar nature obtained via PSM.

The dark current lies for most samples, but Cu-$BDCNH_2$/Cu_2O@ITO, in the range of -0.8 to -0.9 mA/cm^2, with the latter displaying a dark current density of -1.2 mA/cm^2. Interestingly, while both Cu-$BDCNH_2$-coated samples display a photo-current density of -1.9 mA/cm^2, the functionalized Cu-BDC($NHCOC_7F_{15}$) samples display a current density above 2 mA/cm^2, with Cu-BDC($NHCOC_7F_{15}$)/Cu_2O@Au achieving 2.3 mA/cm^2 and Cu-

BDC($NHCOC_7F_{15}$)/Cu_2O@Au achieving 2.1 mA/cm^2. This leads to a total current density of 1.4 mA/cm^2 and 1.3 mA/cm^2 for Cu-BDC($NHCOC_7F_{15}$)/Cu_2O@Au and Cu-BDC($NHCOC_7F_{15}$)/Cu_2O@I respectively. A general observation of the LSV curve also shows a clear improvement regarding the curve development at more negative potentials: independently of the underlying substrate, the LSV curve is shifted upwards towards the end of the measurement. This commonly indicates enhanced stability.

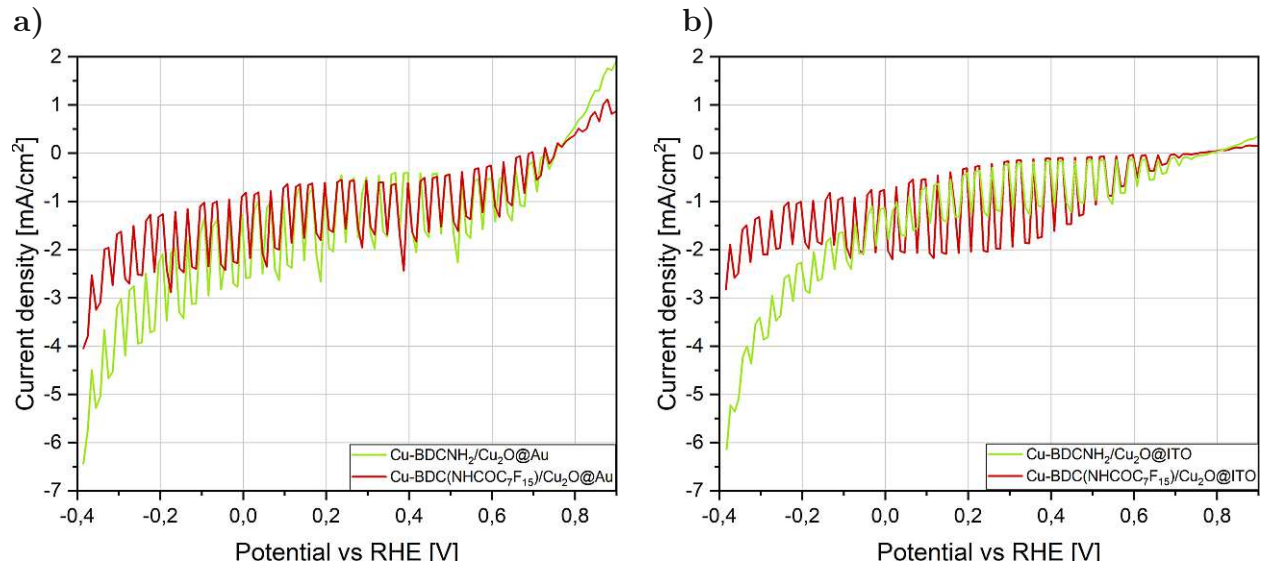

Figure 4.26: Current density obtained via LSV for pre- and post modified MOF layer on a) Cu_2O on Au and b) Cu_2O on ITO.

Polymer-based protection layer

The photo-current densities obtained for different concentrations of PDMS spin-coated onto Cu_2O are displayed in Figure 4.27. Comparing the results at 0 V vs RHE, the Cu_2O@ITO samples all achieve a similar dark current of around -0.05 mA/cm^2 for all PDMS concentrations, whilst the Cu_2O@Au samples only exhibit such a slim dark current for 10 wt%, whereas the 0.1 wt% and 1 wt% both measured a dark current of around 0.3 mA/cm^2. The current density decreases with increasing wt% of PDMS for both substrates.

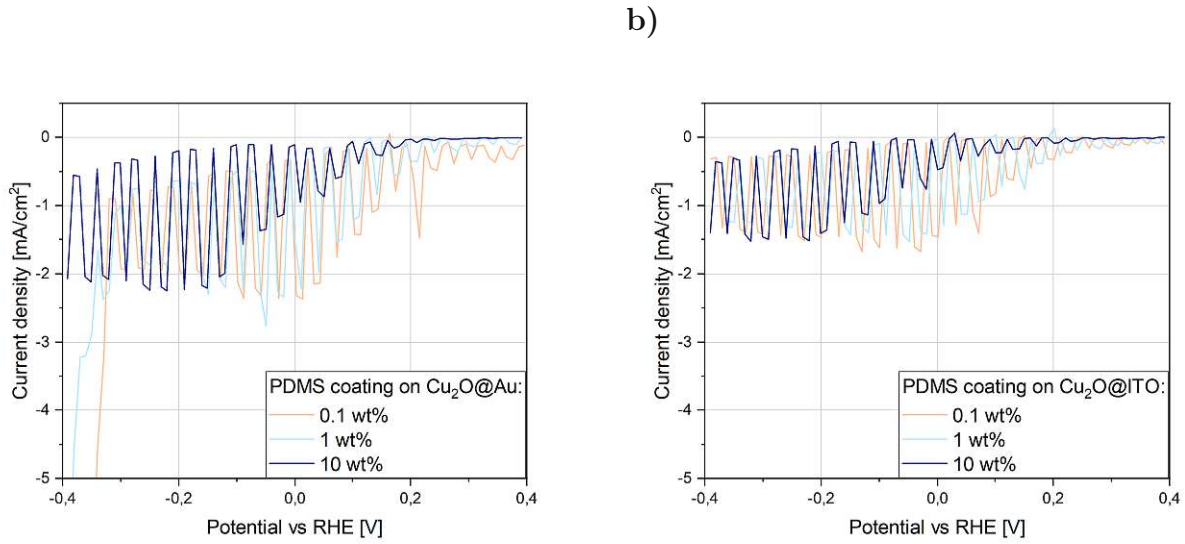

Figure 4.27: Current density obtained for different concentrations of PDMS on a) Cu_2O on Au and b) Cu_2O on ITO.

While the 10 wt% PDMS/Cu_2O@Au and 10 wt% PDMS/Cu_2O@ITO samples achieved 0.9 and 0.5 mA/cm^2, respectively, 0.1 wt% PDMS/Cu_2O@Au and 0.1 wt% PDMS/Cu_2O@ITO samples featured a current density of 2.1 and 1.5 mA/cm^2 (again for Au and ITO) under light illumination. The samples spin-coated with 1 wt% PDMS achieved in both cases an in-between value closer to 0.1 wt% (2.0 mA/cm^2 and 1.4 mA/cm^2 for Au and ITO, respectively). Thus, the general trend regarding the photo-current density is as follows: 0.1 wt%$>$ 1 wt%$>$ 10 wt% for both substrates. The decrease in current density with increasing PDMS concentration is most likely due to blocking effects of the PDMS layer itself. Furthermore, it is to address that the PDMS film suffered considerable damage after the LSV was performed, as displayed in Figure 4.28. Here, it becomes noticeable that the polymer film detaches around the light-exposed spot as well as at the edges of the cell.

Figure 4.28: Damaged 1 wt% PDMS film on Cu_2O after the conducted LSV test.

In order to ensure that a pin-hole free PDMS coating was achieved, multiple coatings of PDMS were applied to the Cu_2O@Au substrate. The LSV curves (see Figure 4.29) illustrate the potential current density achievable for samples coated either once or five times with the corresponding PDMS concentration. The samples coated multiple times displayed an improved dark current of -0.02 mA/cm^2 independently of the PDMS concentration. As expected, the photo-current density for the sample, which has been coated five times with 1 wt% PDMS is smaller (1.9 mA/cm^2) compared to 0.1 wt% x 5 (2.4 mA/cm^2).

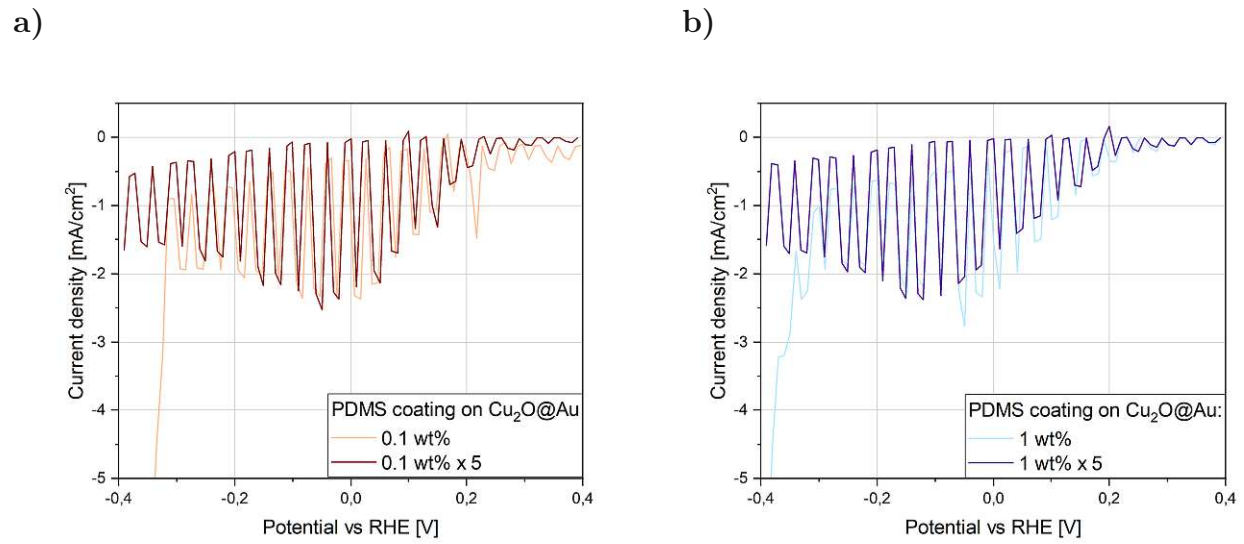

Figure 4.29: Current density obtained via LSV for a) 0.1 wt% PDMS b) 1 wt% PDMS, alongside a sample that has been coated five times with the respective PDMS concentration.

In the pursuit of enhancing the stability of the photo-cathode as well as ensuring the flow of electrons towards the electrode surface, a 50 nm NTO layer was sputtered onto a 0.1 wt% and 1 wt% PDMS/Cu_2O substrate surface, creating p-n junction between the two oxide materials. Figure 4.30 provides a comparison of the purely PDMS-coated samples alongside their NTO sputtered counterparts, as well as a sample that was only sputtered with NTO. In all cases, a decrease in current density with the addition of the NTO protection layer was observed and improved dark current. While the absolute current density is the largest for 0.1 wt%PDMS/Cu_2O@Au (2.1 mA/cm^2), NTO/0.1 wt%PDMS/Cu_2O@Au achieves an absolute current density of 1.2 mA/cm^2. On the other hand, NTO/Cu_2O@Au provides an absolute current density of only -0.7 mA/cm^2. The current density displayed in Figure 4.30 b) are all below 1 mA/cm^2, but for the sample that is only coated with 1 wt% PDMS, indicating that this concentration may be too high for this application.

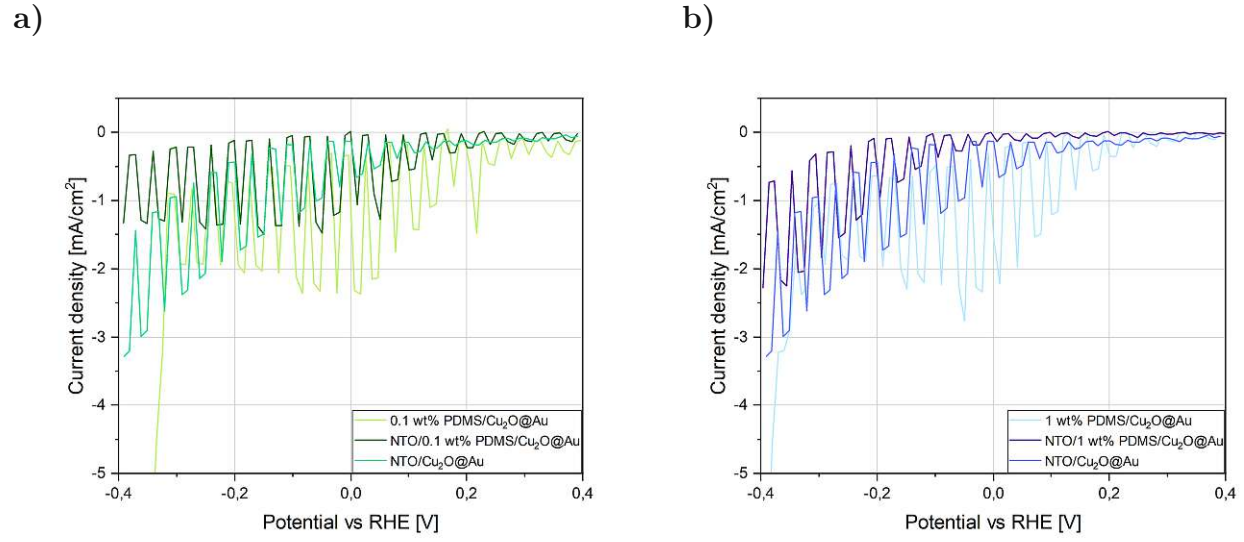

Figure 4.30: Current density obtained via LSV for a) 0.1 wt% PDMS b) 1 wt% PDMS. Both samples were additionally sputtered with NTO to observe the effect of an additional protection layer.

Initially, all three PDMS concentrations (0.1 wt%, 1 wt%, and 10 wt%) were tested via LSV. However, as visible in Figure 4.31, the 10 wt% PDMS sample displayed a drastic change in film transparency after the NTO sputtering process and colored itself silverish. The other two samples remained transparent. The lack of transparency also showed its effects in the LSV (see Figure 4.32), with close to no recorded current density throughout the measurement.

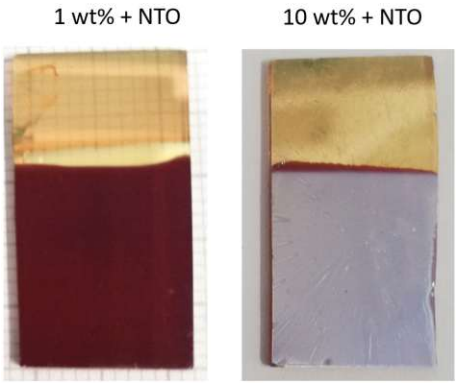

Figure 4.31: NTO sputtered onto 1 wt%, and 10 wt% PDMS-coated Cu_2O@Au substrates.

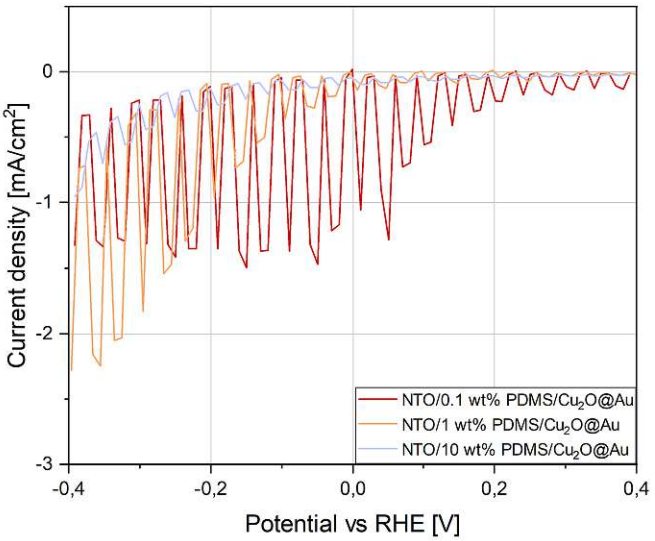

Figure 4.32: Current density obtained via LSV for NTO/PDMS coated Cu_2O on.

4.2.2 Stability measurements of the photo-current density

Bare Cu_2O photo-cathode and semiconducting oxide overlayers

The stability test was conducted in pH 7 similar to the PEC test for different time periods. For the measurement, a chronoamperometry was conducted with a constant voltage of 0V vs RHE. The light source was switched off every 10 s, starting with the light on as marked in Figure 4.33. Soon after the start of the measurement, the current density for both Cu_2O@Au and Cu_2O@ITO decreases tremendously, indicating poor stability. Cu_2O@ITO performs overall worse compared to Cu_2O@Au, which might be due to adhesion problems of Cu_2O on ITO since the Cu_2O film peeled off the glass substrate, as can be seen in Figure 4.34.

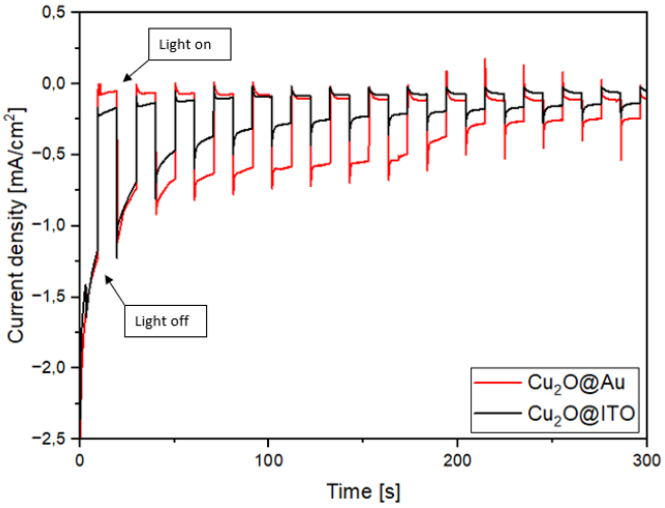

Figure 4.33: Evolution of the current density over 5 min for Cu_2O on Au and ITO.

In order to verify which interface is failing (Cu_2O/ITO or ITO/glass), the multimeter was used to measure the resistance. Since glass can not be detected with the multimeter due to its high resistance, it is safe to assume that the failing interface is between Cu_2O and ITO. Compared to this, the Au-substrates display a resistance of ∼4 Ohm, which might explain the higher current density obtained for Cu_2O@Au.

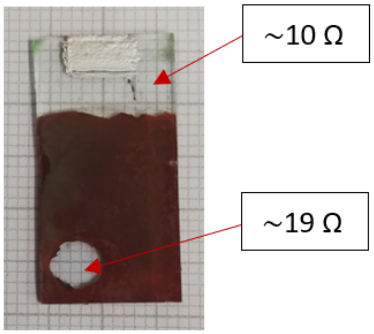

Figure 4.34: Damaged Cu_2O film on ITO substrate alongside their measured resistance.

Figure 4.35 displays the evolution of the current density over 5 min for Cu_2O@Au additionally sputtered with NTO and NTO/ZnO(S). While NTO/ZnO(S)/Cu_2O@Au exhibits a relatively stable current density of -0.5 mA/cm^2, NTO/Cu_2O@Au provides an initially larger current density starting from -2.4 mA/cm^2 slowly decaying to -0.4 mA/cm^2 throughout 300 s.

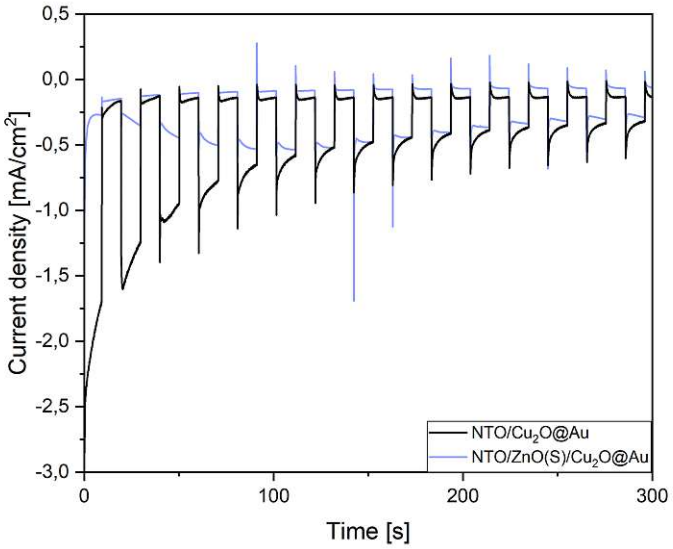

Figure 4.35: Evolution of the current density over 5 min for Cu_2O on Au sputtered with NTO and NTO/ZnO(S).

Cu-BDCNH$_2$ overlayers and functionalization

The evolution of the current density for MOF-coated samples before and after PSM is illustrated in Figure 4.36. In both cases, a large dark current can be observed alongside a decrease in the overall current density after 100 s. The high current density of 3 mA/cm^2 and 1.7 mA/cm^2 recorded in the first seconds diminished quickly to 0.5 mA/cm^2 and 0.4 mA/cm^2 current density, for Cu-BDCNH$_2$ before and after the functionalization, respectively. In order to make further assumptions about the nature of the intense dark current for the MOF-coated samples, stability measurements were conducted under two different conditions: 1) dark measurement and 2) room light measurement. For the former, a box was placed over the experimental set-up as well as all light sources (including room light) were turned off. As for the latter, the AM.15 light source was omitted, and the experiment was conducted solely with the laboratory room light.

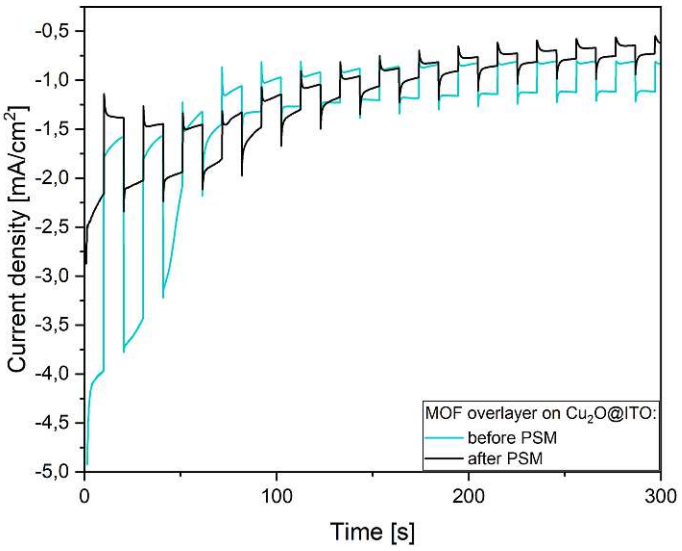

Figure 4.36: Evolution of the post-synthetic modified MOF layer after the stability test under room light.

The results for Cu-BDCNH$_2$ and Cu-BDC(NHCOC$_7$F$_{15}$) (Cu-BDCNH$_2$ after PSM), are presented in Figure 4.37. In both cases, the dark current is greatly improved, whereas the current density measured at room light remains largely stable for 5 min. Taking both, dark and room light current density into account, a total current density of 0.5 and 1 mA/cm^2 can be provided by Cu-BDCNH$_2$/Cu$_2$O@Au and Cu-BDC(NHCOC$_7$F$_{15}$)/Cu$_2$O@Au after 5 min respectively. Since Cu$_2$O is only active under the light source, the additional current solely provided at room light indicates superior electrocatalytic properties for Cu-BDCNH$_2$.

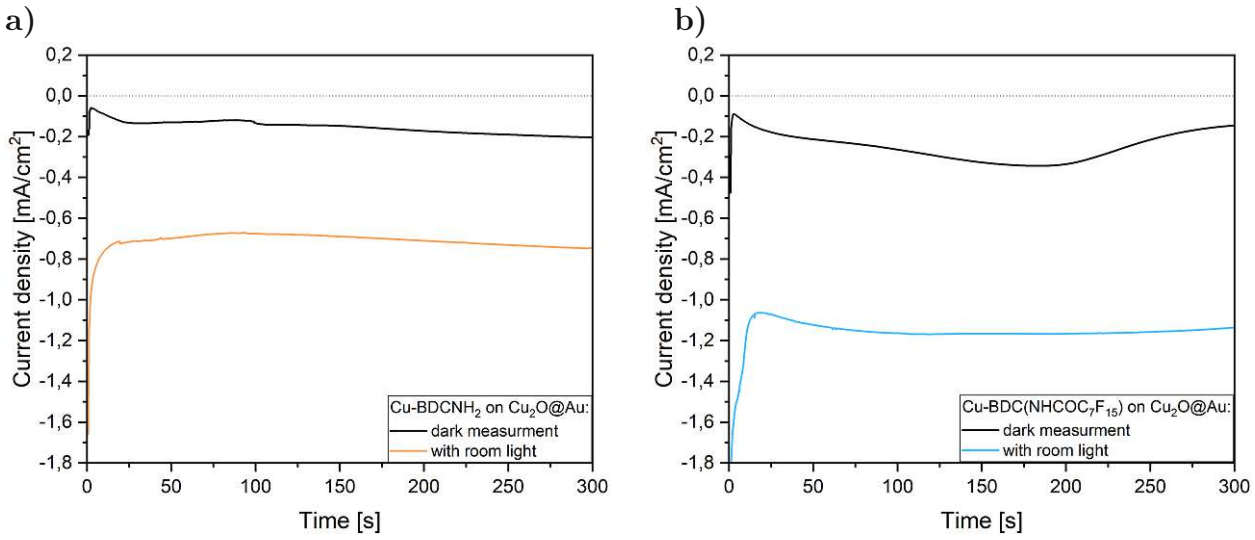

Figure 4.37: Evolution of the current density over 15 min: dark measurements were conducted by placing a box over the test set-up, whereas room light measurements were conducted by making only use of the laboratory room light without the usually applied light source.

Figure 4.38 provides a comparison of the stability performance of the different MOF-coatings compared to bare Cu$_2$O@Au. While the usual light source for Cu$_2$O was applied, only room light conditions were met for the MOF-coated samples. After 10 min, a slight decrease in the current density can be observed for Cu-BDC(NHCOC$_7$F$_{15}$)/Cu$_2$O@Au amounting to 1.1 mA/cm^2, whereas Cu-BDCNH$_2$/Cu$_2$O@Au records a current density of 0.8 mA/cm^2 at the

same time. In comparison, bare Cu_2O delivers a current density of 0.5 mA/cm^2 after 5 min. However, while the MOF-functionalization increases hydrophobicity greatly, it does not seem to show significant changes in performance.

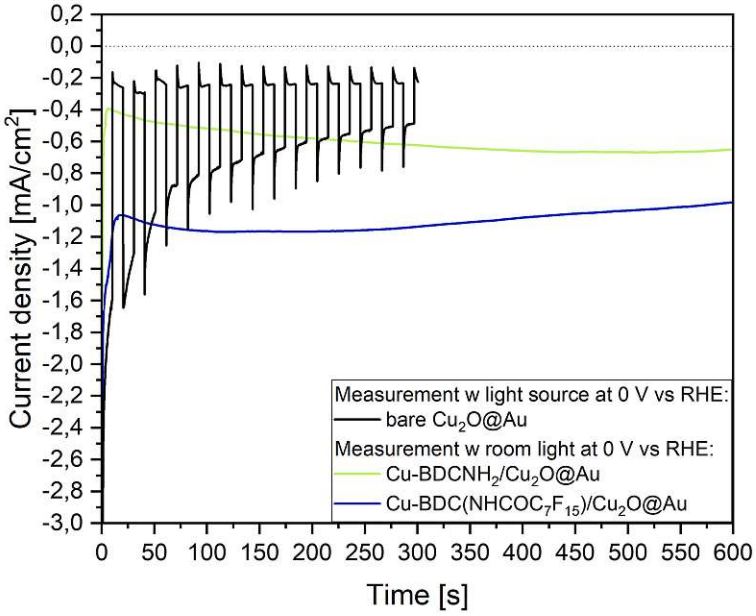

Figure 4.38: Stability test of different Cu_2O-based photo-cathodes under different conditions.

Examining the particularly the post-synthetic modified MOF surface under the SEM, a loss in the structural integrity of the MOF system can be revealed. Although the MOF layer is mostly intact, its damage can not be denied. Hence, it is most likely that the total current density obtained is a combination of HER as well as the destruction of the MOF.

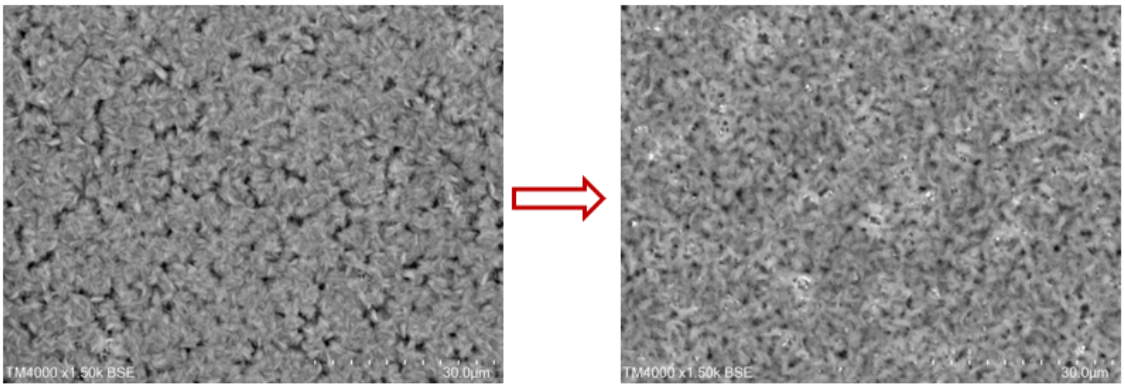

Figure 4.39: Structural evolution of the functionalized MOF layer after conducting a 10 min stability test under room light conditions.

Hydrophobic overlayers

The comparison of the different PDMS concentration layers is illustrated in Figure 4.40 for both Au and ITO. While no significant difference can be observed between the different wt% of PDMS at 0V vs RHE, 0.1 wt% PDMS still produces slightly higher current densities. Furthermore, 10 wt% PMDS shows the lowest dark current, particularly in combination with Cu_2O@ITO. Since PDMS does not increase the stability that much, there might be an issue with the PDMS films themselves, such as pin-holes or cracks, as discussed before.

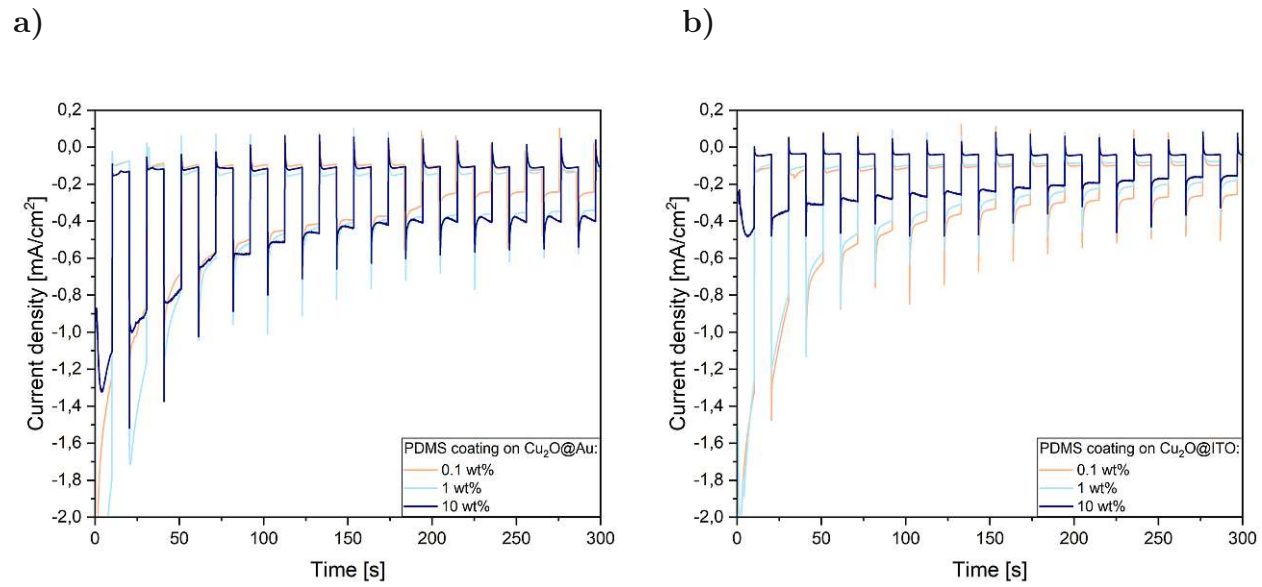

Figure 4.40: Evolution of the current density for a) 0.1 wt% PDMS b) 1 wt% PDMS over 5 min for a) Cu_2O@Au and b) Cu_2O@ITO.

The effects of multiple spin-coating with 0.1 wt% and 1 wt% PDMS on Cu_2O@Au are displayed in Figure 4.41. Although no significant difference can be observed between coating Cu_2O once or five times with 0.1 wt% PDMS, a slight improvement is noticeable for 1 wt% PDMS, which has been spin-coated five times.

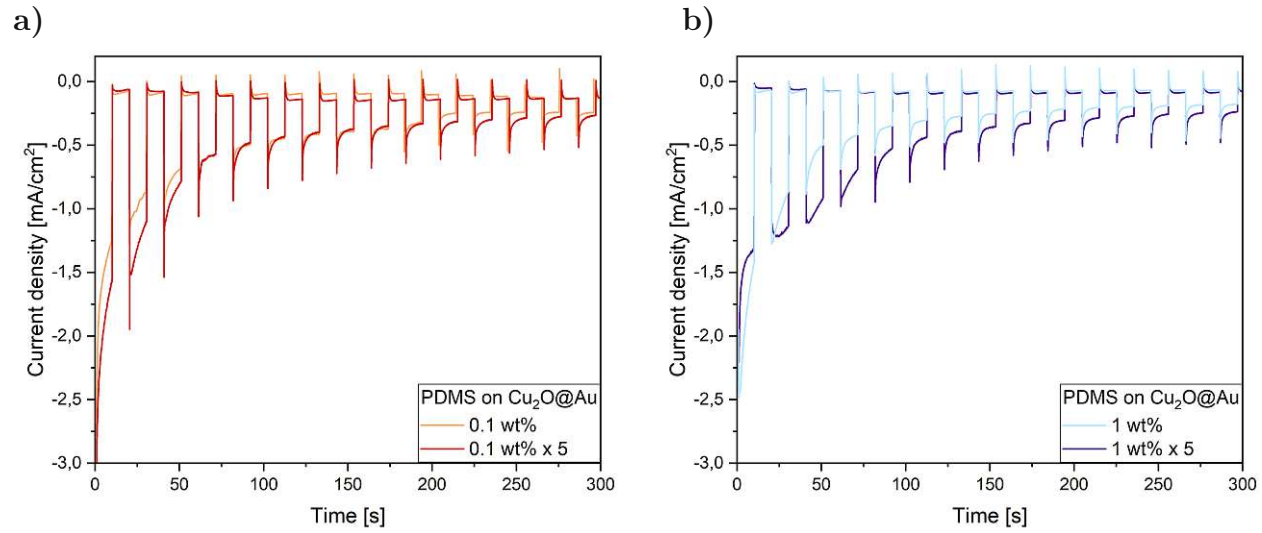

Figure 4.41: Evolution of the current density for a) 0.1 wt% PDMS b) 1 wt% PDMS, alongside a sample that has been coated five times with the respective PDMS concentration.

The peak in the anodic (positive) direction might be due to the accumulation of holes. On the other hand, when the light is switched on, a peak in the cathodic direction suggests an accumulation of electrons. This peak corresponds to "lost" current or dissipated charges and is usually a result of recombination events due to e.g., defects. In general, NTO/0.1wt% PDMS/Cu_2O@Au appears to be the best compromise between stability and current density, providing a stable current density of -0.5 mA/cm^2 for 5 min, performing better than the conventional oxide-based architecture cell (NTO/ZnO(S)/Cu_2O).

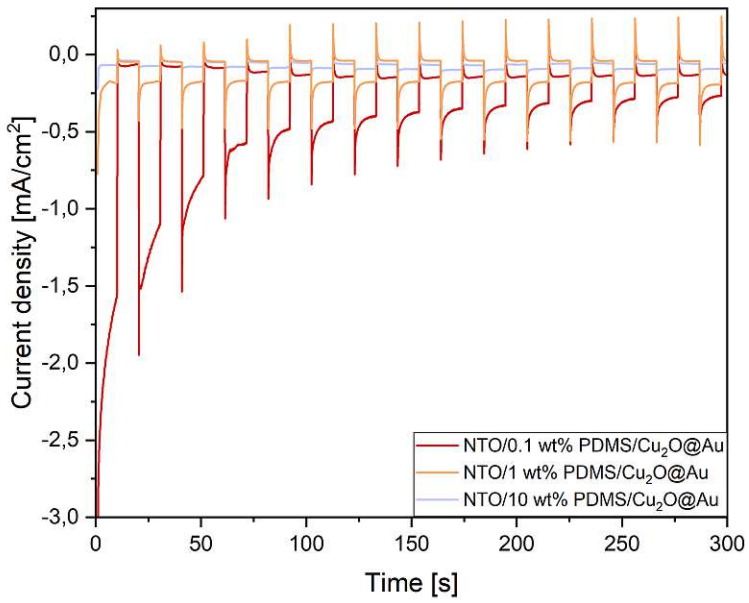

Figure 4.42: Evolution of the current density for NTO/PDMS-coated Cu_2O surfaces over 5 min.

Figure 4.43 provides a direct comparison of the stability performance for NTO and NTO/PDMS-protected Cu_2O surfaces. In both cases, the addition of NTO enhances stability in combination with PDMS. However, the current density for NTO/1 wt% PDMS/Cu_2O@Au is considerably lower compared to those samples that were coated with either one. NTO/0.1 wt% PDMS/Cu_2O@Au provides a current density of 0.5 mA/cm^2 after 300 s, alongside less pronounced anodic or cathodic peaks, indicating fewer recombination events and, thus, less "lost current".

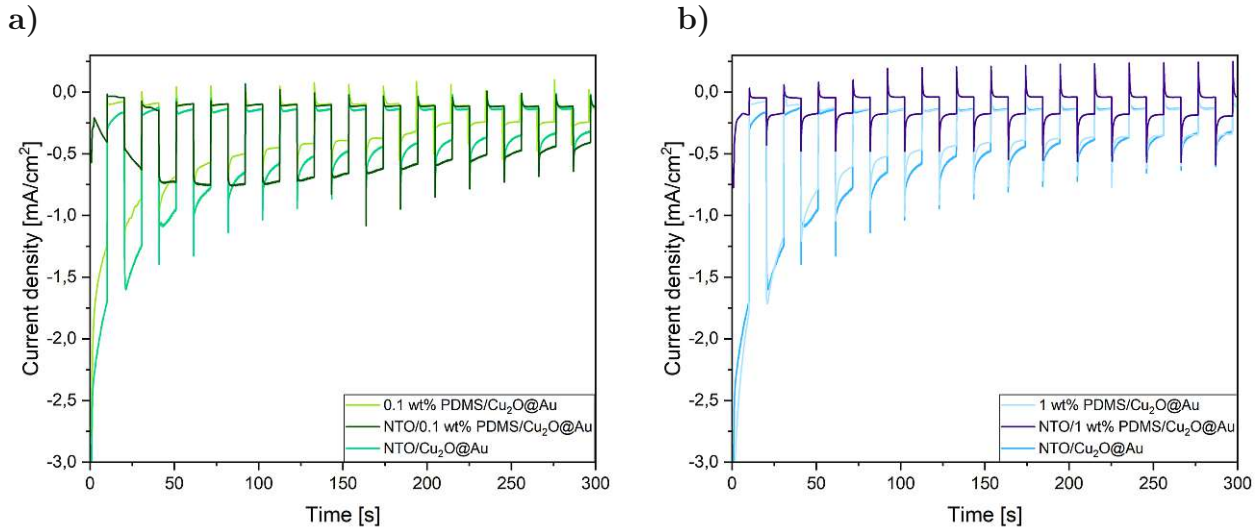

Figure 4.43: Comparison of evolution of the current density over 5 min involving a) 0.1 wt% PDMS-coated Cu_2O, and b) 1 wt% PDMS-coated Cu_2O surfaces. Additionally, NTO/Cu_2O and NTO/PDMS-coated Cu_2O samples are displayed.

5 | Conclusion and Outlook

Photo-electrochemical cells based on Cu_2O were successfully obtained via electrochemical bath deposition on Au/glass and ITO. While SEM images for Cu_2O on ITO showed the typical cubic-shaped crystals, SEM of Cu_2O on Au/glass reveals the growth of Cu_2O crystals in a more pyramidal-shaped manner. This is reflected in the X-ray diffractograms, where the preferred (111) peak showed higher intensity for Cu_2O on ITO, indicating a better quality of the Cu_2O film. By sputtering semiconductor-based oxide layers on the cuprous oxide films (NTO/ZnO(S), and NTO), a typical photo-cathode for PEC water-splitting was obtained. While NTO/Cu_2O@Au achieved a photo-current density of around 0.7 mA/cm^2, NTO/ZnO(S)/Cu_2O@Au provided a slightly higher photo-current density of around 0.8 mA/cm^2. Compared to this, bare Cu_2O@Au and Cu_2O@ITO achieved 2.0 mA/cm^2 and 1.6 mA/cm^2, respectively. The higher photo-current density for Cu_2O@Au might be due to overall less resistance in the system in addition to attachment problems of Cu_2O on ITO, thus, not all architectures were tested on ITO, but rather on Au.

Furthermore, metal-organic frameworks, namely Cu-BDCNH_2 MOFs, have been successfully synthesized on Cu_2O via solvothermal in-situ growth in an autoclave. This method allows the direct growth of MOFs on a substrate in an overall dense manner with good attachment. FTIR-ATR, alongside EDS measurements, confirmed the formation of Cu-BDCNH_2 on Cu_2O. Interestingly, as the in-situ growth requires the release of Cu^+ from the substrate, the XRD measurements reveal a sudden increase of the (111) peak for Cu_2O@Au compared to Cu_2O@ITO after the MOF synthesis, indicating that the less stable phases are used up first in the process. Moreover, via PSM of the amine group, it was possible to obtain a superhydrophobic surface, which was confirmed in a contact angle measurement with DI water as a probing liquid. Furthermore, while no distinct difference could be detected via XRD, the SEM demonstrated a surface of increased roughness after the PSM. The XPS analysis confirmed the successful functionalization with pentadecafluorooctanyol chloride was successful with the presence of the F1s at 686 eV. However, as the peak at 400 eV for N_{1s} is around half the intensity for the functionalized Cu-BDCNH_2 compared to the unfunctionalized sample, it is highly likely that the amine groups have not been completely fluorinated. The LSV measurements for Cu-BDCNH_2 and Cu-BDC($NHCOC_7F_{15}$) on Cu_2O showed a slight decrease in photo-current density for the functionalized sample, which might be explained by a slightly decreased light-absorbing ability or damaged MOF layer. Interestingly, an early on-set potential was observed for Cu-BDCNH_2 compared to common oxide overlayers. As for the stability measurements, no clear improvement was observed before and after the post-synthetic modification of Cu-BDCNH_2. However, conducting this measurement under different conditions (room light and darkness by covering the experimental set-up with a box) revealed an interesting behavior: Cu-BDCNH_2 displayed enhanced light-absorbing abilities generating around 0.8 mA/cm^2 for 5 min with only room light as a trigger, whereas Cu-BDC($NHCOC_7F_{15}$) provided 1.1 mA/cm^2 for 15 min.
In addition, polymer-based overlayers were implemented to enhance the stability of Cu_2O. Here, thin PDMS layers of different concentrations were spin-coated on Cu_2O and tested for

their potential photo-current density as well as stability. While 0.1 wt% provided a high photo-current density, it also displayed poor stability, which might be explained by attachment issues of PDMS on Cu_2O and/or pin-holes in the polymer film. Thus, multiple layers of PDMS were spin-coated on Cu_2O. While the photo-current density measured via LSV could be enhanced to 2.4 mA/cm^2, which is the highest obtained value, no distinct improvements regarding the stability were observed. The further addition of NTO layer to form a p-n junction between the two oxide layers (NTO/Cu_2O), also did not increase the stability dramatically.
All measured photo-current densities obtained via LSV are displayed in Table 5.1.

Table 5.1: Overview of photo-current densities for all investigated PEC architectures.

	Architecture	*current density [mA/cm^2]*
oxide-based	Cu_2O@Au	2.0
	Cu_2O@ITO	1.6
	NTO/Cu_2O@Au	0.7
	NTO/ZnO(S)/Cu_2O@Au	0.8
MOF-based	Cu-BDCNH_2/Cu_2O@Au	1.5
	Cu-BDCNH_2/Cu_2O@ITO	0.7
	Cu-BDC($NHCOC_7F_{15}$)/Cu_2O@Au	1.4
	Cu-BDC($NHCOC_7F_{15}$)/Cu_2O@ITO	1.3
polymer-based	0.1 wt% PDMS/Cu_2O@Au	2.1
	0.1 wt% PDMS/Cu_2O@ITO	1.5
	1 wt% PDMS/Cu_2O@Au	2.0
	1 wt% PDMS/Cu_2O@ITO	1.4
	10 wt% PDMS/Cu_2O@Au	0.9
	10 wt% PDMS/Cu_2O@ITO	0.5
	0.1 wt% PDMS x 5/Cu_2O@Au	2.4
	1 wt% PDMS x 5/Cu_2O@Au	1.9
	NTO/0.1 wt% PDMS/Cu_2O@Au	1.2
	NTO/1 wt% PDMS/Cu_2O@Au	0.2

In conclusion, Cu-BDCNH_2 showed promising behaviors such as an early on-set potential as well as enhanced light-absorbing abilities. While the method of in-situ growth provides MOF layers of good quality and attachment to the substrate, it also restricts the number of MOFs one can synthesize, as the underlying substrates provide the metal source for the MOF formation. However, by further adjusting the properties of the MOF through PSM, it is possible to address issues such as catalytic capabilities and stability, again accessing a wide range of different MOFs. Through PSM it was possible to obtain an overall photo-current density of 1.1 mA/cm^2 for 15 min without the aid of additional noble metal co-catalysts. Although the matter of stability will be the greatest concern for MOFs as well as Cu_2O, where the latter has been attempted to address with PDMS, the field of MOFs implemented in photo-cathodes for PEC water-splitting is still relatively unexplored.

Concerning the outlook of the implementation of MOFs in the field of PEC water-splitting, the PSM approach appears to be a promising route to further adjust the properties of the MOFs, which should be further explored - particularly towards enhanced hydrophobicity. Furthermore, additional techniques such as gas-chromatography should be applied to make a clear distinction between the current density generated via HER or side reactions, such as photo-corrosion, by quantifying the total amount of H_2 produced by the PEC cell. In addition,

as a wide range of MOFs exists, other structures should be investigated as they prove to be promising co-catalysts in the field of PEC water-splitting.

All in all, it is believed that the right combination of semiconducting material and MOF, as well as the adjustment of the latter by PSM, will play an interesting role in the pursuit of creating a low-cost and environmentally friendly photo-electrochemical cell for PEC water-splitting, which combines good stability and performance.

Bibliography

[1] Roozbeh Siavash Moakhar, Seyed Morteza Hosseini-Hosseinabad, Saeid Masudy-Panah, Ashkan Seza, Mahsa Jalali, Hesam Fallah-Arani, Fatemeh Dabir, Somayeh Gholipour, Yaser Abdi, Mohiedin Bagheri-Hariri, Nastaran Riahi-Noori, Yee-Fun Lim, Anders Hagfeldt, and Michael Saliba. Photoelectrochemical water-splitting using cuo-based electrodes for hydrogen production: A review. *Advanced Materials*, 33(33):2007285, 2021.

[2] Run Yu, Qianqiao Chen, Wenhua Li, Xinyuan Yu, and Qin Zhong. Decorating cu2o with ni-doped metal organic frameworks as efficient photocathodes for solar water splitting. *International Journal of Hydrogen Energy*, 2023.

[3] Jinyun Li, Wenwen Li, Guoxiong Deng, Ying Qin, Hongyan Wang, Yunjia Wang, and Song Xue. Polyimide stabilized cu2o photocathode for efficient pec water reduction. *Ionics*, 29:1–9, 11 2022.

[4] Sehar Tasleem, Muhammad Tahir, and Wesam Alsayeh Khalifa. Current trends in structural development and modification strategies for metal-organic frameworks (mofs) towards photocatalytic h2 production: A review. *International Journal of Hydrogen Energy*, 46(27):14148–14189, 2021.

[5] J. Curtin, C. McInerney, B. Ó Gallachóir, C. Hickey, P. Deane, and P. Deeney. Quantifying stranding risk for fossil fuel assets and implications for renewable energy investment: A review of the literature. *Renewable and Sustainable Energy Reviews*, 116:109402, 2019.

[6] Nick Watts, Markus Amann, Sonja Ayeb-Karlsson, Kristine Belesova, Timothy Bouley, Maxwell Boykoff, Peter Byass, Wenjia Cai, Diarmid Campbell-Lendrum, Jonathan Chambers, Peter M Cox, Meaghan Daly, Niheer Dasandi, Michael Davies, Michael Depledge, Anneliese Depoux, Paula Dominguez-Salas, Paul Drummond, Paul Ekins, Antoine Flahault, Howard Frumkin, Lucien Georgeson, Mostafa Ghanei, Delia Grace, Hilary Graham, Rébecca Grojsman, Andy Haines, Ian Hamilton, Stella Hartinger, Anne Johnson, Ilan Kelman, Gregor Kiesewetter, Dominic Kniveton, Lu Liang, Melissa Lott, Robert Lowe, Georgina Mace, Maquins Odhiambo Sewe, Mark Maslin, Slava Mikhaylov, James Milner, Ali Mohammad Latifi, Maziar Moradi-Lakeh, Karyn Morrissey, Kris Murray, Tara Neville, Maria Nilsson, Tadj Oreszczyn, Fereidoon Owfi, David Pencheon, Steve Pye, Mahnaz Rabbaniha, Elizabeth Robinson, Joacim Rocklöv, Stefanie Schütte, Joy Shumake-Guillemot, Rebecca Steinbach, Meisam Tabatabaei, Nicola Wheeler, Paul Wilkinson, Peng Gong, Hugh Montgomery, and Anthony Costello. The lancet countdown on health and climate change: from 25 years of inaction to a global transformation for public health. *The Lancet*, 391(10120):581–630, 2018.

[7] A.G. Olabi and Mohammad Ali Abdelkareem. Renewable energy and climate change. *Renewable and Sustainable Energy Reviews*, 158:112111, 2022.

[8] U.S Energy Information Administration. Monthly energy review march 2023. http:https://www.eia.gov/totalenergy/data/monthly/. Accessed: 2023-04-24.

[9] L. Gustavsson, T. Nguyen, R. Sathre, and U.Y.A. Tettey. Climate effects of forestry and substitution of concrete buildings and fossil energy. *Renewable and Sustainable Energy Reviews*, 136:110435, 2021.

[10] Global Change Data Lab. Global direct primary energy consumption. https://ourworldindata.org/grapher/sub-energy-fossil-renewables-nuclear. Accessed: 2023-04-24.

[11] Global Change Data Lab. Global direct primary energy consumption. https://ourworldindata.org/grapher/global-primary-energy. Accessed: 2023-04-24.

[12] Mikael Höök and Xu Tang. Depletion of fossil fuels and anthropogenic climate change - a review. *Energy Policy*, 53:797–809, 01 2013.

[13] T Bak, J Nowotny, M Rekas, and C.C Sorrell. Photo-electrochemical hydrogen generation from water using solar energy. materials-related aspects. *International Journal of Hydrogen Energy*, 27(10):991–1022, 2002.

[14] Bastian Mei, Kai Han, and Guido Mul. Driving surface redox reactions in heterogeneous photocatalysis: The active state of illuminated semiconductor-supported nanoparticles during overall water-splitting. *ACS Catalysis*, 8(10):9154–9164, 2018. PMID: 30319883.

[15] Alexandra M Oliveira, Rebecca R Beswick, and Yushan Yan. A green hydrogen economy for a renewable energy society. *Current Opinion in Chemical Engineering*, 33:100701, 2021.

[16] Mohammed Al-Breiki and Yusuf Bicer. Investigating the technical feasibility of various energy carriers for alternative and sustainable overseas energy transport scenarios. *Energy Conversion and Management*, 209:112652, 2020.

[17] Lorna Jeffery Minggu, Wan Ramli Wan Daud, and Mohammad B. Kassim. An overview of photocells and photoreactors for photoelectrochemical water splitting. *International Journal of Hydrogen Energy*, 35(11):5233–5244, 2010.

[18] AKIRA FUJISHIMA and KENICHI HONDA. Electrochemical photolysis of water at a semiconductor electrode. *Nature*, 238(5358):37–38, jul 1972.

[19] Linfeng Pan, Seunghyeon Kim, Matthew Mayer, Min-Kyu Son, Amita Ummadisingu, Jae Sung Lee, Anders Hagfeldt, Jingshan Luo, and Michael Grätzel. Boosting the performance of cu2o photocathodes for unassisted solar water splitting devices. *Nature Catalysis*, 1, 06 2018.

[20] Chong-Chen Wang, Xiao-Hong Yi, and Peng Wang. Powerful combination of mofs and c3n4 for enhanced photocatalytic performance. *Applied Catalysis B: Environmental*, 247:24–48, 2019.

[21] Sisi Chen, Runmin Huang, Jiao Zou, Dan Liao, Jingang Yu, and Xinyu Jiang. A sensitive sensor based on mofs derived nanoporous carbons for electrochemical detection of 4-aminophenol. *Ecotoxicology and Environmental Safety*, 191:110194, 2020.

[22] Xi Deng, Rui Li, Sikai Wu, Li Wang, Jiahua Hu, Jun Ma, Wenbin Jiang, Ning Zhang, Xusheng Zheng, Chao Gao, Linjun Wang, Qun Zhang, Junfa Zhu, and Yujie Xiong. Metal–organic framework coating enhances the performance of cu2o in photoelectrochemical co2 reduction. *Journal of the American Chemical Society*, 141(27):10924–10929, 2019.

[23] Huanhao Chen, Yibing Mu, Yan Shao, Sarayute Chansai, Huan Xiang, Yilai Jiao, Christopher Hardacre, and Xiaolei Fan. Nonthermal plasma (ntp) activated metal–organic frame-

works (mofs) catalyst for catalytic co2 hydrogenation. *AIChE Journal*, 66(4):e16853, 2020.

[24] Shuliang Yang, Li Peng, Safak Bulut, and Wendy L. Queen. Recent advances of mofs and mof-derived materials in thermally driven organic transformations. *Chemistry – A European Journal*, 25(9):2161–2178, 2019.

[25] Xianlong Li, Zhiliang Wang, and Lianzhou Wang. Metal–organic framework-based materials for solar water splitting. *Small Science*, 1(5):2000074, 2021.

[26] Mohit Kumar, Bhagatram Meena, Palyam Subramanyam, Duvvuri Suryakala, and Challapalli Subrahmanyam. Recent trends in photoelectrochemical water splitting: the role of cocatalysts. *NPG Asia Materials*, 14(1):88, 2022.

[27] Xin Li, Jiaguo Yu, Jingxiang Low, Yueping Fang, Jing Xiao, and Xiaobo Chen. Engineering heterogeneous semiconductors for solar water splitting. *J. Mater. Chem. A*, 3:2485–2534, 2015.

[28] Michael G. Walter, Emily L. Warren, James R. McKone, Shannon W. Boettcher, Qixi Mi, Elizabeth A. Santori, and Nathan S. Lewis. Solar water splitting cells. *Chemical Reviews*, 110(11):6446–6473, 2010.

[29] Qiurong Shi, Chengzhou Zhu, Dan Du, and Yuehe Lin. Robust noble metal-based electrocatalysts for oxygen evolution reaction. *Chem. Soc. Rev.*, 48:3181–3192, 2019.

[30] Chaoran Jiang, Savio J. A. Moniz, Aiqin Wang, Tao Zhang, and Junwang Tang. Photoelectrochemical devices for solar water splitting – materials and challenges. *Chem. Soc. Rev.*, 46:4645–4660, 2017.

[31] Adriana Paracchino, Vincent Laporte, Kevin Sivula, Michael Grätzel, and Elijah Thimsen. Highly active oxide photocathode for photoelectrochemical water reduction. *Nature materials*, 10:456–61, 06 2011.

[32] Walter H. Brattain. The copper oxide rectifier. *Rev. Mod. Phys.*, 23:203–212, Jul 1951.

[33] AF Wright and JS Nelson. Theory of the copper vacancy in cuprous oxide. *Journal of Applied Physics*, 92(10):5849–5851, 2002.

[34] David O Scanlon, Benjamin J Morgan, Graeme W Watson, and Aron Walsh. Acceptor levels in p-type cu 2 o: rationalizing theory and experiment. *Physical review letters*, 103(9):096405, 2009.

[35] O. Porat and Ilan Riess. Defect chemistry of cu2yo at elevated temperatures. part i: Non-stoichiometry, phase width and dominant point defects. *Solid State Ionics*, 74:229–238, 1994.

[36] Norman Lee Peterson and CL Wiley. Diffusion and point defects in cu2o. *Journal of Physics and Chemistry of Solids*, 45(3):281–294, 1984.

[37] René Wick and S. David Tilley. Photovoltaic and photoelectrochemical solar energy conversion with cu2o. *The Journal of Physical Chemistry C*, 119(47):26243–26257, 2015.

[38] Indrajit V. Bagal, Nilesh R. Chodankar, Mostafa Afifi Hassan, Aadil Waseem, Muhammad Ali Johar, Do-Heyoung Kim, and Sang-Wan Ryu. Cu2o as an emerging photocathode for solar water splitting - a status review. *International Journal of Hydrogen Energy*, 44(39):21351–21378, 2019.

[39] Kailai Zhang, Haijun Hu, Litong Shi, Baohua Jia, Hongwei Huang, Xiaopeng Han, Xiaodong Sun, and Tianyi Ma. Strategies for optimizing the photocatalytic water-splitting performance of metal–organic framework-based materials. *Small Science*, 1(12):2100060, 2021.

[40] Yun-Nan Gong, Jin-Wang Liu, Bi-Zhu Shao, Di-Chang Zhong, and Tong-Bu Lu. Stable metal–organic frameworks for pec water splitting. *FlatChem*, 27:100240, 2021.

[41] Hiroyasu Furukawa, Kyle E. Cordova, Michael O'Keeffe, and Omar M. Yaghi. The chemistry and applications of metal-organic frameworks. *Science*, 341(6149):1230444, 2013.

[42] Ying Liu, Jianmin Lu, Qianxiao Zhang, Yajie Bai, Xuliang Pang, Song Wang, Hongye Bai, and Weiqiang Fan. Charge-transfer dynamics at a ag/ni-mof/cu2o heterostructure in photoelectrochemical nh3 production. *Chem. Commun.*, 57:8031–8034, 2021.

[43] Mercedes Alvaro, Esther Carbonell, Belén Ferrer, FrancescX. LlabrésiXamena, and Hermenegildo Garcia. Semiconductor behavior of a metal-organic framework (mof). *Chemistry – A European Journal*, 13(18):5106–5112.

[44] K. Meyer, M. Ranocchiari, and J. A. van Bokhoven. Metal organic frameworks for photocatalytic water splitting. *Energy Environ. Sci.*, 8:1923–1937, 2015.

[45] Meicheng Wen, Kohsuke Mori, Takashi Kamegawa, and Hiromi Yamashita. Amine-functionalized mil-101(cr) with imbedded platinum nanoparticles as a durable photocatalyst for hydrogen production from water. *Chem. Commun.*, 50:11645–11648, 2014.

[46] Cláudia GomesSilva, Ignacio Luz, Francesc X. LlabrésiXamena, Avelino Corma, and Hermenegildo García. Water stable zr–benzenedicarboxylate metal–organic frameworks as photocatalysts for hydrogen generation. *Chemistry – A European Journal*, 16(36):11133–11138, 2010.

[47] Chuantao Hou, Qin Xu, Yanjuan Wang, and Xiaoya Hu. Synthesis of pt@nh2-mil-125(ti) as a photocathode material for photoelectrochemical hydrogen production. *RSC Adv.*, 3:19820–19823, 2013.

[48] Jingshu Zhao, Yin Wang, Junwen Zhou, Pengfei Qi, Siwu Li, Kexin Zhang, Xiao Feng, Bo Wang, and Changwen Hu. A copper(ii)-based mof film for highly efficient visible-light-driven hydrogen production. *J. Mater. Chem. A*, 4:7174–7177, 2016.

[49] Xi-Yan Dong, Mei Zhang, Ru-Bo Pei, Qian Wang, Dong-Hui Wei, Shuang-Quan Zang, Yao-Ting Fan, and Thomas CW Mak. A crystalline copper (ii) coordination polymer for the efficient visible-light-driven generation of hydrogen. *Angewandte Chemie International Edition*, 55(6):2073–2077, 2016.

[50] Zhi-Lei Wu, Chang-Hong Wang, Bin Zhao, Jie Dong, Feng Lu, Wei-Hua Wang, Wei-Chao Wang, Guang-Jun Wu, Jian-Zhong Cui, and Peng Cheng. A semi-conductive copper–organic framework with two types of photocatalytic activity. *Angewandte Chemie International Edition*, 55(16):4938–4942, 2016.

[51] Man Luo, Huimin Li, Zhifei Wang, Qianqian Shen, Jinbo Xue, Xuguang Liu, and Husheng Jia. In-situ growth of mof nanosheets with controllable thickness on copper foam for photoelectrocatalytic co2 reduction. *Journal of Materials Science: Materials in Electronics*, 33:1–13, 06 2022.

[52] Beatriz Costa e Silva, Kallyni Irikura, Regina Célia Galvão Frem, and Maria Valnice Boldrin Zanoni. Effect of cu(bdc-nh2) mof deposited on cu/cu2o electrode and its

better performance in photoelectrocatalytic reduction of co2. *Journal of Electroanalytical Chemistry*, 880:114856, 2021.

[53] Pramod Patil Kunturu and Jurriaan Huskens. Efficient solar water splitting photocathodes comprising a copper oxide heterostructure protected by a thin carbon layer. *ACS Applied Energy Materials*, 2(11):7850–7860, 2019.

[54] Yang Li, Xiaolan Zhong, Kai Luo, and Zongping Shao. A hydrophobic polymer stabilized p-cu2o nanocrystal photocathode for highly efficient solar water splitting. *J. Mater. Chem. A*, 7:15593–15598, 2019.

[55] Amare Aregahegn Dubale, Wei-Nien Su, Andebet Gedamu Tamirat, Chun-Jern Pan, Belete Asefa Aragaw, Hong-Ming Chen, Ching-Hsiang Chen, and Bing-Joe Hwang. The synergetic effect of graphene on cu2o nanowire arrays as a highly efficient hydrogen evolution photocathode in water splitting. *J. Mater. Chem. A*, 2:18383–18397, 2014.

[56] Huan Qi, Jonathan Wolfe, Denis Fichou, and Zhong Chen. Cu2o photocathode for low bias photoelectrochemical water splitting enabled by nife-layered double hydroxide cocatalyst. *Scientific Reports*, 6:30882, 08 2016.

[57] Shengsen Zhang, Jie Yan, Siyuan Yang, Yuehua Xu, Xin Cai, Xin Li, Xiangchao Zhang, Feng Peng, and Yueping Fang. Electrodeposition of cu2o/g-c3n4 heterojunction film on an fto substrate for enhancing visible light photoelectrochemical water splitting. *Chinese Journal of Catalysis*, 38(2):365–371, 2017.

[58] Manjeet Chhetri and C. N. R. Rao. Photoelectrochemical hydrogen generation employing a cu2o-based photocathode with improved stability and activity by using nixpy as the cocatalyst. *Phys. Chem. Chem. Phys.*, 20:15300–15306, 2018.

[59] Jatinder Kaur, Ole Bethge, Rachmat Wibowo, Neha Bansal, Martin Bauch, R. Hamid, Emmerich Bertagnolli, and Theodoros Dimopoulos. All-oxide solar cells based on electrodeposited cu2o absorber and atomic layer deposited znmgo on precious-metal-free electrode. *Solar Energy Materials and Solar Cells*, 161:449–459, 03 2017.

[60] Rolando Guidelli, Richard Compton, J.M. Feliu, Eliezer Gileadi, Jacek Lipkowski, Wolfgang Schmickler, and Sergio Trasatti. Defining the transfer coefficient in electrochemistry: An assessment (iupac technical report). *Pure and Applied Chemistry*, 86:245–258, 02 2014.

[61] Lian Guo, Gerko Oskam, Aleksandar Radisic, Peter Hoffmann, and Peter Searson. Island growth in electrodeposition. *Journal of Physics D: Applied Physics*, 44:443001, 10 2011.

[62] Sanjib Shyamal, Arjun Maity, Ashis Kumar Satpati, and Chinmoy Bhattacharya. Development of cu2o thin films under the influence of electrochemical impedance: Applications in improved photoelectrochemical water reduction. *Electrochimica Acta*, 308:384–391, 2019.

[63] D. Mohra, M. Benhaliliba, M. Serin, M. R. Khelladi, H. Lahmar, and A. Azizi. The investigation of electrodeposited cu2o/ito layers by chronocoulometry process: effect of electrical potential*. *Journal of Semiconductors*, 37(10):103001, oct 2016.

[64] Angstrom Engineering. Magnetron sputtering overview. https://angstromengineering.com/tech/magnetron-sputtering/. Accessed: 2023-05-12.

[65] Muralidhar Singh M, Vijaya G, Krupashankara MS, B K Sridhara, and T N Shridhar. Studies on nanostructure aluminium thin film coatings deposited using dc mag-

netron sputtering process. *IOP Conference Series: Materials Science and Engineering*, 149(1):012071, sep 2016.

[66] Semicore Equipment, Inc. What is rf sputtering? https://https://www.semicore.com/news/92-what-is-rf-sputtering. Accessed: 2023-05-12.

[67] Nishesh Kumar Gupta, Suho Kim, Jiyeol Bae, and Kwang Soo Kim. Chemisorption of hydrogen sulfide over copper-based metal–organic frameworks: methanol and uv-assisted regeneration. *RSC Adv.*, 11:4890–4900, 2021.

[68] Muhammad Fiaz and Muhammad Athar. Enhancing the hydrogen and oxygen evolution reaction efficiency of amine functionalized mof nh2-uio-66 via incorporation of cuo nanoparticles. *Catalysis Letters*, 150, 04 2020.

[69] Joseph G. Nguyen and Seth M. Cohen. Moisture-resistant and superhydrophobic metalorganic frameworks obtained via postsynthetic modification. *Journal of the American Chemical Society*, 132(13):4560–4561, 2010.

[70] Tristan T. Y. Tan, Michael R. Reithofer, Eric Y. Chen, Ajay G. Menon, T. S. Andy Hor, Jianwei Xu, and Jia Min Chin. Tuning omniphobicity via morphological control of metal–organic framework functionalized surfaces. *Journal of the American Chemical Society*, 135(44):16272–16275, 2013.

[71] Lu Ye, Yan Gao, Shuyan Cao, Hu Chen, Yanan Yao, Jungang Hou, and Licheng Sun. Assembly of highly efficient photocatalytic co2 conversion systems with ultrathin two-dimensional metal–organic framework nanosheets. *Applied Catalysis B: Environmental*, 227:54–60, 2018.

[72] Bingqing Wang, Jing Jin, Bin Ding, Xu Han, Aijuan Han, and Junfeng Liu. General approach to metal-organic framework nanosheets with controllable thickness by using metal hydroxides as precursors. *Frontiers in Materials*, 7, 2020.

[73] Template-directed growth of well-aligned mof arrays and derived self-supporting electrodes for water splitting. *Chem*, 2(6):791–802, 2017.

[74] Guowu Zhan, Longlong Fan, Feigang Zhao, Zhongliang Huang, Bin Chen, Xin Yang, and Shu-feng Zhou. Fabrication of ultrathin 2d cu-bdc nanosheets and the derived integrated mof nanocomposites. *Advanced Functional Materials*, 29(9):1806720, 2019.

[75] Hoon Ji, Sunhyun Hwang, Keonmok Kim, CheolGi Kim, and Nak Cheon Jeong. Direct in situ conversion of metals into metal–organic frameworks: A strategy for the rapid growth of mof films on metal substrates. *ACS Applied Materials & Interfaces*, 8(47):32414–32420, 2016.

[76] Xiaojiao Yu, Xiyan Tang, Ju Li, Jie Zhang, Song Kou, Jie Zhao, and Binghua Yao. Nucleation mechanism and optoelectronic properties of cu2o onto ito electrode in the electrochemical deposition process. *Journal of The Electrochemical Society*, 164(14):D999, dec 2017.

[77] Dhritiman Gupta, S.R. Meher, Navas Illyaskutty, and Zachariah C. Alex. Facile synthesis of cu2o and cuo nanoparticles and study of their structural, optical and electronic properties. *Journal of Alloys and Compounds*, 743:737–745, 2018.

Nomenclature

Abbreviations

ALD Àtomic layer deposition
AM Air mass
ATR-FTIR Attenuated reflection Fourier-transformed infrared spectroscopy
AZO Aluminium-doped zinc oxide
BG Band gap
CA Contact angle
CB Conduction band
CE Counter electrode
DC Direct current
ECD Electrochemical bath deposition
EDS Energy dispersive X-ray spectroscopy
GHG Greenhouse gases
HER Hydrogen evolution reaction
HOMO Highest occupied molecular orbital
LMTC Ligand to metal charge transfer
LUMO Lowest occupied molecular orbital
MOF Metal-organic framework
NHE Normal hydrogen evolution
NTO Niobium doped Titanium oxide
OER Oxygen evolution reaction
PEC Photo-electrochemical
RE Reference electrode
RF Radio frequency
RHE Reversible hydrogen evolution
SEM Scanning electron microscopy
STH Solar-to-hydrogen
TWh Terawatt-hour
VB Valance band
WE Working electrode
XPS X-ray photo-electron spectroscopy

XRD X-ray diffractogram

Subscripts

α Cathodic charge transfer coefficient

ΔG Gibbs free energy

η Overpotential

E^0_{ox} Water oxidation potential

E^0_{red} Proton reduction potential

E_{CB} Energy band position conduction band

E_{eq} Equilibrium potential

E_{VB} Energy band position valance band

F Faraday constant

j_0 Exhange current density

R Ideal gas constant

Units

$°C$ Celsius

$°$ Degree

$a.u$ Arbitrary unit

A Ampere

Cb Coulomb

eV Electron volt

g Gram

M Molarity

min Minutes

rpm Rotation per minute

s Seconds

V Voltage

$wt\%$ Weight percent